Master's Thesis

No. 716

Concept Evaluation and Modeling of a Magnetic Out of Axis Angle Measurement System

presented by

Gernot Binder

at the

Institute for Electronics

Graz University of Technology

Head: Univ.-Prof. DI Dr. techn. Wolfgang Bösch

in Cooperation with

Infineon Technologies Austria AG

Advisor TU Graz: DI Dr. techn. Mario Auer

Advisor Infineon: DI(FH) Wolfgang Granig

Acknowledgement

This thesis was written in cooperation with Infineon Technologies Austria AG and Graz University of Technology. I would like to thank my supervisor DI(FH) Wolfgang Granig for sharing his expertise and his valuable suggestions while writing this thesis. I also like to thank Dr. Armin Satz and DI Markus Weinberger for their help during the daily work. Furthermore I thank my supervisor Dr. Mario Auer from the Institute for Electronics for the uncomplicated organization and his helpful advices.

Finally I would like to thank my girlfriend Nina for her lovely support and for always motivating me. I dedicate this work to my parents for their permanent support during my studies.

Statutory Declaration

I declare that I have authored this thesis independently, that I have not used other than the declared sources / resources, and that I have explicitly marked all material which has been quoted either literally or by content from the used sources.

…… ……..

date (signature)

Abstract

Brushless direct current electrical commutated motors are getting more and more popular in the automotive environment. Due to the missing mechanical commutation some rotor position feedback for motor control has to be provided. Typically this is done using angle sensors. In automotive applications magnetic sensing principles are used because of their robustness. A high precision feedback system can be realized with a diametrically magnetized permanent magnet mounted to the end of the motor shaft and a GMR-based angle sensor placed in front of it, which is the current state of the art. In this work a new out of axis angle measurement system is presented, in which the sensor is placed alongside the shaft. A new algorithm relying on an existing measurement principle delivers improved accuracy compared to the standard approach. Optionally this algorithm can be combined with a new hardware measurement setup leading to a highly accurate overall angle measurement system. The angle error of this setup is about +0.06° / -0.07°, which is considerable lower compared to the standard approach having an error of +4.23° / -3.50°. Furthermore a MATLAB Simulink model of the new angle measurement system was developed, where also the influences of sensor electronics and signal processing are taken into account.

Kurzfassung

Die Verwendung von BLDC Motoren (bürstenlose elektrisch kommutierte Gleichstrommotoren) wird im Automobilbereich immer populärer. Aufgrund des fehlenden mechanischen Kommutators muss ein Rotorpositions-Feedbacksystem für die Motorsteuerung bereitgestellt werden. Dies kann beispielsweise mit Winkelsensoren erfolgen. Für Anwendungen in der Automobilindustrie werden aufgrund ihrer Robustheit magnetische Sensorprinzipien bevorzugt. Durch einen diametral magnetisierten Permanentmagneten, der am Ende der Motorwelle befestigt wird und einen gegenüber dem Wellenende platzierten GMR basierten Winkelsensor kann ein hochgenaues Feedbacksystem realisiert werden. Diese Anordnung stellt den aktuellen Stand der Technik dar. In dieser Arbeit wird ein neues Winkelmesssystem präsentiert, bei dem der Sensor nicht am Wellenende sondern seitlich neben der Welle am Wellenumfang sitzt. Ein neuer Algorithmus ermöglicht basierend auf einem bereits existierenden Messverfahren erhöhte Genauigkeit im Vergleich zum Standardverfahren. Optional kann dieser Algorithmus mit einem neuen Hardwaresetup zur Winkelmessung kombiniert werden, was zu einem hochgenauen Winkelmesssystem führt. Der Winkelfehler dieses Systems liegt bei ungefähr 0.06° / -0.07°. Der Fehler ist damit wesentlich kleiner im Vergleich zum Standardansatz mit einem Fehler von +4.23° / -3.50°. Weiters wurde ein MATLAB Simulink Modell des neuen Winkelmesssystems entwickelt, in dem auch der Einfluss der elektronischen Komponenten sowie der Signalverarbeitung betrachtet wird.

Table Of Contents

Acronyms And Abbreviations

ADC:	Analog-to-Digital Converter
AMR:	Anisotropic Magneto Resistance
ASIC:	Application Specific Integrated Circuit
BLDC:	Brushless Direct Current
DAC:	Digital-to-Analog Converter
DC:	Direct Current
DFT:	Discrete Fourier Transform
DR:	Dynamic Range
ENOB:	Effective Number Of Bits
EPS:	Electrical Power Steering
FEM:	Finite Element Method
FFT:	Fast Fourier Transform
GMR:	Giant Magneto Resistance
HVAC:	Heating Ventilating and Air Conditioning
LSB:	Least Significant Bit
MSB:	Most Significant Bit
OSR:	Oversampling Ratio
OL:	Overload Level
PWM:	Pulse Width Modulation
RMS:	Root Mean Square
SAR:	Successive Approximation Register
SINAD:	Signal-to-Noise And Distortion ratio
SNR:	Signal-to-Noise Ratio

List Of Tables

List Of Figures

1 Introduction

1.1 Problem Description and Outline

In recent history the usage of brushless DC electrical commutated motors experienced increasing interest in the automotive environment. The motor serves as actuator in various automotive systems. Steering angles, windshield wipers or throttle valve controls are just a few demonstrative applications. The absence of the mechanical commutator results in the need for accurate shaft angle measurement in order to determine the rotor’s position. The more accurate the shaft angle is measured, the better the current commutation can be timed. This increases the motor's efficiency.

There exist different sensing principles to measure the shaft position. In the automotive environment magnetic principles clearly outperform other systems due to the following reasons. Magnetic sensors work contactless, thus there is no mechanical wear. They are insensitive to dirt, which is the main advantage compared to optical systems. Moreover they are robust against vibrations and operate properly over a wide temperature range. Thus they are suitable for rough environmental conditions as prevalent for instance in the engine compartment. Finally they are durable and highly cost-effective as they can be integrated using standard silicon processing techniques.

Figure 1 - 1 illustrates the state of the art setup for shaft angle measurement using a magnetic sensing system. There is a diametrically magnetized permanent magnet mounted at the end of a rotating shaft. The sensor, including an ASIC, is placed in front of the shaft.

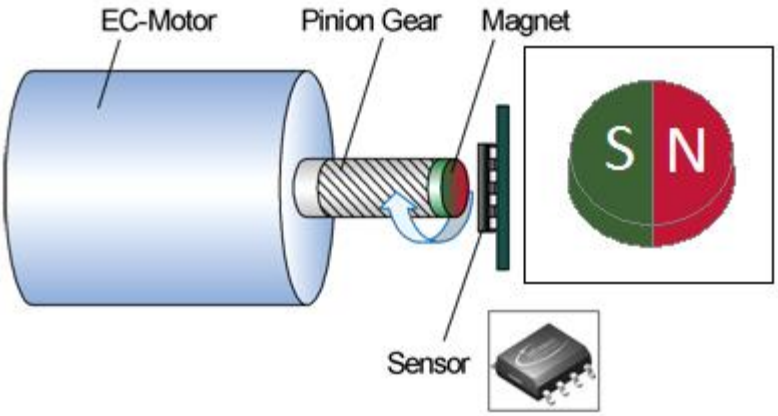

Figure 1 - 1: State of the art angle measurement setup.
There is a diametrically magnetized permanent magnet mounted to the end of the rotating shaft. A sensor is placed in front of the shaft. Image based on [1], p. 281

In some cases, for instance due to limited space, it is not possible to measure the angle at the end of the motor shaft. For this purpose the so called out of axis angle measurement is a possible alternative, in which the sensor is not located at the end but alongside the shaft. Figure 1 - 2 illustrates this setup.

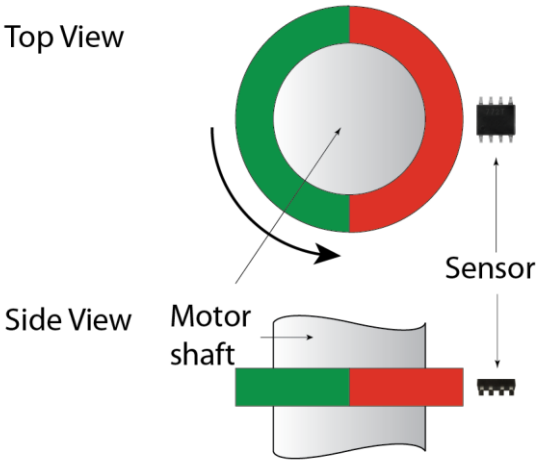

Figure 1 - 2: Example of an out of axis angle measurement setup
The sensor is located alongside the shaft

Moving the sensor from the axis' center however results in increasing angle errors. First MATLAB simulations have shown that increasing the number of pole pairs on the magnet (pole wheel) mitigates this problem [2]. Using more than one pole pair however leads to the loss of unambiguity in angle detection over 360°, as each pole pair excites a

full stroke. For instance a pole wheel with 2 pole pairs delivers two electrical signal periods from 0 to 360° over one mechanical 360° rotation.

The aim of this work is to propose an out of axis angle measurement system based on magnetic sensor principles for rotating shaft applications. Thereby the system has to be capable of measuring the absolute shaft angle with very high accuracy. The sensor system of interest consists of the following main parts:

- Magnet
- Sensor
- Signal conditioning (ASIC)

The angle error at the output of the sensor system will be analyzed as a function of different parameters, given by the major building blocks depicted in Figure 1 - 3.

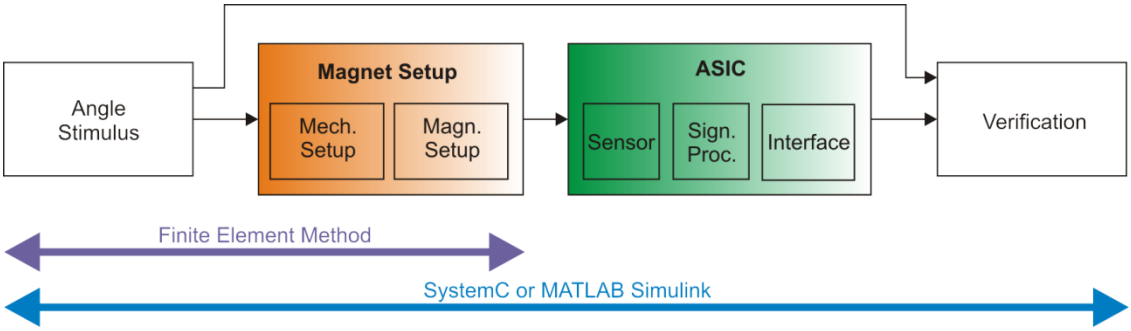

Figure 1 - 3: Overview of the angle measurement system.
FEM software (ANSYS) is used to develop a well suited magnetic circuit design for the out of axis angle measurement application. The influence of signal processing and sensor electronics is modeled using MATLAB Simulink.

In this work the major system parameters influencing the angle error will be identified and different system proposals covering different complexity classes of the sensor system with different reachable angle accuracies will be shown.

After identifying the most suitable magnetic sensing principle, different analog-to-digital converter concepts will be discussed, which are necessary to transform the sensor signals into the digital domain for further signal processing.

Chapter 1 introduces the standard brushless direct current (BLDC) motor working principle and its motor control as a typical application demanding for out of axis angle measurement. Thereafter different magnetic effects suitable for magnetic angle sensors are introduced. This work concentrates on the Hall, AMR and GMR effect. Followed by a short introduction to these effects, a comparison between Hall and xMR is shown.

Chapter 2 is about the magnetic concept evaluations. Different out of axis angle measurement systems relying on magnetic sensing principles are discussed. The so called Vernier principle turns out to be a sophisticated method for absolute angle measurement. Based on the standard Vernier principle a new algorithm leading to much higher accuracy is proposed. Additionally this algorithm can be combined with a new two-probe principle leading to even higher accuracies. The new measurement system is investigated in detail.

Chapter 3 is concerned with the modeling of the sensor electronics and the electrical signal processing. The focus in this chapter is on the analog-to-digital conversion (ADC) which is necessary to transfer the analog sensor signals into the digital domain. Finally a MATLAB Simulink model of the angle measurement system is presented.

In chapter 4 the results of simulation and insights of this master thesis are summarized.

1.2 Brushless DC Motor Working Principle

This chapter gives an introduction to the working principle and the advantages and disadvantages of brushless direct current (BLDC) motors. The information was taken from [3].

Figure 1 - 4 shows the simplest form of a BLDC motor, where three excitation coils are mounted at the stator and a permanent magnet with one pole pair is attached to the rotor. While brushed motors use a mechanical contact in order to commutate the current flowing through the excitation coils at defined rotor positions, there is no such contact in case of the BLDC motor. In contrast to a standard motor, where the coils are mounted

on the rotor and the permanent magnet on the stator, this is inverted for the brushless DC motor.

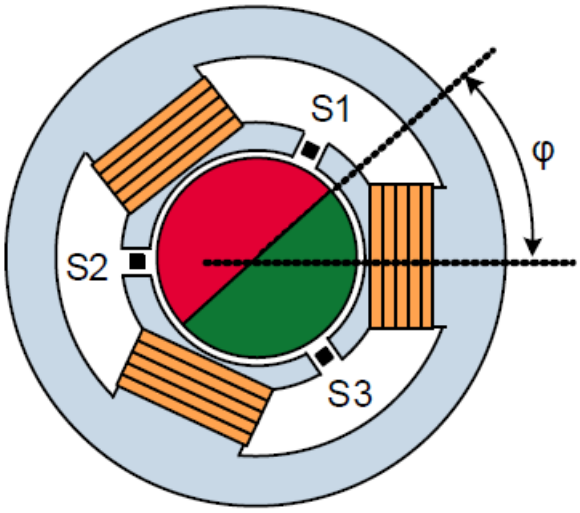

Figure 1 - 4: Brushless DC motor with 1 maget pole pair mounted on rotor and 3 phases. The magnetic field is sensed by 3 Hall-effect switches located at 120° phase angle. Image taken from [3], p. 5

The crucial advantage of this setup is the smaller inertia of the rotor and consequently the higher efficiency of the motor. Furthermore there is no mechanical wear due to the absence of the mechanical contact between stator and rotor. In standard motors a high current is driven through the brushes, which can lead to sparks inducing high electro-magnetic emissions.

The benefits of the brushless DC motor also come at a price, which is mainly the higher system complexity for driving electronics and the need for rotor position feedback sensors.

A commonly used feedback principle as shown in Figure 1 - 5 relies on three Hall-effect switches located at 120° phase angle triggered by a permanent magnet with one pole pair. Over one 360° rotation of the rotor this constellation delivers a signal pattern as depicted in Figure 1 - 5.

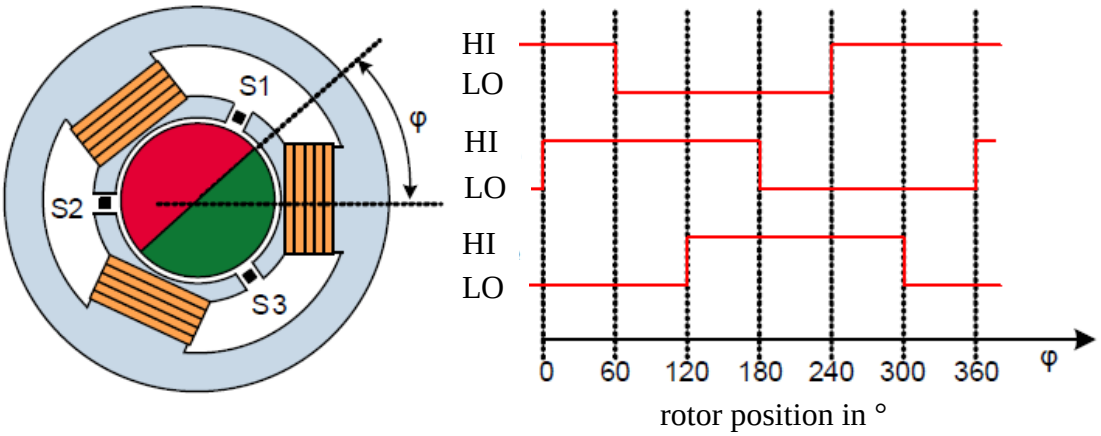

Figure 1 - 5: Hall effect switching pattern over 360° rotation
Image taken from [3], p. 7

The signal envelopes deliver a new digital state at every 60°. It is therefore possible to know the rotor position with a resolution of 60°. A pulse-width modulated signal (PWM) can be used to power the excitation coils. This so called block commutation is suitable for many applications demanding for low accuracy such as for example HVAC blower motors. More complex systems, as for example electrical power steering (EPS), demand more accurate feedback methods like sinusoidal commutation.

A disadvantage of this block commutation might arise in case of defective sensors. The three Hall switches are placed inside the motor, where they are exposed to high temperatures and vibrations. Replacing defective parts is laborious and expensive.

To overcome this issue one can use a separate magnet mounted on the rotating shaft outside of the motor housing. Here temperatures are significantly lower and maintenance is easier. On the downside this configuration results in higher costs due to the additional permanent magnet. For this setup GMR sensors are particularly suited as they deliver an absolute position of the motor shaft. As major advantage only one GMR sensor instead of three Hall-effect switches is required and the resolution is considerable higher. This system allows higher precision feedback for smoother motor torque control as required for instance in the EPS system, which relies on servo motors with sinusoidal commutation.

1.3 Hall effect

The Hall Effect was discovered by Edwin Hall in 1879. It describes the voltage arising when a current is flowing through a Hall plate exposed to a perpendicular external magnetic field.

If there is an external magnetic field perpendicular to the moving direction of charged particles, then the Lorentz force acts on each particle and pushes it to the side.

$$\vec{F}_L = q * (\vec{v}\ x\ \vec{B})$$

$\vec{F}_L$… Lorentz force q… charge $\vec{v}$… velocity vector $\vec{B}$… magnetic flux density

The Lorentz force is perpendicular to both the external magnetic field and the moving direction of the charged particles. Hence charges accumulate on one side of the conductor while a charge deficiency arises on the opposite side. This causes an electrical field and an electrical force which countervails the Lorentz force.

$$\vec{F}_{el} = q * \vec{\mathrm{E}}$$

$\vec{F}_{el}$… Electrical force $\vec{\mathrm{E}}$… Electrical field

Figure 1 - 6 illustrates a sketch of the Hall plate. Typically it is a small, thin squared device of length l, width w and thickness t. The Hall Effect is present in any conductor. Basically any conductor can be used for the plate, but the semiconductor industry prefers silicon as the electron mobility is rather high and it allows integrated solutions.

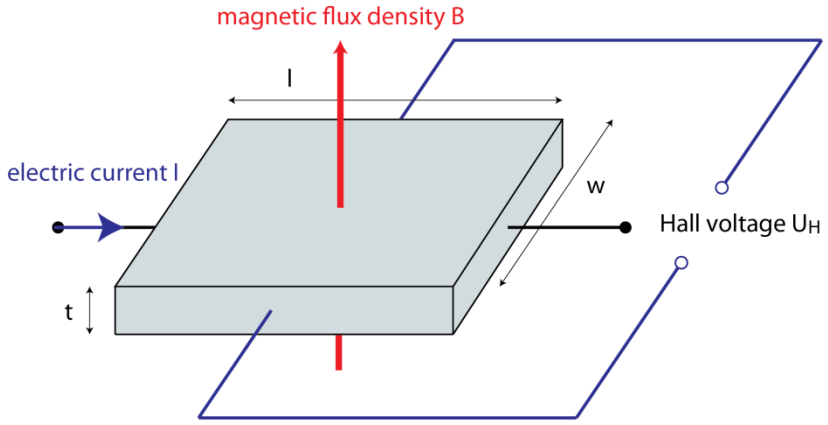

Figure 1 - 6: Schematic picture of a Hall plate.
The Hall voltage is perpendicular to the current direction and the applied magnetic field. Image based on [4]

The Hall voltage is transversal to the current direction. It can be expressed by the following equation.

$$V_H = R_H * \frac{B * I}{t}$$

V_H… Hall voltage R_H… Hall constant t…thickness of the Hall plate

$$R_H = -\frac{1}{n * q}$$

n… charge carrier density

The Hall voltage is linear proportional to the current and the magnetic flux density, inversely proportional to the thickness of the plate. It is independent from the resistivity of the material. The Hall constant is inversely proportional to the charge carrier density. Metals have a high charge carrier density. Thus the Hall constant and also the Hall voltage are small. Semiconductors offer a lower charge carrier density. Therefore the Hall voltage is higher [4], [5].

1.4 AMR effect

The AMR effect was discovered by William Thomson (Lord Kelvin) in 1857. It describes the resistance change in ferromagnetic materials depending on the orientation of a magnetic field. If the magnetization vector points in the same direction as the current vector (aligned or anti-aligned) the resistance will reach its maximum. However if the magnetization direction is oriented orthogonal to the current direction, the resistance is minimal.

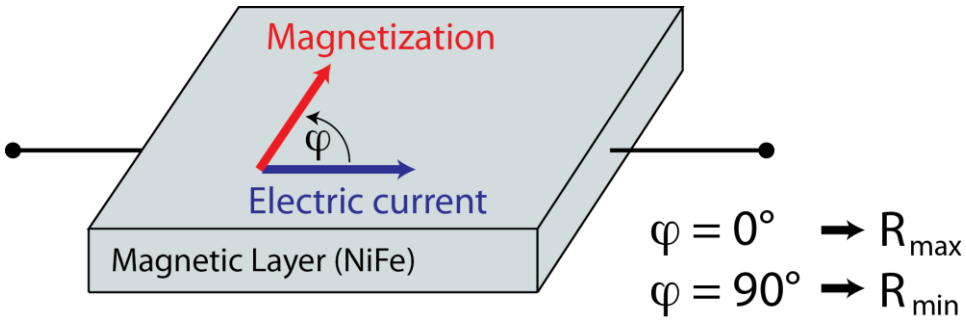

Figure 1 - 7: The AMR effect.
The resistance reaches its minimum when the magnetization is perpendicular to the electric current direction. For parallel or anti-parallel orientation of the current and the magnetization vector the resistance reaches its maximum. Image based on [6], p. 6

The resistance depending on the orientation of the external magnetic field can be described using the following equation.

$$R = \frac{R_{max} + R_{min}}{2} + \frac{R_{max} - R_{min}}{2} * \cos(2\varphi)$$

The angle φ is the angle between the magnetization vector and the current vector. R_{max} and R_{min} correspond to the maximum and minimum resistance of the material in the magnetic field.

The resistance change over a 360° rotation of the external magnetic field corresponds to two sinusoidal periods and is typically about 3% of the resistance in absence of an external field. Using a single AMR element due to the 2φ-periodicity the unique angle

detection over 90° is possible. By grouping four MR elements in a Wheatstone bridge one can sense small changes in resistance and compensate temperature influences.

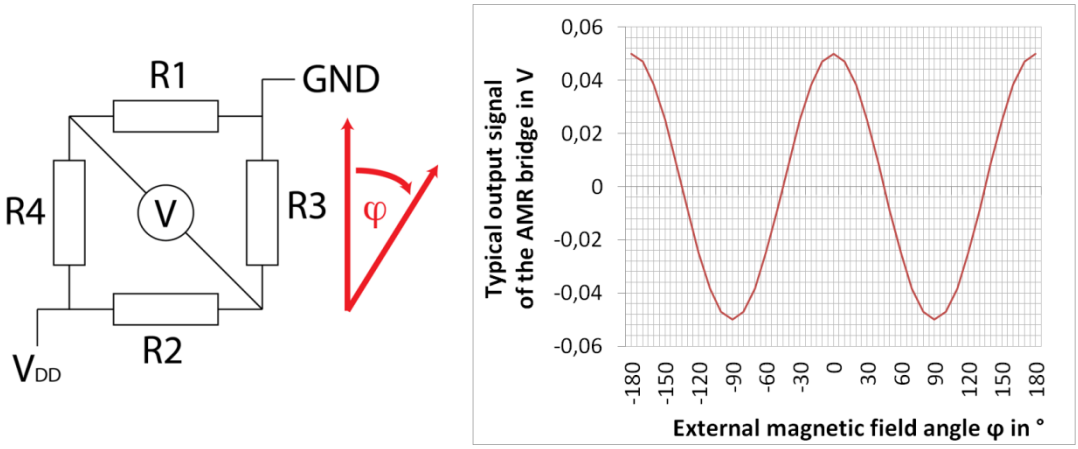

Figure 1 - 8: Output signal of an AMR Wheatstone bridge over 360°. Image based on [6], p. 7

Additionally one can use a second Wheatstone bridge rotated by 45°, which delivers a 45° phase shifted signal. With the trigonometric arc tangent function unique angle detection over 180° is possible [6].

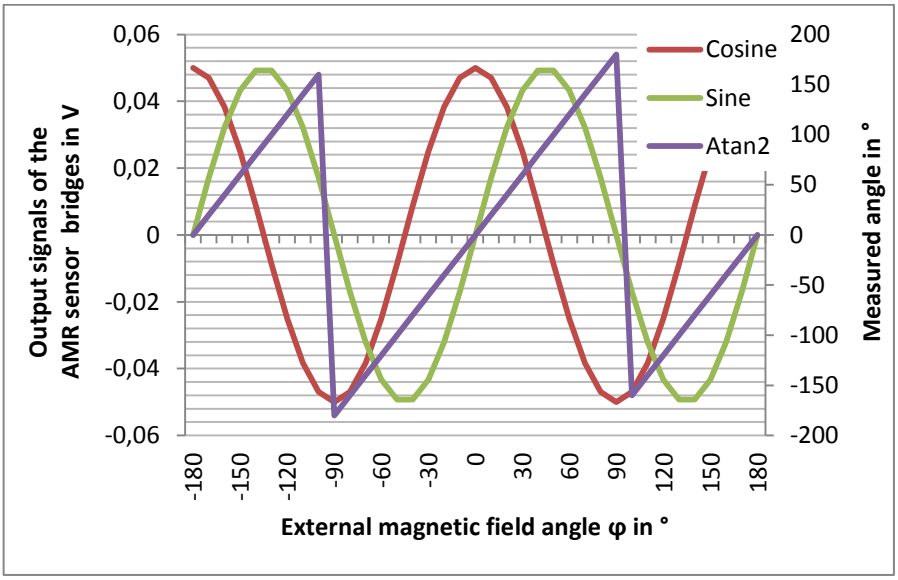

Figure 1 - 9: Output signals of two Wheatstone bridges oriented at 45° to each other and corresponding arc tangent. Image based on [6], p. 8

1.5 GMR effect

This chapter is concerned with a short introduction to the Nobel Prize winning giant magneto resistive (GMR) effect. It was discovered by Peter Grünberg and Albert Fert in 1988. Detailed information can be found in [7], [8], [9] and [10]. The GMR effect is a quantum mechanical effect occurring in alternating layers of ferromagnetic and non ferromagnetic materials. The overall resistance in this structure changes depending on the orientation of two magnetic fields. For anti-parallel alignment of these layers the resistance is significantly higher than for parallel alignment. The magnetic layers consist of nickel, cobalt or iron, while the spacer layer is a non-ferrous metal or a noble metal like copper.

Infineon Technologies use the so called spin valve stacks for their GMR sensors. The stack is depicted in Figure 1 - 10.

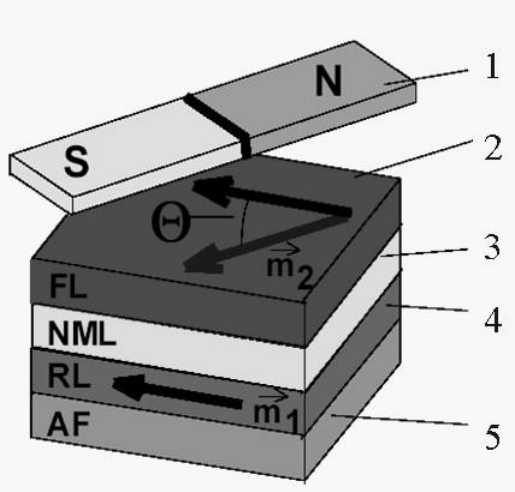

Figure 1 - 10: GMR Spin Valve Stack.
The magnetization direction of the free layer FL (2) follows the direction of the external field (1). The reference layer RL (4) has a pinned magnetization direction. The resitance of the non magnetic layer NML (3) changes depending on the orientation of the magnetization in Layer 2 and 4. Image taken from [8], p. 2

Basically it consists of two ferromagnetic layers (2 and 4), separated by a non ferromagnetic spacer layer (3). The reference layer (4) has a fixed magnetization direction. The magnetization in the free layer (3) follows the orientation of the external magnetic field (1). The resistance changes depending on the orientation of the two ferromagnetic layers. Figure 1 - 11 shows the resistance change depending on the angle between the reference and free layer.

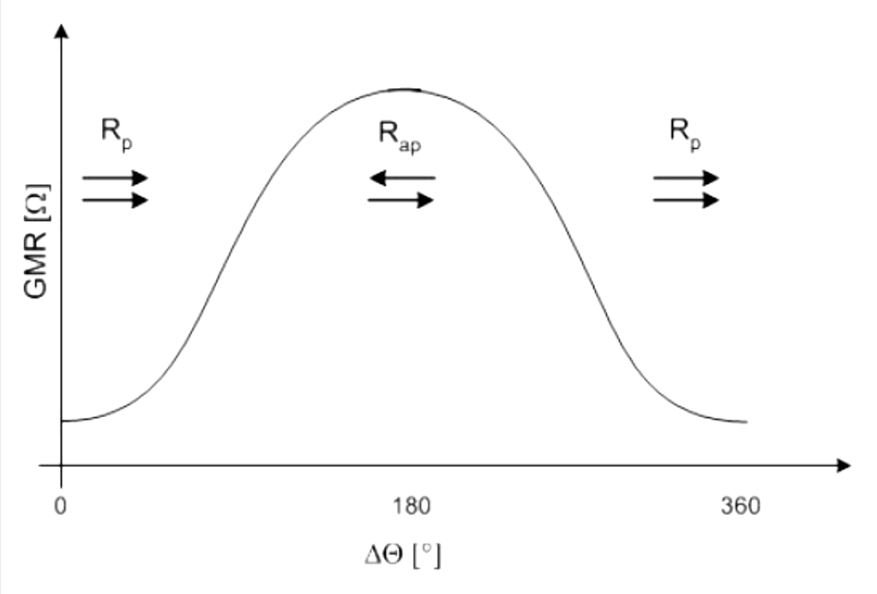

Figure 1 - 11: GMR Resistance change depending on orientation of ferromagnetic layers. The arrows indicate the orientation between the magnetization direction of the reference layer and the free layer. Image taken from [9], p. 4

The resistance depends on the orientation of the two ferromagnetic layers and can be described by the following equation.

$$R = \frac{R_{ap} + R_p}{2} + \frac{R_{ap} - R_p}{2} * \cos(\theta)$$

R_{ap}… Resistance for anti-parallel orientation of reference layer and free layer

R_p… Resistance for parallel orientation of reference layer and free layer

As shown in Figure 1 - 11 by using a single GMR element only the unambiguous angle detection over 180° is possible. To cover the whole 360° range, one can use two Wheatstone bridges oriented orthogonally to each other. Figure 1 - 12 shows the sensor configuration of Infineon's TLE 5012B GMR sensor. The arrows in the resistors indicate the magnetization direction of the reference layer.

The output signals of the bridges depicted in Figure 1 - 13 represent the x and y component of the magnetic field. Using the trigonometric arc tangent function, the magnetic field angle can be calculated from the relation of these components.

$$\theta = \operatorname{atan}\left(\frac{V_Y}{V_X}\right)$$

V_X… Output voltage of the Wheatstone bridge representing the B_X component

V_Y… Output voltage of the Wheatstone bridge representing the B_Y component

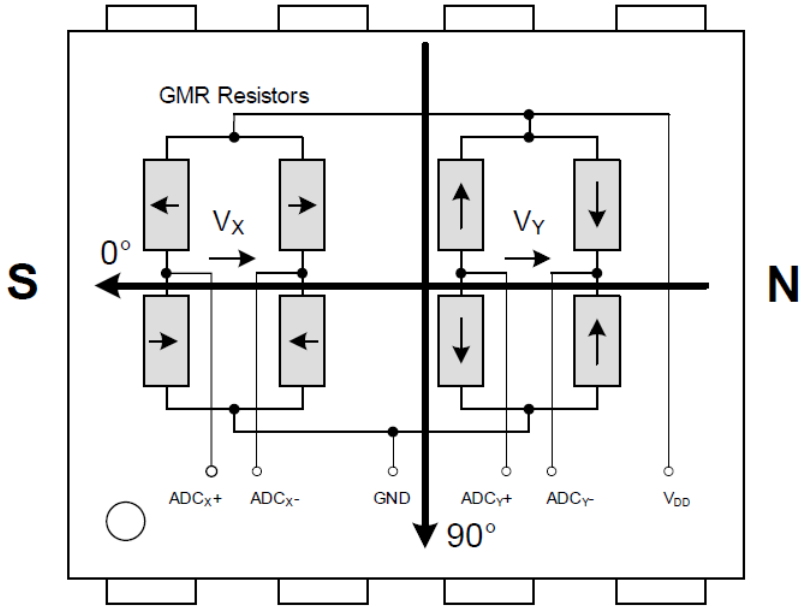

Figure 1 - 12: TLE5012B Sensitive Area.
There are two Wheatstone bridges oriented at 90° to each other.
Image taken from [10], p. 10

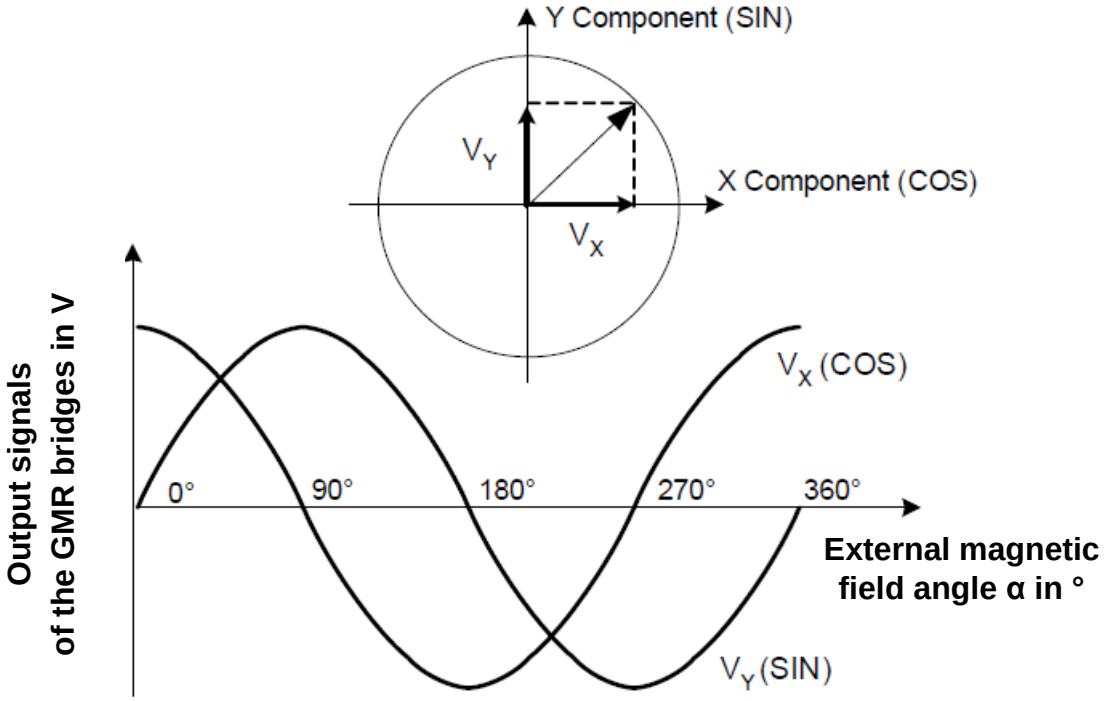

Figure 1 - 13: Output signals of the two Wheatstone bridges.
Image based on [10], p.11

1.6 xMR vs. Hall

This section shows a comparison between the sensors relying on the three magnetic effects outlined in the previous chapter. The Hall sensor is a device which measures the field strength of exactly one component of the magnetic field. The Hall voltage is directly proportional to the applied magnetic field. In contrast to the Hall sensor the xMR sensors do not measure the field strength but rather the field direction. This is the substantial difference between these sensor technologies. Since the Hall sensor measures only one field component, at least two Hall sensors are required for the angle measurement application. In case of the xMR technology one sensor is sufficient, as one sensor already senses two field components.

AMR sensors are sensitive to very low field variations and need only a few mT to operate correctly. The maximum magnetic field strength is not restricted. The major disadvantage is the limited measurement range of 180°. The GMR sensor on the contrary covers the whole 360° range. The maximum field strength however is restricted and

must not be exceeded. For instance the magnetic field induction of Infineon's TLE5012B angular sensor has an absolute maximum rating of 125 mT. Exceeding the absolute maximum rating will damage the sensor, as the reference layer in the spin valve stack will change its pinned direction. Typical GMR sensors require a magnetic field in the range of 30 to 50 mT to operate properly [10].

2 Magnetic Signal Modeling and Simulation

2.1 Introduction

This chapter is concerned with the modeling and simulation of the magnetic circuit. Therefore only raw B-field components are considered. Influences of the sensor and electronics in general are neglected in this chapter. The goal is to find an out of axis measurement concept delivering a highly accurate and absolute shaft angle. In chapter 3 relying on the found system also influences of the electronics will be taken into account.

Beside well known standard systems a new approach for accurate out of axis shaft angle measurement will be presented. It consists of a software algorithm relying on the so called Vernier principle (Nonius principle), which will also be described in this chapter. Optionally the algorithm can be combined with a new hardware measurement setup, delivering outstanding results. The new measurement system is a central contribution of this master thesis.

In this chapter a lot of magnetic circuit simulations are performed. This is done using software packages relying on finite element method (FEM) simulations. The programs used are Ansoft Maxwell v14.0, Ansys Mechanical v13.0 and Ansys Design Modeler v13.0.

Figure 2 - 2 shows the simplest form of a magnetic out-of-axis angle measurement system. There is a diametrically magnetized ring magnet mounted on the rotating shaft. A sensor placed at distance d from the magnet is measuring the x and y components of the magnetic field. This measurement setup is called “Top Read”. Beyond this there is another typical setup called “Side Read” as illustrated in Figure 2 - 1, where the sensor is located below the magnet and also senses the x and y components of the magnetic field.

Figure 2 - 1: Typical Side Read Setup
The sensor is located below the magnet and senses the x and y component of the magnetic field

For simulation efficiency instead of rotating the magnet and calculating the magnetic field for each new position, the magnet is left at its initial position and the sensor is moved around the magnet's circumference. Note that the sensor is also rotating as it moves around the magnet. In reality of course the magnet is rotating while the sensor is left at its fixed position. Anyway for both constellations the resulting field components at the sensor locations are the same.

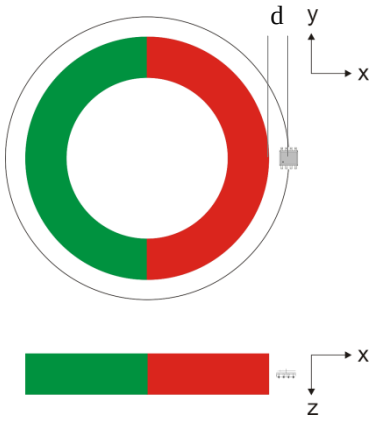

Figure 2 - 2: Magnet with 1 pole pair and Top Read setup:
The sensor is located at distance d and senses the x and y components of the magnetic field. The grey circle represents the movement path of the sensor. The sensor also rotates while circling around the magnet

Figure 2 - 3 shows the magnetic field components over a full mechanical rotation of the shaft.

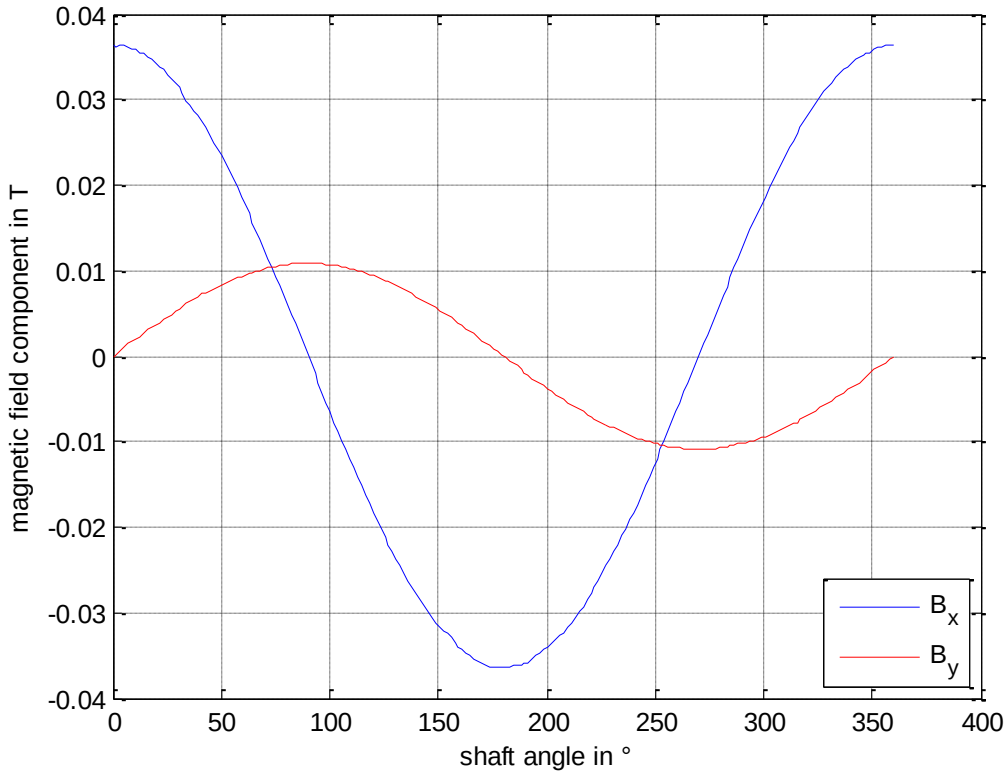

Figure 2 - 3: x and y component of the magnetic B-field over one revolution of the shaft

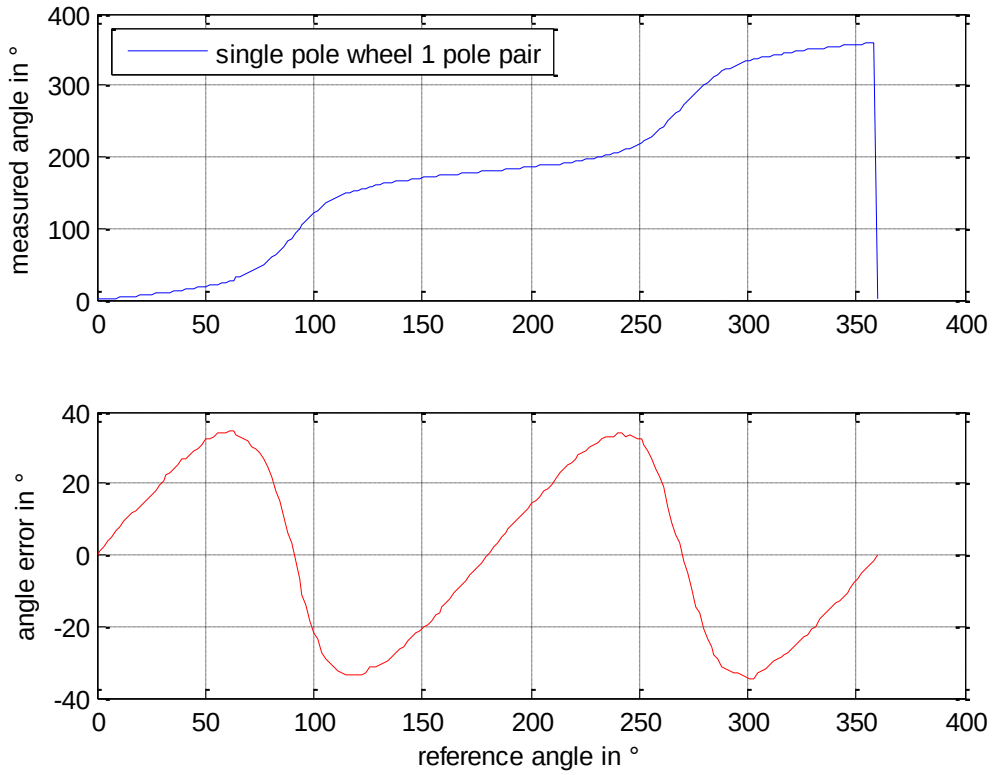

Figure 2 - 4: Measured angle of a magnet with 1 pole pair over one revolution of the shaft. The corresponding angle error depicted in the lower plot is about +/-35°

The measured angle over a 360° rotation of the shaft is depicted in the upper plot of Figure 2 - 4. The lower plot shows the corresponding angle error. The angle error is defined as the deviation from a perfect straight line ranging from 0° to 360°. In this simulation the pole wheel has an outer radius of 30 mm, an inner radius of 20 mm and a height of 10 mm. The sensor is placed 5 mm beside the magnet. As visible in the plot, the error is about +/- 35°, which is simply too high for high precision position feedback motor control. This error is obtained assuming an ideal sensor at that. It is the error arising from the raw B-field components caused by the magnet itself. Errors introduced by the signal processing are not considered at this time. Thus the angle is calculated by

$$\theta = \operatorname{atan}\left(\frac{B_Y}{B_X}\right)$$

The high error results from the different sized peak amplitudes. As visible in Figure 2 - 3 the amplitude of the x component is more than 3 times higher than the amplitude of the y component. The different sized amplitudes can be described by the amplitude synchronism [10], which is defined as

$$k = 100 * \frac{A_X}{A_Y}$$

Ideally the amplitudes of both components should be the same, thus having a synchronism of 100%. Figure 2 - 5 shows a polar plot where the magnetic field strength is depicted as a function of the mechanical shaft angle. Here the non-synchronism of the magnetic field component amplitudes leads to an elliptical shape of the field magnitude with slightly magnitude decreases occurring at the transitions form north-to-south and south-to-north pole (at 90° and 270°). Ideally the plot should show a circular shape. Different technology dependent parameters of real sensors additionally affect the angle error. These parameters will be discussed in chapter 3.

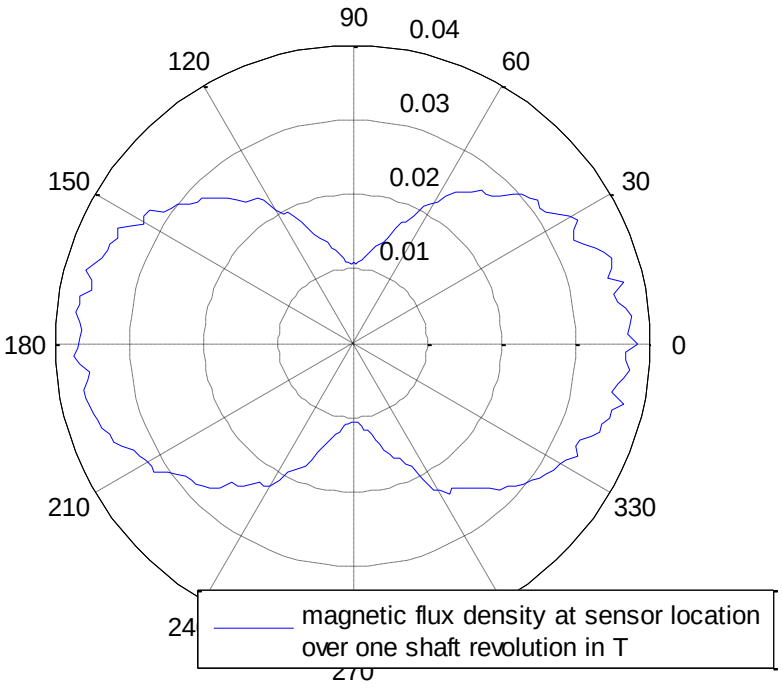

Figure 2 - 5: Magnitude of magnetic field vector in T.
The elliptical shape results from the non-synchronism of the magnetic field component amplitudes. At the pole transitions the field magnitude is weaker

Of course one could argue why not storing the deviations from the reference angle in a lookup table (LUT) and simply correcting the measured angle by these values. Basically this is possible, but some parameters have to be taken into account. First of all the deviations strongly depend on the geometric dimension of the pole wheel and also on the sensor location. Additionally the error drifts over temperature variations. Thus compensating the errors would require a three dimensional LUT and an elaborate calibration procedure to determine the values for this LUT. This results in high effort for setting up the measurement system. Another problem arises if due to sensor influences the measured angle over the mechanical rotation is not unique anymore. Then there is also no unique correspondence between the measured angle and the values in the LUT. Because of these issues the intention of this work is to find an out of axis angle measurement system already delivering accurate results without the need of an elaborate calibration process.

A convenient method of improving angle accuracy is to increase the number of pole pairs on the magnet. Figure 2 - 6 shows a pole wheel with two pole pairs. The pole wheel has the same geometric dimensions as in the previous simulation. The resulting angle and its corresponding error are depicted in Figure 2 - 7.

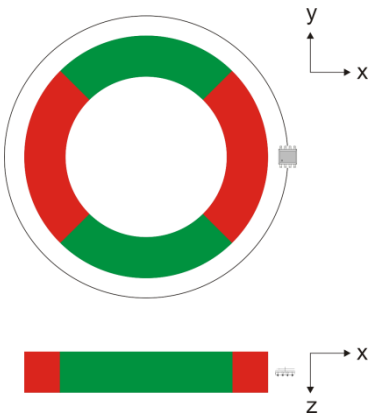

Figure 2 - 6: Magnet with 2 pole pairs and Top Read setup.
Again the sensor senses the x and y components of the magnetic field.

As the pole width decreases also the non-synchronism of the field amplitudes gets smaller. Therefore the error decreases to about +/- 28°. But there arises a central problem by raising the number of pole pairs: As shown in the upper plot of Figure 2 - 7 each pole pair excites its own 360° stroke. Thus the measured angle is ambiguous over the mechanical 360° rotation and the absolute shaft position cannot be determined. Assuming a GMR-based angle sensor each pole pair excites one signal period. The measured angle in the upper plot is denoted as electrical angle. Its corresponding error is the electrical angle error. To get the mechanical angle error the electrical angle error has to be divided by the number of pole pairs.

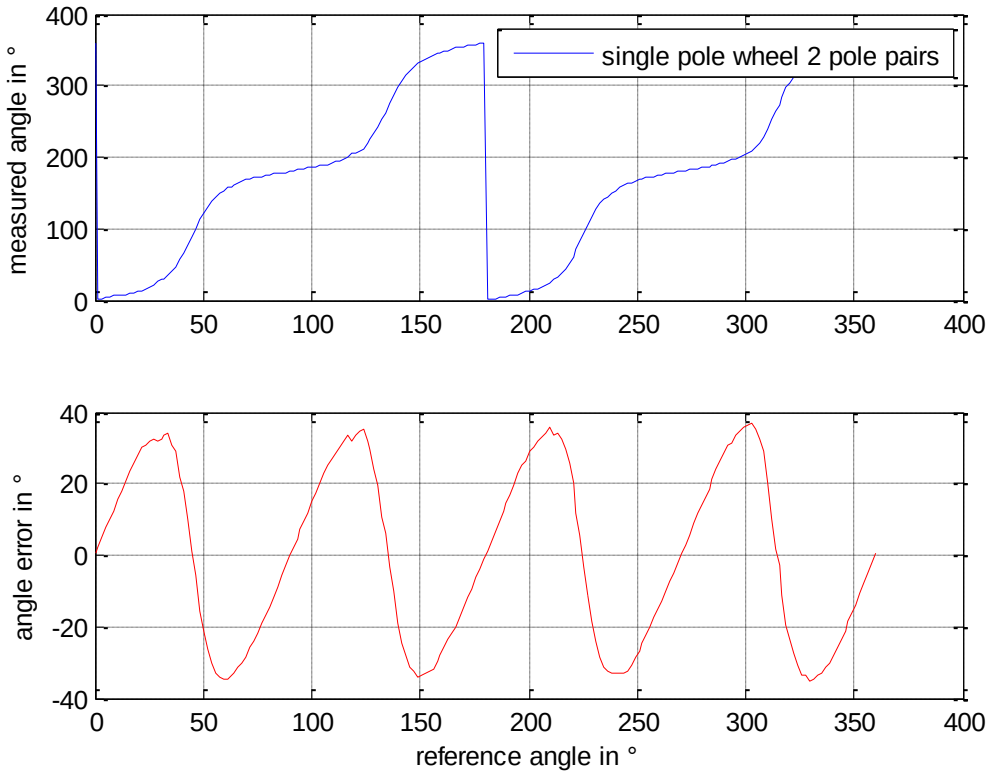

Figure 2 - 7: Measured angle of a magnet with 2 pole pairs over one revolution of the shaft. The corresponding angle error depicted in the lower plot is about +/-28°

There exist various system proposals for accurate and absolute angle detection. Some of the most promising systems are introduced and discussed in the following subchapters. Thereafter a new and powerful angle measurement system partly relying on the standard systems will be introduced. Its core is formed by an algorithm which drastically reduces the absolute angle error.

2.2 Vernier Principle

As described in Chapter 2.1 it is not possible to measure an absolute shaft angle using a single pole wheel with multiple pole pairs and an xMR-based sensor. With an AMR sensor one can detect the absolute angle position within one pole. In case of the GMR sensor due to the distinct angle range of 360° one can determine the absolute position within one pole pair.

The Vernier Principle allows absolute shaft angle detection over a 360° rotation by combining the signal information of two sensors triggered by two pole wheels. The pole wheels have the same geometric dimension but different number of pole pairs [6]. Figure 2 - 8 illustrates the measurement setup.

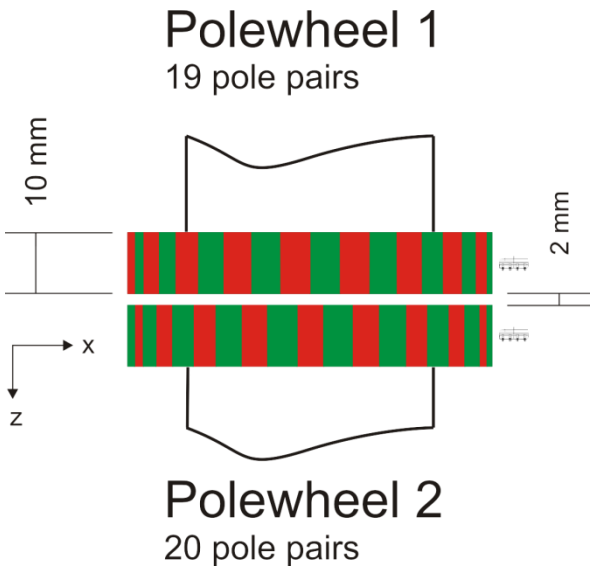

Figure 2 - 8: Basic setup of a Vernier principle.
There is a coarse pole wheel with 19 pole pairs and a fine wheel with 20 pole pairs. Again the sensors sense the x and y components of the magnetic field.

In this simulation there are two pole wheels with 19 and 20 pole pairs mounted on the shaft. Again the geometric dimensions equal those of the previous simulations (R = 30 mm, r = 20 mm, h = 10 mm). Two GMR-based sensors placed in “Top Read” configuration 3 mm beside the magnets sense the x and y components of the magnetic field. Using the arc tangent function the electrical angle can be calculated from these components. The upper plot in Figure 2 - 9 shows the electrical angle measured by each sensor. The absolute angle is obtained by subtracting the electrical angles of the sensors:

$$\theta_{NONIUS} = \theta_{FINE} - \theta_{COARSE}$$

θ_{NONIUS}… Vernier angle θ_{FINE}… Angle of pole wheel with (x + 1) pole pairs

θ_{COARSE}... Angle of pole wheel with x pole pairs

Thereafter to correct overshoots a modulo operation is performed on the Vernier angle.

$$\theta_{NONIUS} = mod(\theta_{NONIUS}, 360)$$

The resulting angle of the Vernier calculation is depicted as the green line in the upper plot of Figure 2 - 9.

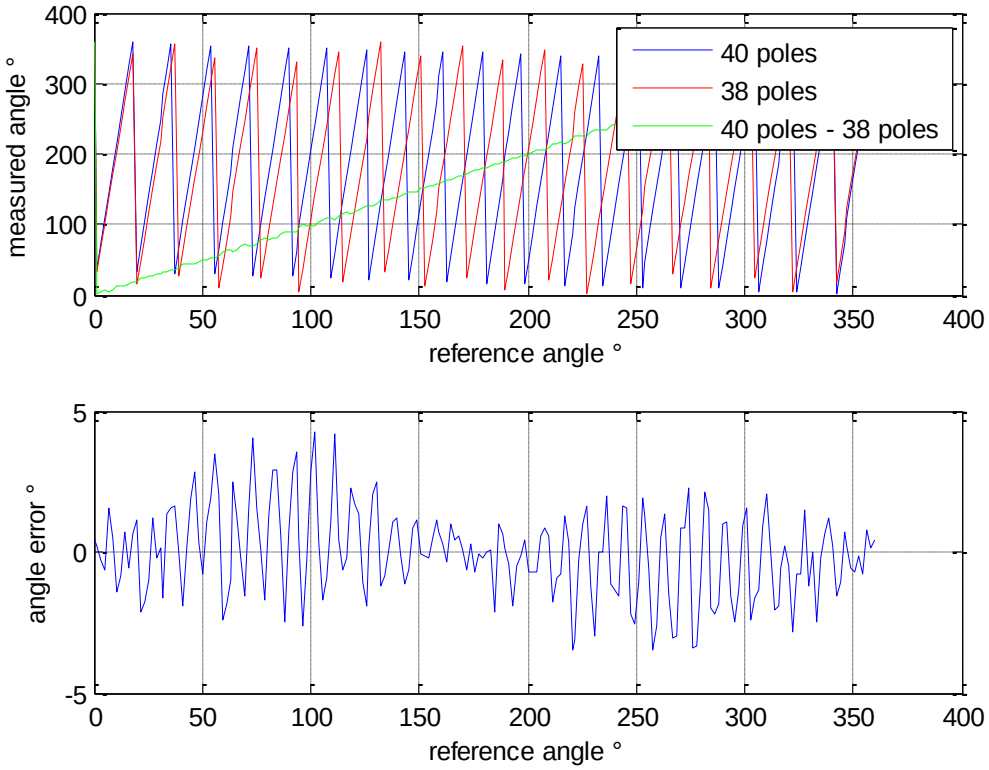

Figure 2 - 9: Vernier angle and corresponding error over mechanical 360° rotation. The resulting maximum error is about +4.23° / -3.50°.

As shown in the plot the Vernier angle is unambiguous over the mechanical 360° rotation. Unfortunately this method has a crucial drawback. While in theory both sensors deliver highly accurate angles and thus a highly accurate absolute angle, in practice angle errors deteriorate the result. In worst case the two maximum electrical errors of the single pole wheels sum up additive and result in a mechanical angle error, which is considerable higher than the error of the single wheels. Thus while the electrical angle errors of the single wheels are small, the error increases by the Vernier operation. While the error of the single wheels in the simulated example is about +/- 2.50° the resulting Vernier error depicted in the lower plot of Figure 2 - 9 lies between +4.23° and – 3.50°.

2.3 Two-Probe Principle relying on field strength measurements

An important parameter for accurate angle measurement using field strength sensors is the so called amplitude synchronicity of the sensor output voltages representing the B-field components. According to Infineon standards it is defined as $k = 100 * (Ax / Ay)$ [10]. Ideally the amplitudes have the same size. Thus the arc tangent of the relation of these two signal amplitudes delivers a perfect circular shape over 360°. In practice the amplitudes representing the B-field components will be slightly different, which leads to a non-linear variation of the measured angle. Correcting the signal amplitude of one component by a simple gain factor already improves the accuracy.

A more sophisticated approach for amplitude correction is the two-probe principle proposed by MMT [11]. The measurement setup is depicted in Figure 2 - 10.

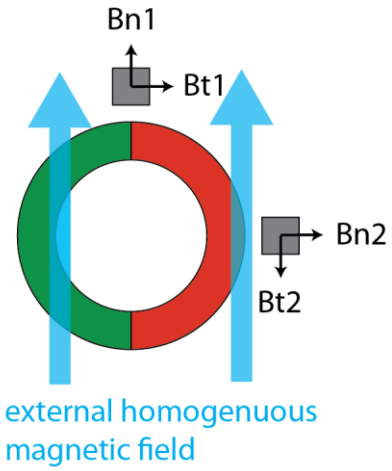

Figure 2 - 10: Two-Probe Principle. Two Hall ICs located at 90° sense the radial and tangential components of the magnetic field. Image based on [11], p. 4

The idea is to combine the signal information of two Hall ICs located at 90° by the following equations:

$$B_n = B_{n1} + B_{t2}$$

$$B_t = B_{t1} + B_{n2}$$

This configuration leads to proper sine and cosine signals having same amplitudes that reduce the non-linearity of the measured angle over a full mechanical 360° rotation. As a convenient side effect this method cancels out the effects of an external homogenous magnetic field. This can be very useful in case where the sensor is placed close to the motor and can be influenced by the poles.

Unfortunately this two-probe principle cannot be realized with xMR sensors. As already mentioned xMR sensors do not sense the field strength and thus the amplitudes, but rather the field direction.

2.4 Combining incremental with absolute position signals

This method was originally proposed in [12]. The basic idea is to combine the signal information of a speed sensor with the absolute angle measured by a GMR angle sensor. The setup is illustrated in Figure 2 - 11.

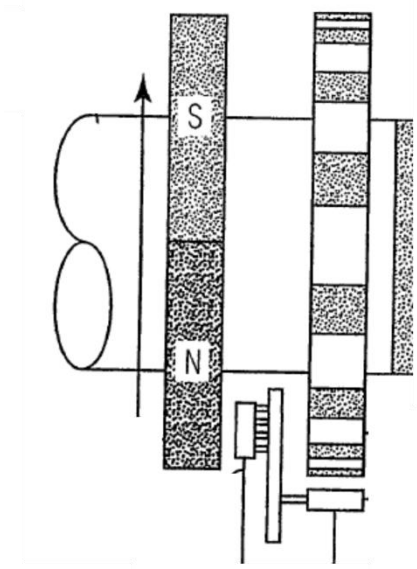

Figure 2 - 11: Setup for combining incremental with absolute position signals.
The GMR sensor faces the diametrically magnetized ring magnet and delivers an absolute but inaccurate angle. This signal is corrected with the incremental information of the second sensor. Image taken from [12], p. 23.

There is a diametrically magnetized ring magnet mounted on the rotating shaft. Additionally there is a second encoder wheel mounted next to the magnet. This wheel is typically a cogwheel sensed by a speed sensor with a back bias magnet or a magnetic pole wheel. The GMR sensor can either be placed in “Top Read” or in “Side Read” configuration as illustrated. As already shown this configuration delivers an absolute but erroneous angle. The error is typically about +/-35°. Consider for example a cogwheel with 60 cogs. In this case the rising and falling edges trigger the speed sensor every 3°. The timing of the edges is highly accurate. Thus the speed sensor delivers an angle corresponding to the straight line as depicted in Figure 2 - 12. The dashed vertical lines symbolize the rising and falling edges. At these positions the angle is known in advance.

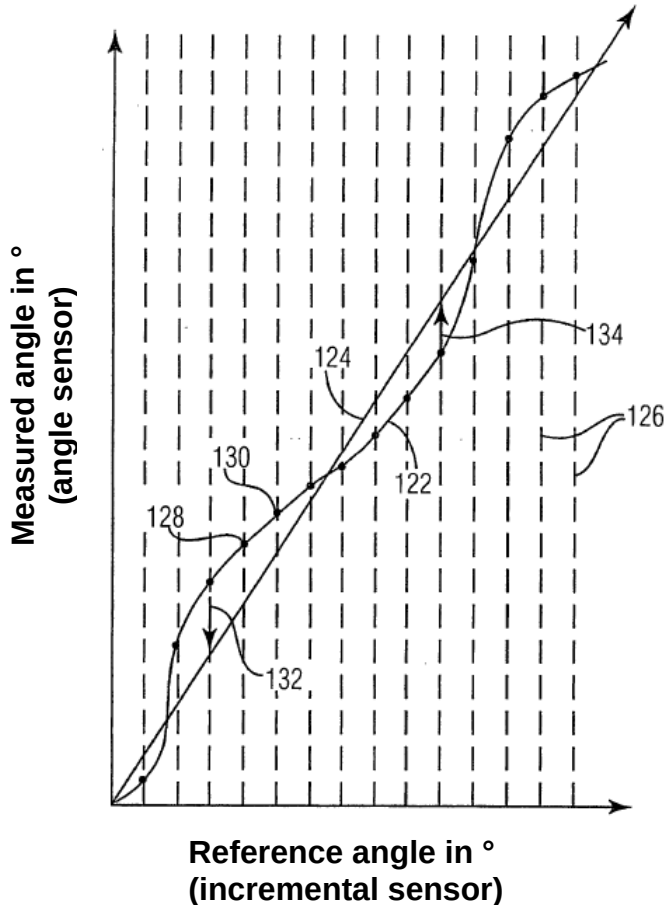

Figure 2 - 12: Measured angle over mechanical 360° rotation.
The dashed lines symbolize the signal delivered by the speed sensor. The curved line is the angle measured by the GMR sensor. Image taken from [12], p. 19.

The curved signal is the one delivered by the GMR sensor. Based on the incremental speed sensor signal the erroneous GMR sensor signal can be corrected. For this method a monotonically non-decreasing GMR angle curve is required. Otherwise there is no unique correspondence between the GMR angle and the incremental signals. Another drawback is the missing true power on capability, which means that the true angle is available right after startup.

2.5 A new approach for out-of-axis angle measurement

In the following two sections a new approach for accurate out of axis angle measurement is presented. It consists of a new software algorithm that improves the accuracy of the standard Vernier principle. Additionally this algorithm can be combined with a new hardware measurement setup. Basically these two inventions can be applied independently from each other. But in combination they deliver outstanding results. This new out of axis angle measurement system is a central contribution of this thesis.

The new algorithm relies on a modification of the standard Vernier principle in combination with a new two-probe principle, which is also suitable for GMR-based angle sensors. The system requires at least two pole wheels and two sensors. Another sensor can be added according the new two-probe principle to achieve even higher accuracies. In this section the software algorithm will be described. In Chapter 2.6 the new two-probe principle will be explained.

The measurement setup equals the one of the Vernier principle in Chapter 2.2. There are two pole wheels mounted on a rotating shaft. Each wheel is sensed by a GMR-based angle sensor, placed beside the wheel and measuring x and y components of the B-field. Again the system consists of a coarse pole wheel with x pole pairs and a finer wheel with (x+1) pole pairs. In the simulation two wheels with 19 and 20 pole pairs are used. The sensors are placed 3 mm beside the magnets. The only difference is the applied algorithm for calculating the absolute angle.

The system makes use of a sophisticated algorithm to improve the accuracy of the standard Vernier principle. Instead of simply calculating the phase difference between the output angles, the algorithm determines the output angle by counting the actual signal period. This is done as follows:

First the Vernier angle is calculated

$$\theta_{NONIUS} = \theta_{FINE} - \theta_{COARSE}$$

A modulo operation is performed on the Vernier angle to correct overshoots.

$$\theta_{NONIUS} = mod(\theta_{NONIUS}, 360)$$

This angle already roughly indicates the position within the signal curve.

Next the corresponding signal period of the fine pole wheel can be determined by

$$Threshold = \frac{360°}{pole\ pair\ number\ of\ fine\ wheel}$$

$$Signalperiod\ Number = \left\lfloor \frac{\theta_{NONIUS}}{Threshold} \right\rfloor$$

Once the signal period is known, the new and more accurate output angle can be calculated by

$$\theta_{NEW} = Threshold * Signalperiod\ Number + \frac{\theta_{FINE}}{pole\ pair\ number\ of\ fine\ wheel}$$

Since the Vernier angle is erroneous, the correct signal period cannot always be determined correctly. In some cases the calculated signal period number will be off by one. This results in high error peaks having an amplitude of +/- $Threshold$. This situation is illustrated in Figure 2 - 13.

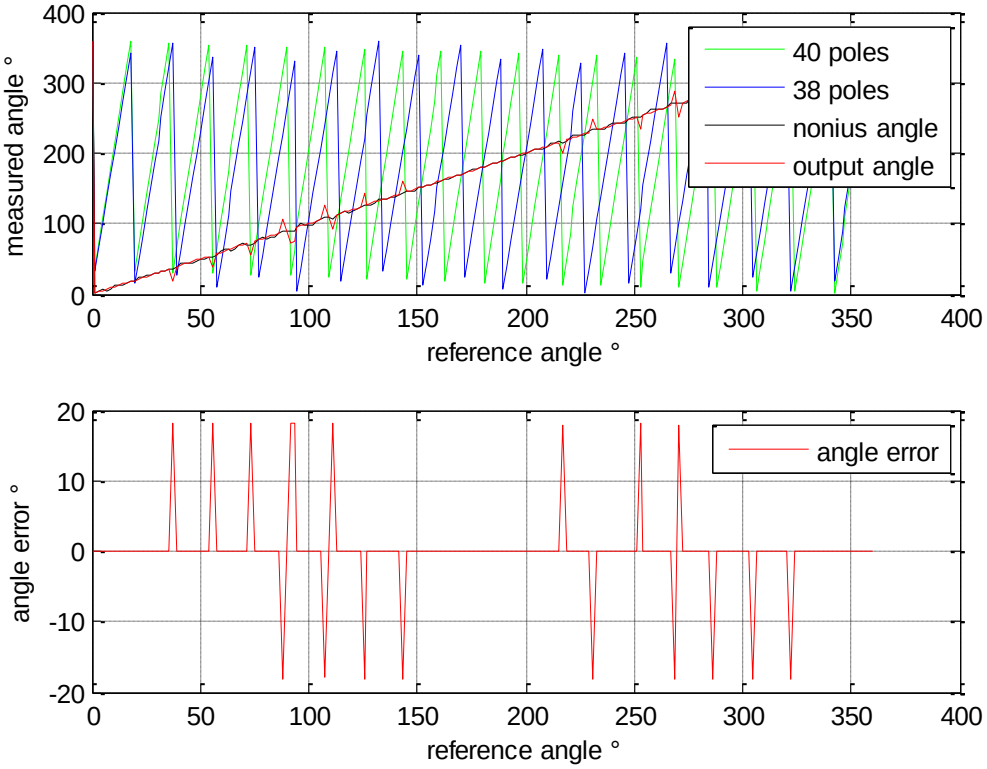

Figure 2 - 13: Resulting angle and corresponding error.
Without threshold correction there occur high error peaks

To overcome this issue the error peaks can be removed by comparing the new angle θ_{NEW} to the Vernier angle θ_{NONIUS}. If the difference is bigger than the maximum Vernier error, than $Threshold$ is subtracted from θ_{NEW}.

$$IF\ \theta_{NONIUS} - \theta_{NEW} > \max\ (abs(Error_{NONIUS}))$$

$$\theta_{NEW} = \theta_{NEW} - Threshold$$

Vice versa $Threshold$ is added if the difference is smaller than the minimum Vernier error.

$$IF\ \theta_{NONIUS} - \theta_{NEW} < -1 * \max\ (abs(Error_{NONIUS}))$$

$$\theta_{NEW} = \theta_{NEW} + Threshold$$

The resulting output angle after threshold correction and its corresponding error are depicted in Figure 2 - 14.

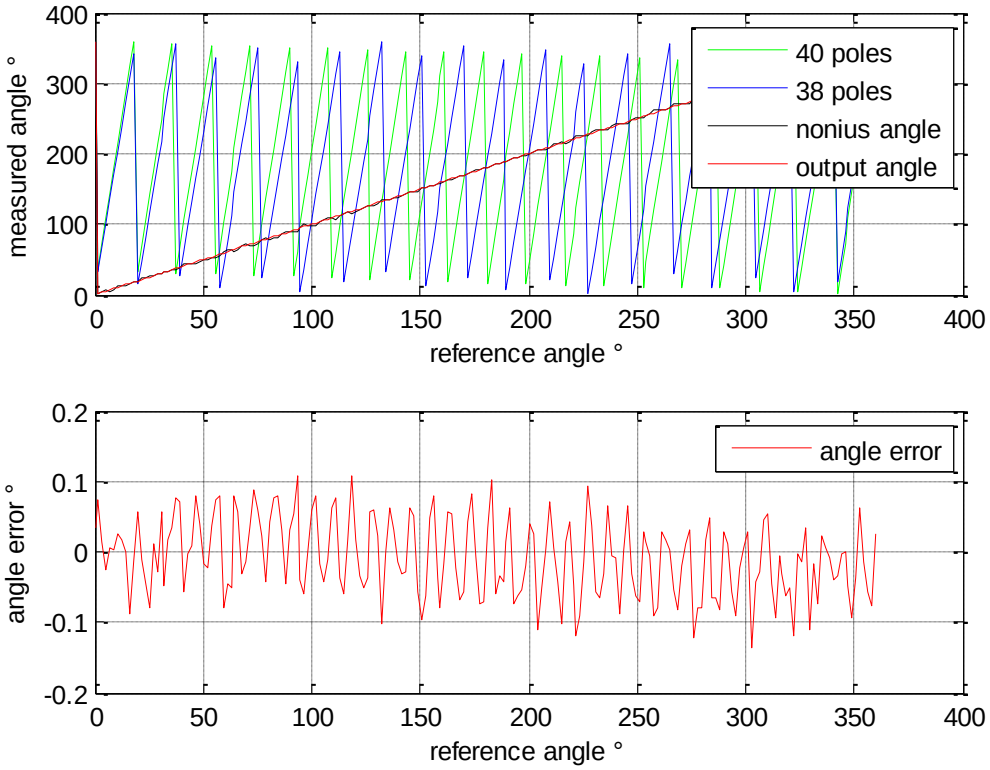

Figure 2 - 14: Resulting angle and corresponding error over mechanical 360° rotation using the new algorithm. Compared to the standard Vernier principle the error decreases from +4.23 / -3.50° to only +0.11° / -0.14°.

As one can see the error is very small compared to the Vernier error. It decreases from +4.23° / – 3.50° to +0.11° / -0.14°. Thus compared to the standard Vernier principle the proposed algorithm already delivers an accurate solution. In the next section a new two-probe principle suitable for GMR-based angle sensors is shown, which allows even higher accuracies.

2.6 A new two-probe principle relying on field direction measurements

In this section a new hardware measurement setup developed within this thesis is presented. This principle can be shown best using a practical example. For demonstration purpose it is shown using a diametrically magnetized ring magnet and a sensor placed in

“Top Read” configuration, but it also holds for higher pole numbers. The output angle of such a setup was already shown in Figure 2 - 4 at the beginning of Chapter 2. Ideally the output angle should correspond to a straight line over one mechanical 360° rotation. In reality as visible in the upper plot of Figure 2 - 4 it is an erroneous signal curve which deviates from the perfect linear line. The corresponding angle error depicted in the lower plot is small at a reference angle of 0°, 90°, 180° and 270°. At these locations the sensor is facing the middle of the pole or a pole transition respectively. At these locations one component of the B-field reaches its maximum while the other component is almost zero. Thus only one dominant component is present. As a result the non-synchronity of the amplitudes doesn’t affect the angle calculations and therefore the error is low. Between these accurate locations stronger deviations from the straight line occur. This implies placing an additional sensor exactly at the pole transition. Additionally this sensor is rotated with respect to the first sensor, that both sensors measure the same angle (with small deviations) at a time. In case of the diametrically pole wheel the sensor is rotated by 180° as illustrated in Figure 2 - 15.

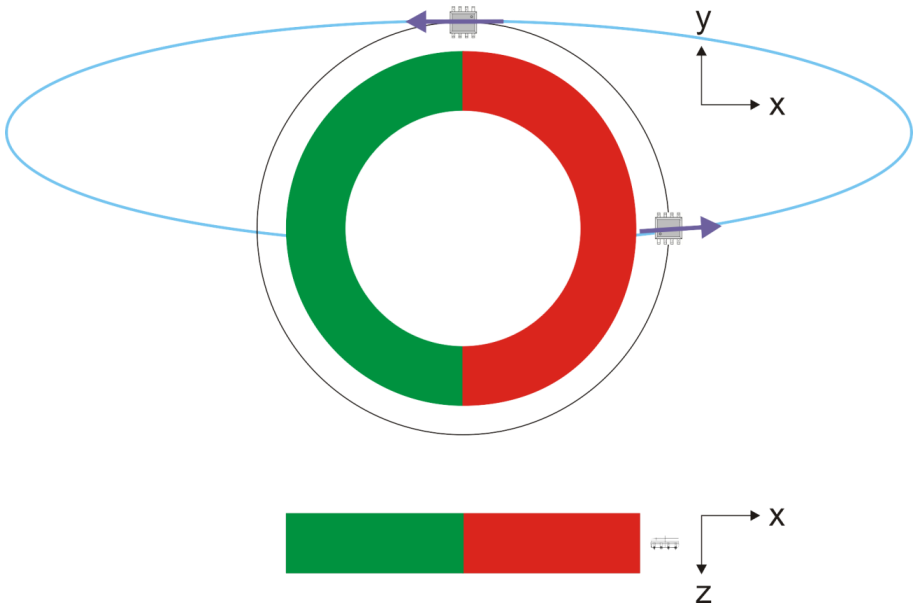

Figure 2 - 15: New two-probe principle using GMR sensors.
A second sensor is placed exactly at the pole transition. Additionally this sensor is rotated around its z-axis with respect to the first sensor, such that both sensors measure the same angle at a time. By calculating the mean angle of both sensors the deviations from the reference angle cancel out.

Figure 2 - 16 shows the angles measured by each sensor. As shown the additional sensor delivers the same angle as the first sensor shifted by 90°. By calculating the mean value of both angles, the deviations nearly cancel out. The result is a more accurate output angle. The error decreases from +/- 35° to +/- 9.4°.

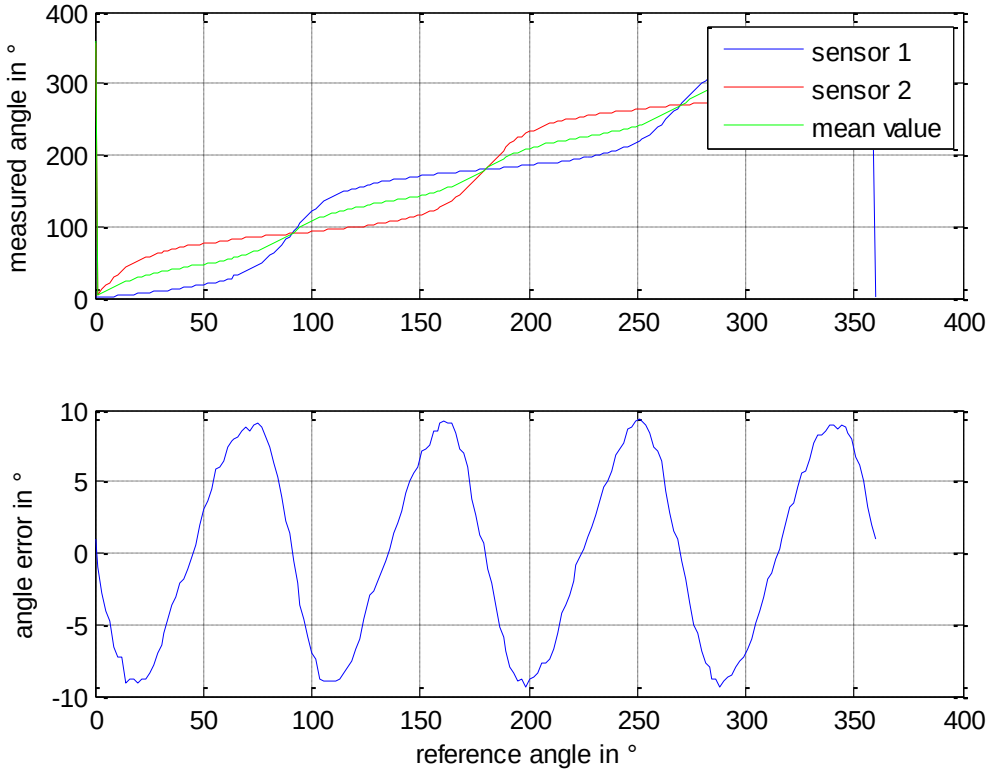

Figure 2 - 16: Result of the new Two-Probe principle.
By calculating the mean angle of both sensors the deviations from the reference angle cancel out. The error decreases from +/- 35° to +/- 9.4°.

As already mentioned this property also holds for higher pole numbers. Figure 2 - 17 illustrates a pole wheel with 4 pole pairs. In that case the second sensor has to be placed at the pole transition and rotated by $90° + 360°/(2 * Number\ of\ Poles) = 112.5°$.

The method can be applied to the proposed out-of-axis angle measurement system of the previous chapter and leads to even higher accuracies. The second sensor has to be added to the finer pole wheel (the wheel with the higher pole number). Adding the sensor to the coarse pole wheel is dispensable as it doesn't gain additional information in combination with the algorithm. Thus 3 sensors are sufficient to achieve highly accurate

results. Again using the setup with 38 and 40 poles the maximum angle error is about +/- 0.06° as shown in Figure 2 - 18.

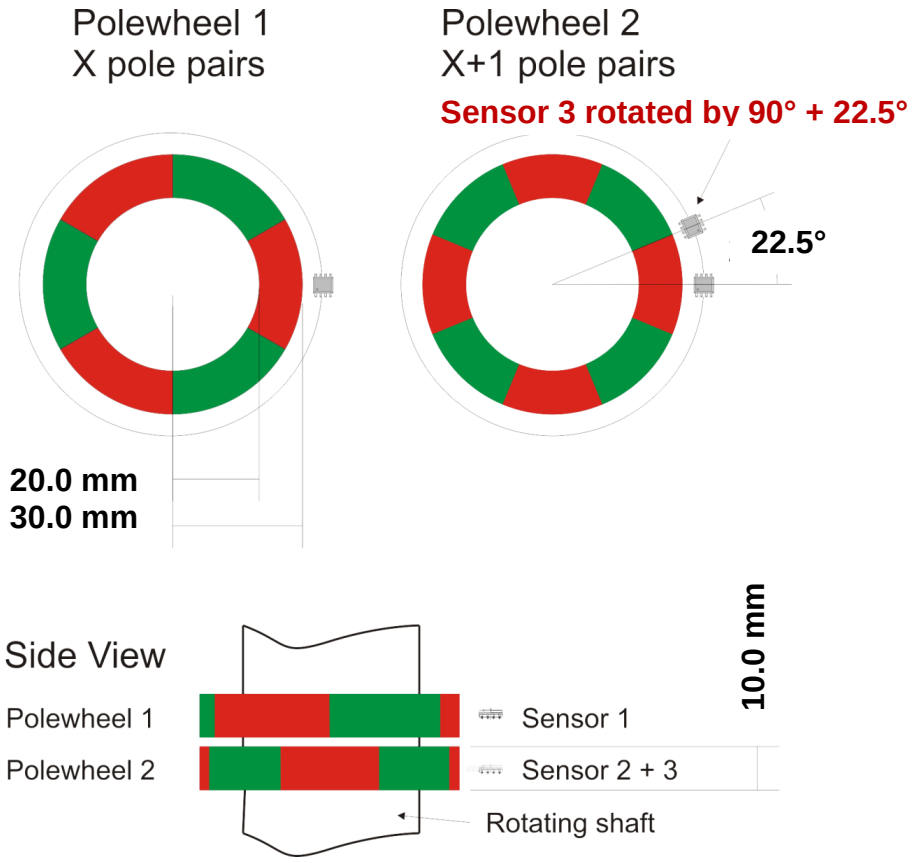

Figure 2 - 17: Measurement setup for highly accurate results. The third sensor is placed in front of the fine pole wheel exactly at the pole transition. Additionally it is rotated in a way that both sensors measure the same angle at a time

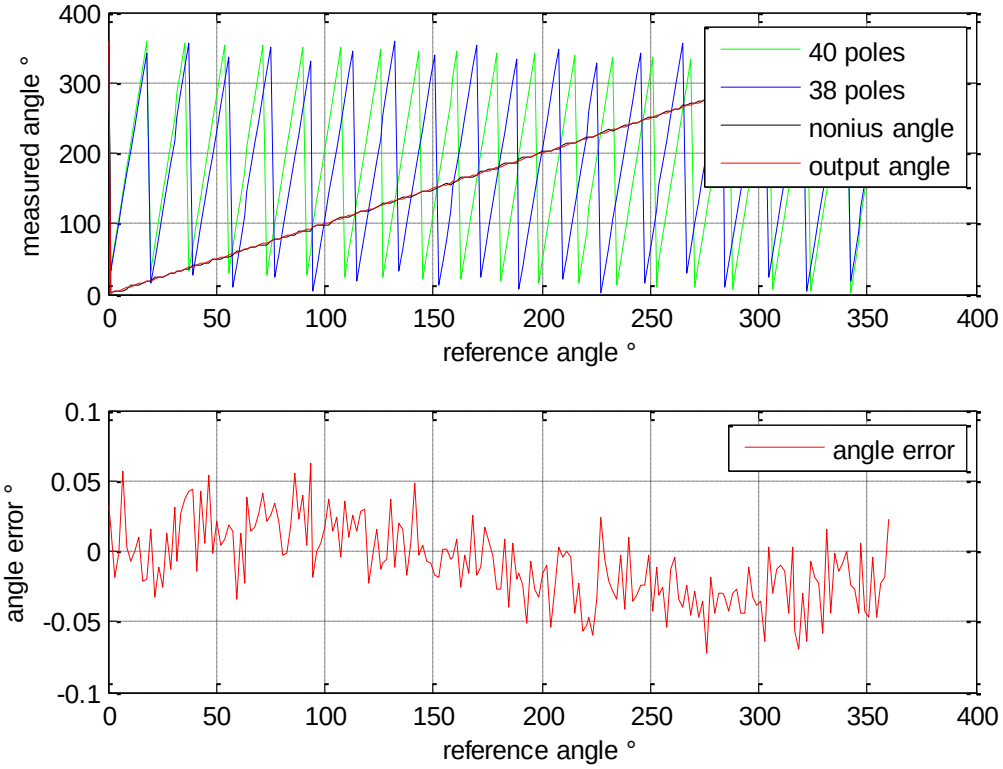

Figure 2 - 18: Result of the new two-probe principle using the proposed algorithm. The maximum angle error is about +/- 0.06°.

2.6 Further investigations

Of course the results of Chapter 2.5 and Chapter 2.6 are based on ideal conditions. The pole wheels are ideal, thus a perfect magnetization in reference direction leading to a constant pole width is assumed. There is no additional error considered due to mounting tolerances. In reality the accurate placement of the sensors and mounting the magnets on the shaft is a challenging task.

Non-ideal magnetization

To study the influences of non-ideal magnetization laboratory measurement protocols of existing pole wheels are used. According to measurements of Magnetfabrik Schramberg the maximum deviation from the reference pole width is 2.20%. For the simulation of the pole wheel with 20 pole pairs a uniform distribution of the magnetization error over the circumference of the wheel is assumed. This implies an alternating pole width: 20

poles have an increased pole width of 9.198° while the other 20 poles have a smaller width of 8.802°. As before the coarse wheel with 19 pole pairs is assumed to have an ideal magnetization. Again the proposed algorithm and the two-probe principle are applied. Figure 2 - 19 shows the result of the simulation. As shown the error raises to about +0.14° / -0.16°.

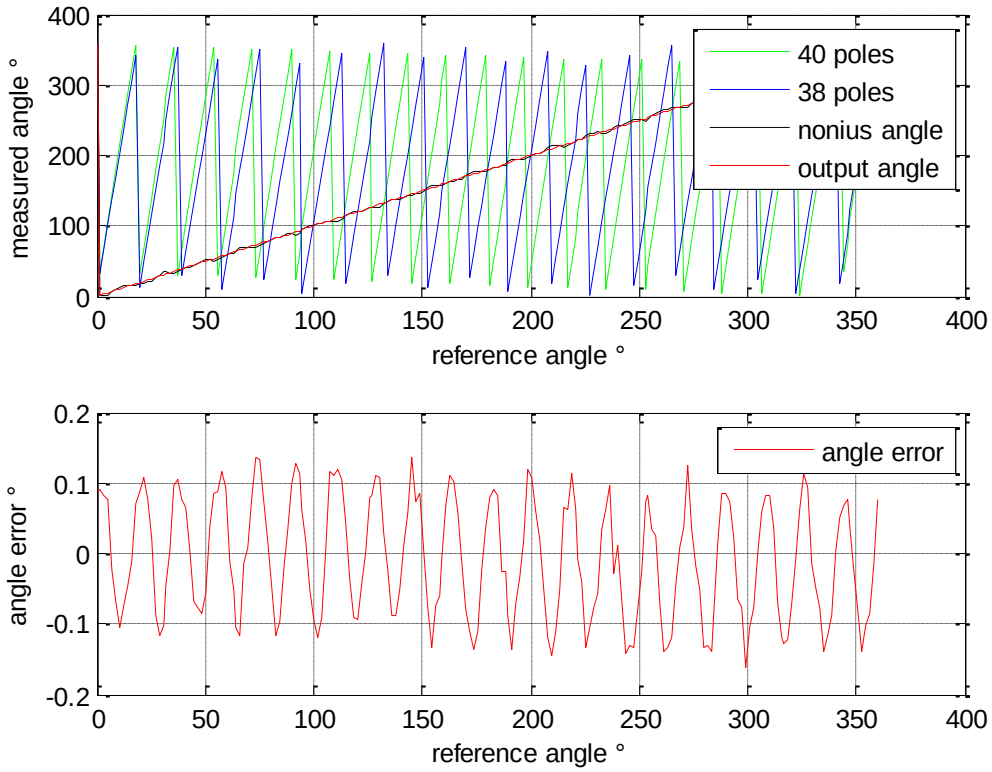

Figure 2 - 19: Result of non-ideal magnetization.
The finer pole wheel has an varying pole width. The deviation from the reference pole width is +/- 2.2%. The resulting maximum error is +0.14° / -0.16°

Optimum number of pole pairs

To obtain a minimum angle error the optimum number of pole pairs for a fixed pole wheel size has to be determined. This is done using the simulation results from the tables in Appendix A and plotting the angle error versus the pole pair number. All pole wheels have the same geometric dimensions. The inner radius measures 20 mm, the outer radius is 30 mm and the height is 10 mm. As material hard ferrite with a coercivity H_C = 140 kA/m and a remanence B_R = 0.22 T is used. As shown in Figure 2 - 20 the

electrical angle error is about +/- 26° for a pole wheel with 10 poles (5 pole pairs). Then by raising the number of poles the error decreases and reaches its minimum at about 38 / 40 poles (19 / 20 pole pairs). For higher pole number the error increases again.

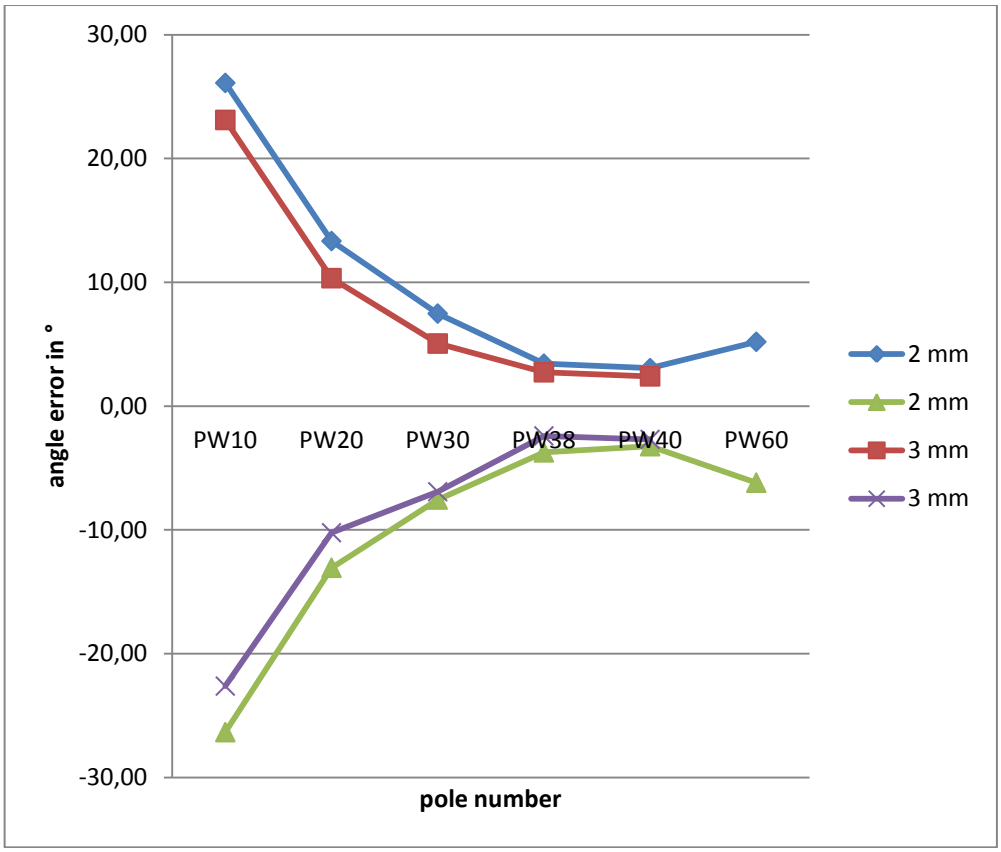

Figure 2 - 20: Electrical angle error versurs number of poles. The number of poles on the wheel is increased while keeping the geometric dimensions the same. The error reaches its minimum at 40 poles. For higher pole numbers the error increases again. Each curve represents a specific sensor distance.

3 Electrical Signal Modeling and Simulation

3.1 Introduction

So far the angle error was discussed considering only the raw magnetic field components and assuming an ideal sensor. In this chapter the sensor itself, including signal conditioning will be taken into account. The requirements in analog-to-digital conversion (ADC) are figured out and an adequate ADC type is proposed. Finally a MATLAB Simulink model of the out of axis measurement system is presented and the overall angle error is derived.

3.2 Sensor Parameters

So far the angle error was discussed assuming an ideal sensor. But there are also sensor-technology dependent parameters influencing the error which have to be considered. The information in this chapter was taken from [10] and [13].

In case of the GMR-based angle sensors there are three parameters which affect the angle calculations: These are the amplitude, the offset and the phase shift between the output signals of the Wheatstone bridges. Due to production tolerances and process variations these parameters cannot be considered as perfect.

The output signals of the bridges can be described by

$$X = A_X * cos(\theta + \varphi_X) + O_X$$

$$Y = A_Y * sin(\theta + \varphi_Y) + O_Y$$

X… Output voltage of the X bridge

Y… Output voltage of the Y bridge

A_X…Peak amplitude of X signal

A_Y…Peak amplitude of Y signal

φ_X…Phase of X signal

φ_Y…Phase of Y signal

O_X…Offset of X signal

O_Y…Offset of Y signal

Figure 3 - 1 illustrates these parameters.

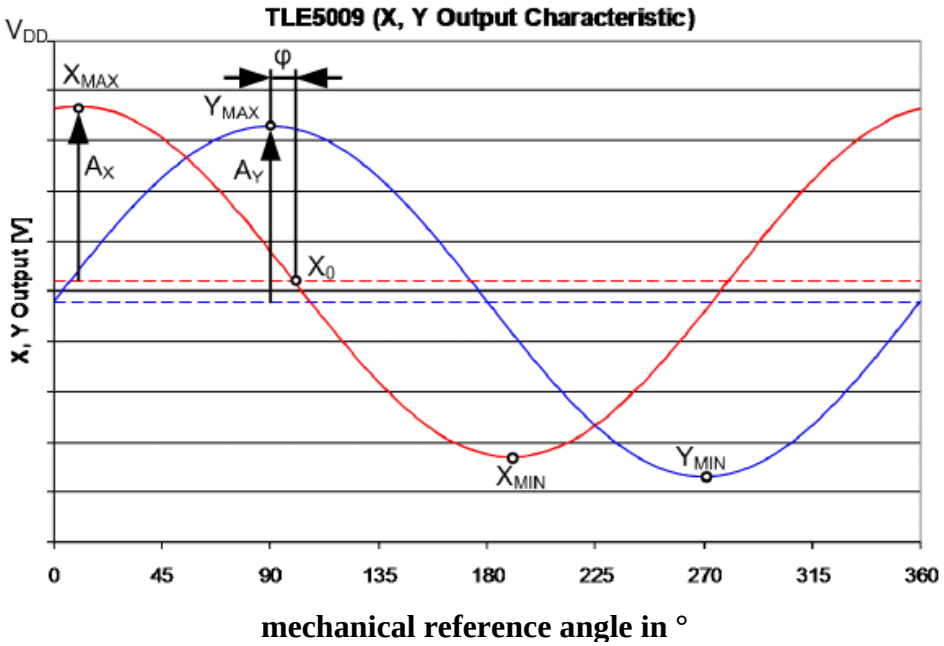

Figure 3 - 1: GMR sensor output signals and sensor parameters over one shaft revolution. The red and blue lines illustrate typical output voltages of the GMR sensor bridges. The offset voltages are illustrated as the dashed lines. Image taken from [14], p. 15.

Without parameter correction the output signal over one shaft revolution assuming a diametrically magnetized permanent magnet and the sensor placed ahead of it, would look something like illustrated in Figure 3 - 2.

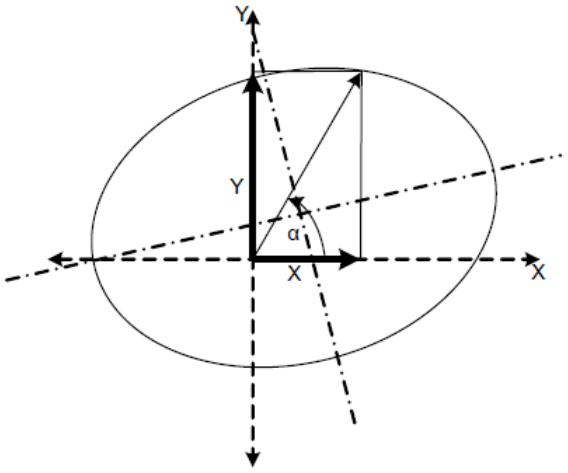

Figure 3 - 2: Angle performance without parameter correction over one mechanical rotation. The elliptical form mainly results from the non-synchronism and non-orthogonality of the x and y voltages. Image taken from [13], p. 7.

The elliptical form results from the non-synchronism and non-orthogonality of the x and y voltages, which is defined as

$$k = 100 * (\frac{A_X}{A_Y})$$

$$\varphi = \varphi_X - \varphi_Y$$

k… X,Y synchronism φ ...orthogonality

Ideally k should be 100% and φ = 90° resulting in an output signal corresponding to a circle with its center located at the origin. The good news is that these parameters can be corrected using the following calibration algorithm: Initially the amplitudes and offsets of both output voltages have to be determined.

$$A_X = \frac{X_{MAX} - X_{MIN}}{2}$$

$$A_Y = \frac{Y_{MAX} - Y_{MIN}}{2}$$

$$O_X = \frac{X_{MAX} + X_{MIN}}{2}$$

$$O_Y = \frac{Y_{MAX} + Y_{MIN}}{2}$$

Using these values the offset and amplitude correction can be performed.

$$X' = \frac{X - O_X}{A_X}$$

$$Y' = \frac{Y - O_Y}{A_Y}$$

Next the orthogonality error is corrected

$$X_{corr} = X'$$

$$Y_{corr} = \frac{(Y' - X' * \sin(-\varphi))}{\cos(-\varphi)}$$

The resulting angle after this correction is given by

$$\theta = \operatorname{atan}\left(\frac{X_{corr}}{Y_{corr}}\right) - \varphi_X$$

Figure 3 - 3 illustrates the angle performance after parameter correction. Now the output corresponds to a circular shape with its center in the origin.

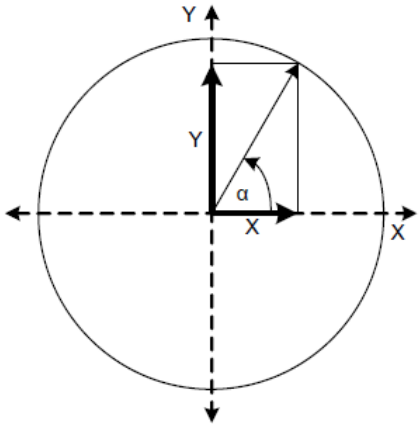

Figure 3 - 3: Angle performance after parameter correction.
The output angle corresponds to a circle. Image taken from [13], p. 8.

3.3 The GMR sensor bridge

As already mentioned the sensitive part of the GMR based angle sensor consists of two Wheatstone bridges oriented at 90° to each other. Each bridge measures one magnetic field component. The maximum signal amplitude strongly varies over temperature and magnetic field changes. Furthermore an offset might be superimposed to the signal which has an additional temperature and field coefficient. The influence of field strength variations is negligible, though. Finally there is an orthogonality error if the bridges aren't placed at exactly 90° to each other. These GMR technology parameters are summarized in Table 3 - 1.

Symbol	Parameter	Value	Unit	Comment
		typ		
V_{Peak}	Peak Amplitude	20	mV/V	@ 25°C
TCV_{Peak}	Temperature coefficient of peak voltage	-0.34	%/K	@ 25°C
HCV_{Peak}	Field coefficient of peak voltage	-0.02	%/(kA/m)	
V_{Offset}	Signal offset	+/- 2	mV/V	
TCV_{Offset}	Temperature coefficient of offset voltage	+/- 1	µV/V/K	
HCV_{Offset}	Field coefficient of offset voltage	+/- 0.1	µV/V/(kA/m)	
φ_{NO}	Signal non-orthogonality	+/- 2	°	
$TC_{\varphi NO}$	Temperature coefficient of non-orthgonality	0.0005	°/K	
$HC_{\phi NO}$	Field coefficient of non-orthgonality	-0.004	°/(kA/m)	

Table 3 - 1: Characteristics of the Wheatstone output voltages

The output signals can be characterized by the following equations:

$$V_X = V_{DD} * \left(V_{PeakX} * \left(1 + TCV_{PeakX} * \frac{dT}{100} \right) \right) * \left(1 + HCV_{PeakX} * \frac{dB}{100} \right) * \cos(\alpha) +$$

$$V_{DD} * \left(V_{OffsetX} + TCV_{OffsetX} * dT + HCV_{OffsetX} * dB \right)$$

$$V_Y = V_{DD} * \left(V_{PeakY} * \left(1 + TCV_{PeakY} * \frac{dT}{100} \right) \right) * \left(1 + HCV_{PeakY} * \frac{dB}{100} \right)$$

$$* \sin\left(\alpha + TC_{\varphi no} * dT + HC_{\varphi no} * dB \right) +$$

$$V_{DD} * \left(V_{OffsetY} + TCV_{OffsetY} * dT + HCV_{OffsetY} * dB \right)$$

Based on these equations the minimum and maximum bridge output voltages are calculated. The maximum anticipated signal amplitude is 81.6 mV occurring at a temperature of -40°C. With increasing temperatures the maximum amplitude decreases and reaches its minimum at 15.4 mV at 150°C. Figure 3 - 4 illustrates the maximum and minimum output voltages.

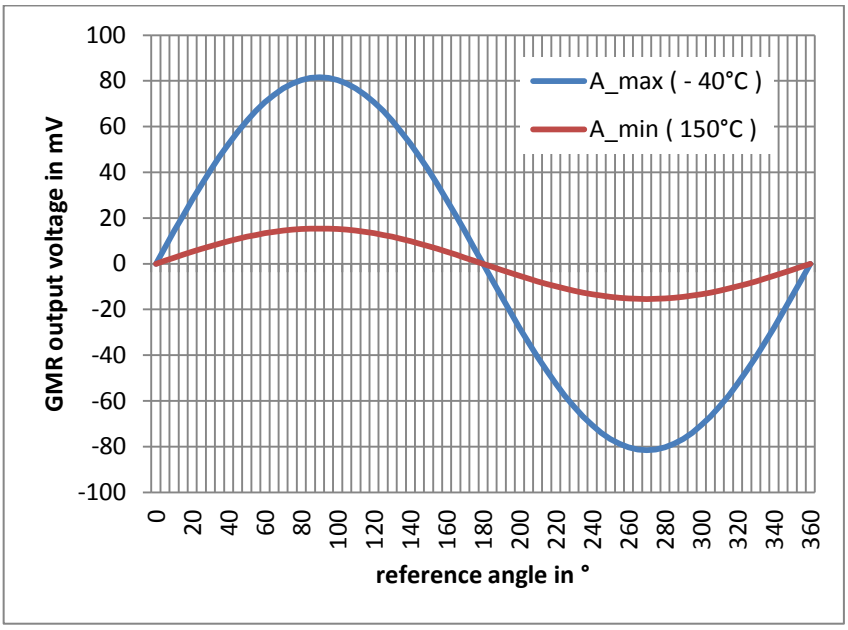

Figure 3 - 4: Minimum and maximum possible output voltages of the GMR Wheatstone bridges. The voltage varies strongly over temperature drifts.

3.4 Analog-to-digital conversion

In this chapter the requirements in analog-to-digital conversion (ADC) in terms of resolution and conversion rate are figured out. Thereafter two types of ADC are introduced, which match the requirements of the angle measurement system. The analog-to-digital conversion is necessary to transfer the output voltages of the Wheatstone bridges into the digital domain for further signal processing. Very small signal amplitudes have to be digitized. Thereby emerges quantization noise, as the continuous analog signal is mapped to a limited number of quantization stages.

The resolution of the ADC is specified in bits. The minimum resolution of the ADC ensuring accurate results can be determined by analyzing the output signals of the Wheatstone bridges. In the previous section the characteristics of the Wheatstone sig-

nals were discussed in detail. The maximum amplitude is about 81.6 mV at -40 °C. It decreases with increasing temperatures and reaches its minimum at 15.4 mV at +150 °C. To get an accurate system a minimum angular resolution of about 0.05° is desirable. This implies that a bit transition occurs at a minimum amplitude change of

$$V_{LSB} = \sin(angular\ resolution) * V_{min} = \sin(0.05\ °) * 15.4\ mV = 13.44\ \mu V$$

As visible in the equation the voltage corresponding to 1 LSB directly depends on the minimum output voltage of the Wheatstone bridge and the desired angular resolution. Note that in any analog-to-digital conversion emerges quantization noise in the range of +/- ½ LSB. Non idealities of individual ADC concepts additionally degrade the resolution. As a consequence the least significant bits don't carry useful information. Therefore some reserve is included by adding two additional bits. The resolution of the converter is increased and a worst case resolution of 0.05° is ensured.

$$V_{LSB} = \frac{13.44\ \mu V}{2^{2\ Bit}} = 3.36\ \mu V$$

The maximum output voltage of the Wheatstone bridge is 81.6 mV. To leave some headroom for the ADC the maximum input amplitude is set to 70% of the full scale reference voltage of the ADC.

$$V_{REF} = \frac{81.6mV}{0.7} = 117\ mV$$

Finally the required number of bits is calculated by

$$\frac{2 * V_{REF}}{3.36\ \mu V} = 2 * 34696.37$$

$$log_2(2 * 34696.37) = 16.08\ bit$$

Thus to achieve a worst case resolution of approximately 0.05° approximately 16 bits are needed.

Next the maximum occurring input frequency is considered. The signal frequency depends on the structure of the pole wheel and on the motor speed. The system is designed for a maximum speed of 15000 rpm. Assuming a diametrically magnetized pole wheel this corresponds to a 250 Hz sine wave at the output of the Wheatstone bridge. For higher pole numbers the frequency increases according to the pole pair number on the wheel.

$$f_s = \frac{15000\ rpm}{60\ s} * number\ of\ pole\ pairs \qquad [Hz]$$

The measurement system proposed in Chapter 2.5 and Chapter 2.6 utilizes a pole wheel with 20 pole pairs. Therefore the maximum occurring input frequency applied to the ADC is 5 kHz.

Figure 3 - 5 shows different types of ADCs for different resolutions and different input signal bandwidths. As visible the Delta-Sigma ADC is suitable for high resolution applications and an input signal frequency ranging from a few hundred Hertz up to some Megahertz.

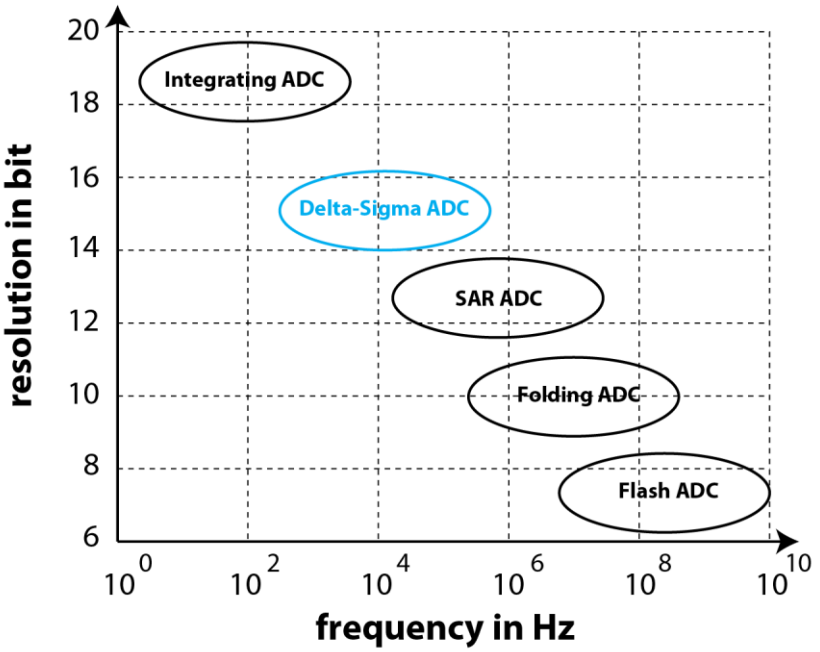

Figure 3 - 5: Different ADC concepts
trade resolution with input signal bandwidth. Image based on [15], ch. 3, p. 23.

The Delta-Sigma converter offers high resolution analog-to-digital conversion without the need for high precision analog building blocks. A lot of the conversion work is performed in the digital part of the converter. The analog part consists of some simple building blocks (Integrator, Comparator, Difference Amplifier). Due to a single bit DAC in the feedback loop, which outputs only two states the converter offers inherent linearity. A sample and hold block is dispensable due to high modulator frequency. Finally the ADC can be easily integrated using standard CMOS technology. These features make it a good choice for the out of axis angle measurement system [15], [16], [17].

Basically also a successive approximation register (SAR) ADC could be utilized. A serious drawback of the SAR architecture is the requirement that each of the analog building blocks has to be as accurate as the overall system, which leads to higher effort in system design. For the sake of completeness also the SAR architecture will be discussed in the next section.

3.4.1 SAR ADC

In this section the working principle of a Successive Approximation Register (SAR) ADC is introduced. Additionally a rough parameterization for the application in the angle measurement system is shown. The information in this chapter was taken from [18]. As the name already states a SAR ADC performs a binary search through all quantization levels to approximate the analog input voltage. Basically the SAR ADC consists of the building blocks depicted in Figure 3 - 6.

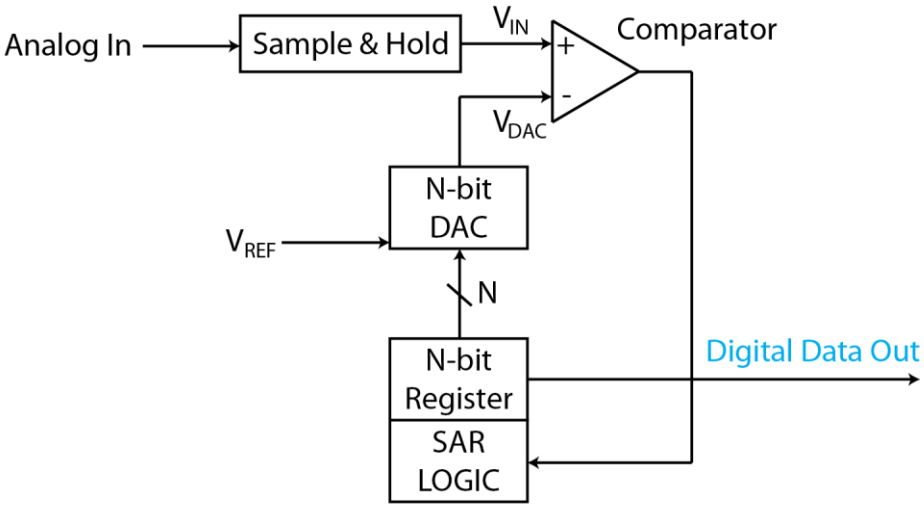

Figure 3 - 6: Block diagram of a SAR ADC.
Image based on [18], p. 2.

The conversion works as follows: First the most significant bit MSB in the SAR is set to 1 while the lower bits are initialized to 0 (100..000). This corresponds to a midscale range of the reference voltage V_{REF}. The DAC converts the digital value to an analog voltage V_{DAC}, which is $V_{REF} / 2$ in this case. The output voltage of the DAC is compared to the analog input signal V_{IN} of the ADC. If the input signal V_{IN} is smaller than V_{DAC}, the comparator output is 0 and the SAR logic sets the MSB to 0. If V_{IN} is greater than V_{DAC} the comparator output is 1 and the MSB remains at 1. Thereafter the SAR logic continues with the next bit and repeats the described steps. After N steps the resulting code can be read from the register.

One can see that N comparison periods are required for an N-bit ADC. During this process the input voltage must not change. Therefore the Sample and Hold block is re-

quired. A standalone sample and hold block is not always mandatory as many SAR ADC implementations offer an inherent sample and hold function integrated in the DAC. A typical capacitive DAC implementation is depicted in Figure 3 - 7.

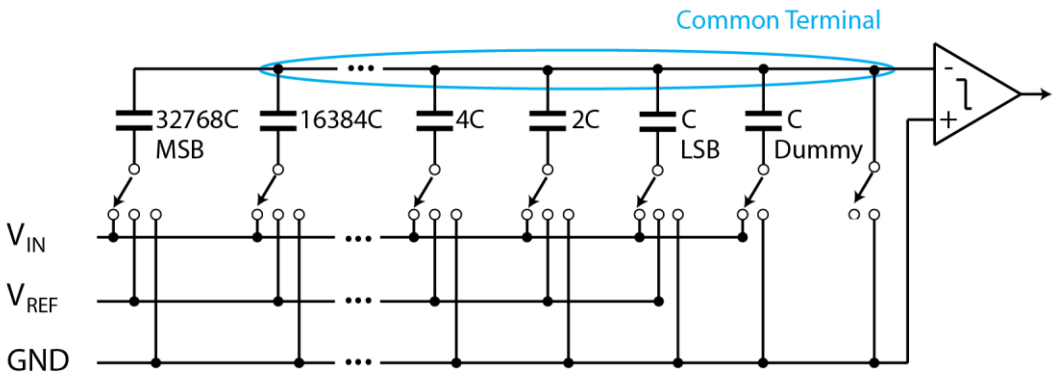

Figure 3 - 7: An example of a 16 bit capacitive DAC
Image based on [18], p. 3.

For a N-bit ADC there is an array of N binary weighted switched capacitors plus one dummy capacitor. The leftmost capacitor corresponding to the MSB has the highest capacity. Each consecutive capacitor has half the capacity of his left-handed neighbor. This example illustrates a 16 bit DAC. The conversion starts with the signal acquisition. At the beginning the common node of the capacitors is connected to ground, while the other terminals are connected to the analog input voltage V_{IN}. After acquisition each capacitor holds a charge proportional to the input voltage according to $Q = C * V_{IN}$. By switching the terminals from the input voltage source to ground, the capacitors cause a voltage of $– V_{IN}$ at the negative comparator input. Next the binary search is performed. The MSB capacitor is connected to the reference voltage source, while the rest of the capacitors stay at ground. Due to the binary-weighting the MSB capacitor causes a voltage of $V_{REF} / 2$ at the comparator input. Thus the resulting input is $– V_{IN} + V_{REF} / 2$. If this sum is smaller zero or equivalently if $V_{IN} > V_{REF} /2$, the comparator outputs a logic 1 and the MSB capacitor stays connected to the reference voltage source. Otherwise the comparator outputs a logic 0 and the MSB capacitor is connected to ground again. This step is repeated for each consecutive capacitor. At the end the input voltage at the comparator is almost zero.

The input voltage after conversion corresponds to

$$-V_{IN} + B_{N-1} * \frac{V_{REF}}{2} + B_{N-2} * \frac{V_{REF}}{4} + B_{N-3} * \frac{V_{REF}}{8} + \ldots + B_0 * \frac{V_{REF}}{2^N},$$

where $B_0,\ldots, B_{N-1}$ are the comparator output bits and form the result of the SAR ADC.

Next the parameters of the SAR ADC as part of the proposed angle measurement system are figured out. Based on the maximum input signal frequency and the desired sample rate the internal circuitry frequency is determined. The input signal is a sine wave with a maximum frequency of 5 kHz. Assuming a sample rate of 244 kHz, there are 48 samples per signal period. In case of a 16 bit ADC the binary search algorithm requires 16 cycles + 2 clock cycles for data processing (loading registers, etc). Thus an internal clock frequency of 244 kHz * 18 cycles = 4.392 MHz is required. The reference voltage of the SAR ADC is +/- 85 mV, which is selected according the maximum anticipated GMR sensor bridge output voltage of 81.6 mV. The parameters are summarized in Table 3 - 2.

Parameter	Value	Unit	Comment
N	16	Bit	Resolution
F	4.392	MHz	Internal clock frequency
V_{REF}	+/- 85	mV	Reference voltage
f_{OUT}	244	kHz	Sample rate

Table 3 - 2: Parameters of the SAR ADC

Summarized the benefits of the SAR ADC are its low power consumption and the small form factor. The central limitation is that the comparator and the DAC must be as accurate as the overall system, as the accuracy directly affects the conversion result.

3.4.2 Delta-Sigma-ADC

This section introduces the Delta-Sigma ADC. The information was taken from [15], [16] and [17]. The basic working principle of Delta-Sigma-ADCs is to estimate the input signal, measure the error, integrate this error and then compensate it. Figure 3 - 8 illustrates the simplest form of a Delta-Sigma ADC.

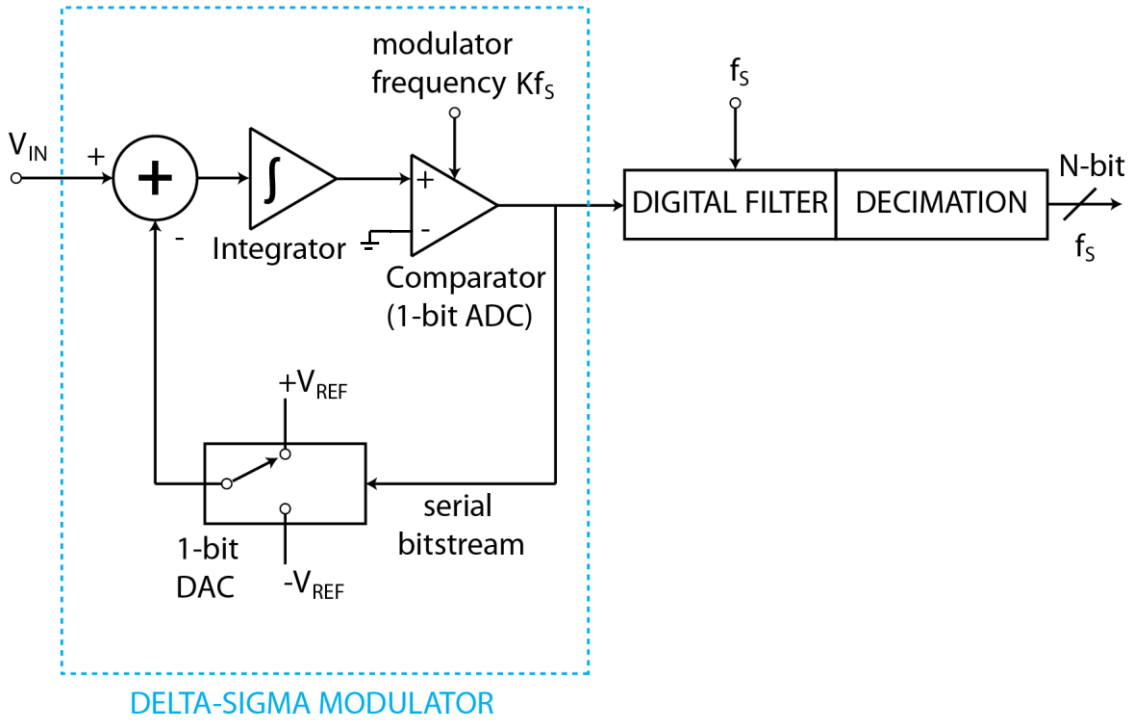

Figure 3 - 8: Block diagram of a first order Delta-Sigma ADC.
Image based on [16], p. 6.

It consists of two major building blocks: An analog first order Delta-Sigma modulator and a digital low-pass filter. The modulator is build up by an integrator and a comparator. The output signal of the comparator can be interpreted as a bit stream. It is coupled to a feedback loop containing a 1-bit digital-to-analog converter (DAC). The output signal of the DAC is subtracted from the input signal. The error is integrated and the comparator outputs a “one” if a certain threshold is exceeded. Depending on the comparator output the DAC can adopt two states, which are $-V_{REF}$ and $+V_{REF}$. These voltages also define the signal input range of the Delta-Sigma-ADC.

The comparator output is a bit stream with much higher data rate than the overall system data rate. The mean value of this bit stream corresponds to the mean value of the

input signal of the Delta-Sigma-ADC. As the input signal increases towards $+V_{REF}$, the number of "ones" in the bit stream increases. Conversely, as the signal goes towards $-V_{REF}$, the number of "ones" in the bit stream decreases. The bit stream data rate has to be much higher than twice the maximum input signal frequency (Nyquist-Shannon sampling theorem), in order to get a higher amount of bit stream pulses, from which the mean value can be calculated. The more bits are considered, the more accurate the mean value of the input signal can be approximated. The subsequent decimation filter converts the bit stream to a higher resolution code with lower data rate.

Next the theoretical background leading to the described structure of the Delta Sigma ADC will be discussed in detail.

By converting an analog signal into the digital domain assuming an ideal converter the maximum quantization error is +- ½ LSB. The root mean square (RMS) quantization noise is $\frac{q}{\sqrt{12}}$, where q is the voltage of a LSB. As illustrated in Figure 3 - 9A the noise is distributed uniformly within the Nyquist band from DC to $f_s/2$.

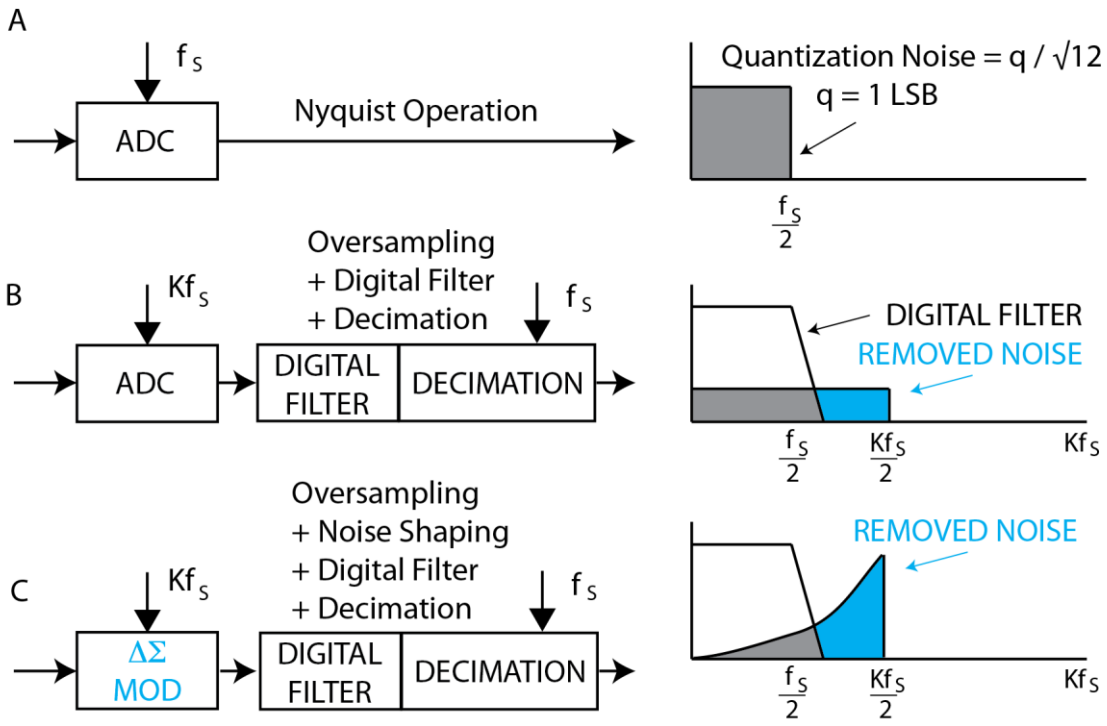

Figure 3 - 9: Effects of oversampling, digital filtering, noise shaping, and decimation. Image based on [16], p. 5.

According the Nyquist theorem the sampling frequency f_s has to be at least twice the maximum input frequency to reconstruct the input waveform. By increasing the sampling frequency by a factor K, the RMS noise remains $\frac{q}{\sqrt{12}}$, but it spectrally flattens out to a wider band ranging from DC up to $K*f_s/2$. K is denoted as the oversampling factor. The situation is depicted in Figure 3 - 9B. Applying a digital low pass filter to the output, removes a lot of quantization noise while keeping the signal information. Therefore the SNR increases by simply raising the sampling frequency. The output rate can be lower than this sampling rate by passing every M^{th} result and discarding the remainder. This process is called decimation by a factor of M. Basically M can adopt any integer value, as long as the output frequency is twice the maximum input frequency in order to fulfill the Nyquist sampling theorem.

Using the oversampling technique a factor of $K = 2^{2N}$ has to be applied to obtain an additional bit in resolution. Thus oversampling is limited by a maximum sampling frequency. This is where noise shaping comes in. The Delta-sigma modulator leads to a noise distribution as depicted in Figure in Figure 3 - 9C. The integrator acts as a high pass filter to the quantization noise and pushes it to higher frequencies. Thus applying a filter to the Delta-Sigma output removes more noise than simply oversampling does. Higher order Delta Sigma modulators lead to an even higher signal-to-noise ratio (SNR). Additionally the oversampling ratio can be smaller to achieve the same SNR compared to lower order modulators. The first order modulator provides a 9dB improvement in SNR for every doubling of the sampling rate. The second order modulator leads to a 15dB improvement.

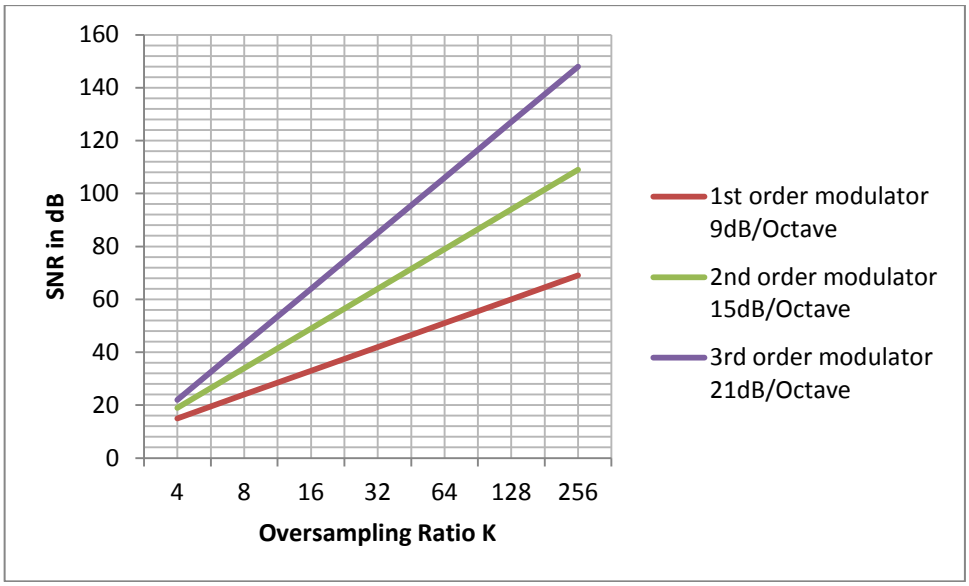

Figure 3 - 10: Signal-to-noise ratio vs oversampling ratio
Relationship between order of delta-sigma modulator and the required over-sampling ratio to achieve a particular SNR. Image based on [17], p. 4.

Summarized the benefits of the Delta-Sigma ADC are its high resolution without the need for high precision analog building blocks. It offers inherent linearity, due to the single bit DAC in the feedback loop, which outputs only two states. Because of the high oversampling ratio there is also no need for anti-aliasing filters at the input. Finally a sample and hold block is dispensable. The main limitations are the limited input signal frequency, the high internal modulator frequency and the challenging digital filter design.

The parameters of the Delta-Sigma ADC as part of the proposed angle measurement system will be figured out in Chapter 3.5. In the next section the digital filter is described, which is necessary to convert the modulator bitstream into a code word.

3.4.3 Cascaded Integrator Comb Filtering

As already mentioned the output of the Delta-Sigma modulator is a bit stream with high data rate. The stream has to be converted into a signal with higher bit width but lower data rate. This is achieved in the subsequent digital filter using frequency decimation. Basically frequency decimation consists of two steps:

1. Low-pass filtering to remove aliasing in the desired passband and
2. Decimation by a factor of R, which means discarding R-1 samples

An economic way of decimation is cascaded integrator comb (CIC) filtering which was originally proposed by Eugene Hogenauer [19]. This section summarizes the findings of Hogenauer. Additionally the derivation of the transfer function is shown in detail. Further information was taken from [20] and [21].

Figure 3 - 11 illustrates the structure of a CIC decimation filter. As the name already states the filter consists of N integrators running at the high sampling frequency and N comb filters (differentiators) running at low frequency. These two sections are separated by a downsampling block which reduces the integrator's frequency by a factor R.

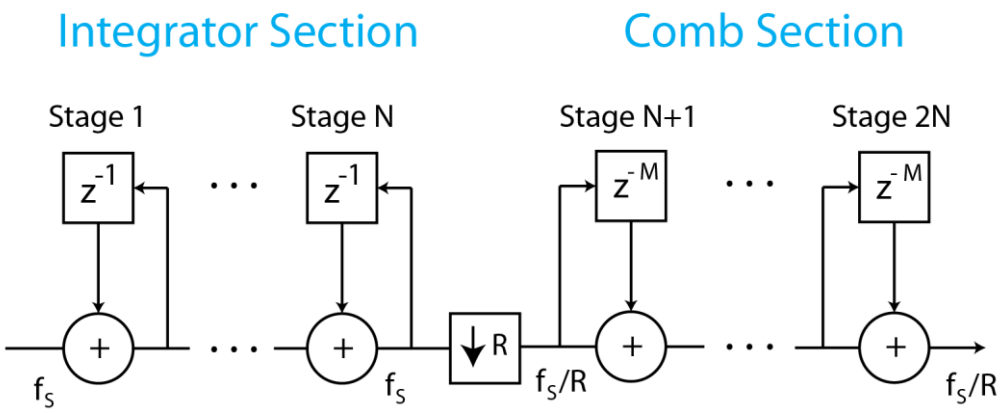

Figure 3 - 11: Basic structure of CIC decimation filter.
It consists of N integrator stages running at high sampling frequeny and N comb stages running at reduced frequency by factor R. Image based on [19], p. 2.

The transfer function of a single integrator stage can be derived from the block diagram depicted in Figure 3 - 12.

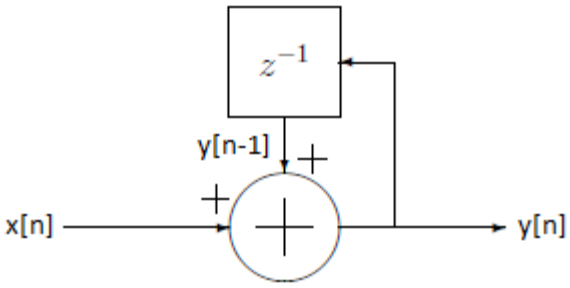

Figure 3 - 12: Block diagram of single integrator

$$y[n] = y[n-1] + x[n]$$

$$Y(z) = Y(z) * z^{-1} + X(z)$$

$$H_I(z) = \frac{Y(z)}{X(z)} = \frac{1}{(1 - z^{-1})}$$

There is a single pole at z = 1, leading to an infinite impulse response which makes the integrator stage as a stand-alone system instable. The frequency response has low pass characteristic and decreases with -20dB per decade.

The magnitude frequency response can be determined by evaluating $H_I(z)$ at $z = e^{j(2\pi f/R)}$. For simplicity $2\pi f/R$ is substituted by ω

$$H_I(e^{j\omega}) = \frac{1}{(1 - e^{-j\omega})}$$

Using Euler's identity this equation can be rewritten as

$$H_I(e^{j\omega}) = \frac{1}{1 - cos\omega + j \sin\omega} = \frac{1}{2} - j \frac{\sin\omega}{2\,(1 - \cos\omega)}$$

The magnitude of a complex number is given by $|z| = \sqrt{Re^2 + Im^2}$

$$\left|H_I\left(e^{j\omega}\right)\right| = \sqrt{\frac{1}{4} + \frac{\sin^2\omega}{4\,(1-\cos\omega)^2}} = \sqrt{\frac{1-2\,cos\omega+\cos^2\omega+\sin^2\omega}{4\,(1-\cos\omega)^2}}$$

Using the identity $\cos^2\omega + \sin^2\omega = 1$ the equation can be rearranged to

$$\left|H_I\left(e^{j\omega}\right)\right| = \sqrt{\frac{1}{2\,(1-\cos\omega)}}$$

Resubstituting $2\pi f/R$ for ω finally gives the magnitude frequency response of the integrator stage.

$$|H_I(f)| = \sqrt{\frac{1}{2\left(1-\cos\frac{2\pi f}{R}\right)}}$$

In a similar way the transfer function of one comb stage relative to the high sampling frequency can be derived from Figure 3 - 13.

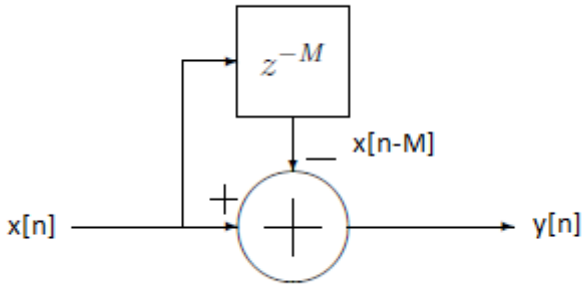

Figure 3 - 13: Block diagram of single comb filter

$$y[n] = x[n] - x[n - RM]$$

$$Y(z) = X(z) - X(z) * z^{-RM}$$

$$H_C(z) = \frac{Y(z)}{X(z)} = (1 - z^{-RM})$$

M is denoted as the differential delay and is typically set to 1 or 2. R is the rate change factor. The frequency at the filter output is fs/R. Thus the zero at z = 1 cancels out the pole at z = 1 leading to a stable overall system.

Again the magnitude frequency response is derived:

$$H_C(e^{j\omega}) = (1 - e^{-j\omega RM}) = 1 - \cos \omega RM + j \sin \omega RM$$

$$|H_C(f)| = \sqrt{2(1 - \cos 2\pi fM)}$$

Due to linearity the overall system function is given by

$$H(z) = {H_I}^N(z) * Hc^N(z) = \frac{(1 - z^{-RM})^N}{(1 - z^{-1})^N}$$

The magnitude frequency response can be determined by multiplying the frequency responses of the single stages.

$$|H(f)| = |H_I(f)| * |H_C(f)| = \sqrt{\frac{2\,(1 - \cos 2\pi fM)}{2\left(1 - \cos \frac{2\pi f}{R}\right)}}$$

$$|H(f)|^2 = \frac{1 - \cos 2\pi f M}{1 - \cos \frac{2\pi f}{R}}$$

Using the identity $\cos 2x = 1 - 2\sin^2 x$ the equation can be rearranged to

$$|H(f)|^2 = \frac{\sin^2 \pi f M}{\sin^2 \frac{\pi f}{R}}$$

Thus the magnitude frequency response of the overall system including N integrator and N comb stages is given by

$$|H(f)| = \left(\frac{\sin \pi f M}{\sin \frac{\pi f}{R}} \right)^N$$

Here the frequency is relative to the low output sampling frequency. For large rate change factors R and a limited frequency range of $0 \leq f \leq \frac{1}{M}$ the function can be approximated by

$$|H(f)| = \left(RM \frac{\sin \pi f M}{\pi f M} \right)^N$$

Figure 3 - 14 illustrates the magnitude frequency response of an N = 3 stage CIC filter with a differential delay parameter M = 1 and a rate change factor R = 128.

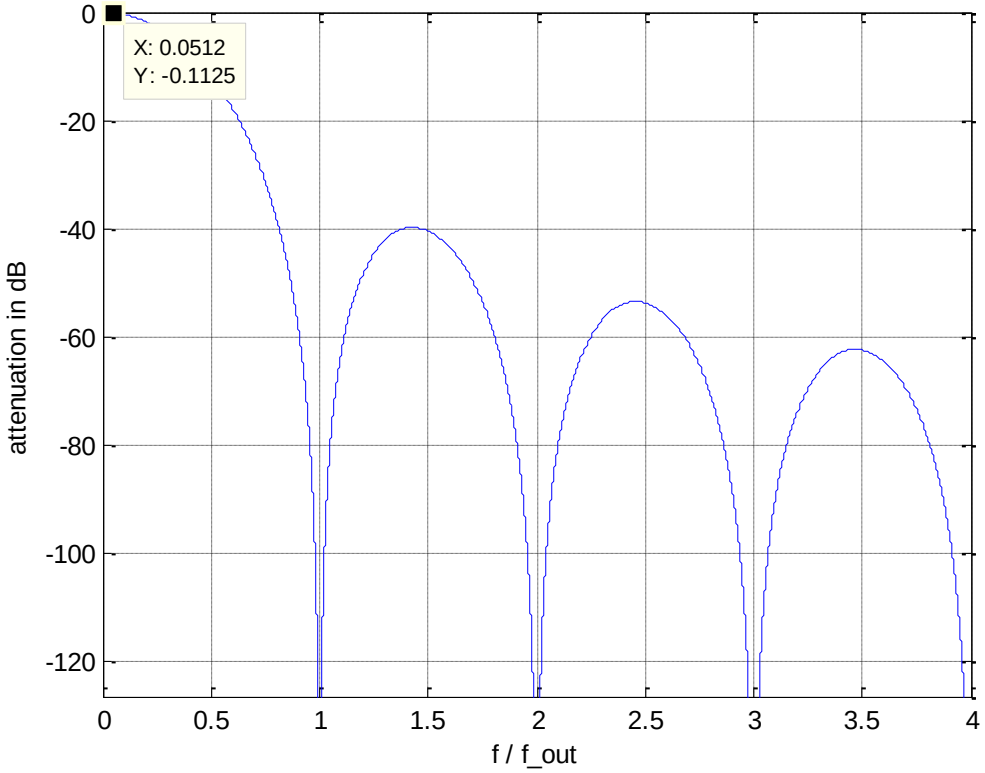

Figure 3 - 14: Magnitude frequency response of a CIC decimation filter

R, M, and N are the only parameters to control the transfer characteristic. M controls the placement of zeros. Zeros occur at integer multiples of f = 1/M. N controls the magnitude attenuation which is N * 20dB per decade.

There occur aliasing bands around every M^{th} zero ranging from 1/M $-f_c$ to 1/M + f_c, which causes aliasing errors in the desired passband. The aliasing attenuation is defined at frequency 1-f_c. The gain at DC of the filter is given by

$$G = (RM)^N$$

which leads to a minimum required bit register length due to bit growth.

$$B_{out} = \lceil N * log_2 RM + B_{in} \rceil$$

B_{in}… number of input bits.

As shown in Figure 3 - 14 at a maximum input frequency of 5 kHz the signal is attenuated by 0.1125 dB. However this attenuation doesn't affect the angle calculation as both GMR bridge signals are attenuated equally. Consequently over one shaft revolution the circular shaped envelope described by the field magnitude vector will get a smaller diameter, but the angle stays the same.

The major benefit of CIC decimation filters is the reduced hardware effort. No multipliers are required and there is no need for additional storage for filter coefficients. A disadvantage is the limited range of filter characteristics as the frequency response is fully determined by only three integer parameters (R, M and N).

3.5 Simulink model

In this section the MATLAB Simulink model of the out of axis angle measurement system proposed in Chapter 2.5 and Chapter 2.6 is presented. The ADC's digital filter structure has been adopted from Infineon's TLE 5012B Simulink model. The filter parameters have been adapted to match the input signal requirements of the new angle measurement system. The rest of the model has been developed within this thesis. There is a central script named init.m in which all parameters of the model can be adjusted and initialized.

Figure 3 - 15 shows an overview of the out of axis angle measurement system. It consists of 4 major building blocks:

- A stimulus block which represents the rotating shaft.
- A sensor block consisting of two Wheatstone bridges and a look-up table which holds the magnetic field components.
- An ADC block that converts the analog sensor output into the digital domain.
- An algorithm block calculates the absolute shaft angle from the sensor signals.

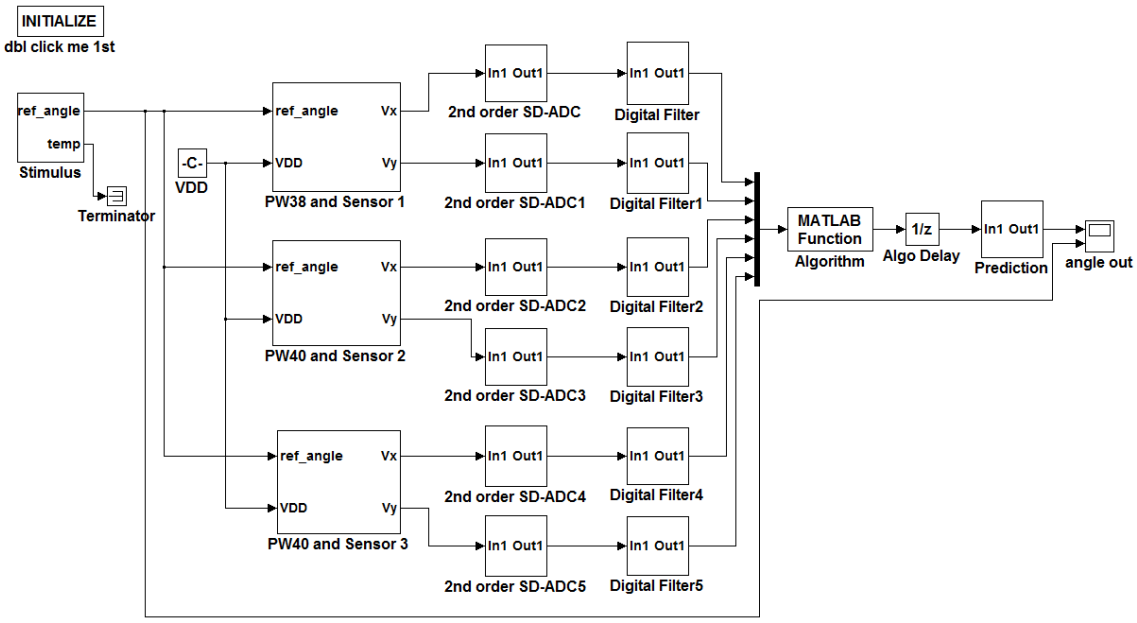

Figure 3 - 15: Simulink model of the out of axis angle measurement system

Stimulus Generation

The stimulus block depicted in Figure 3 - 16 represents the rotating shaft. The output is a mechanical reference angle derived from the motor speed. The system is designed for a maximum motor speed of 15.000 rotations per minute (rpm). The angle is calculated from a sine and cosine block using the atan2 function. The frequency of these signals is derived from the motor speed.

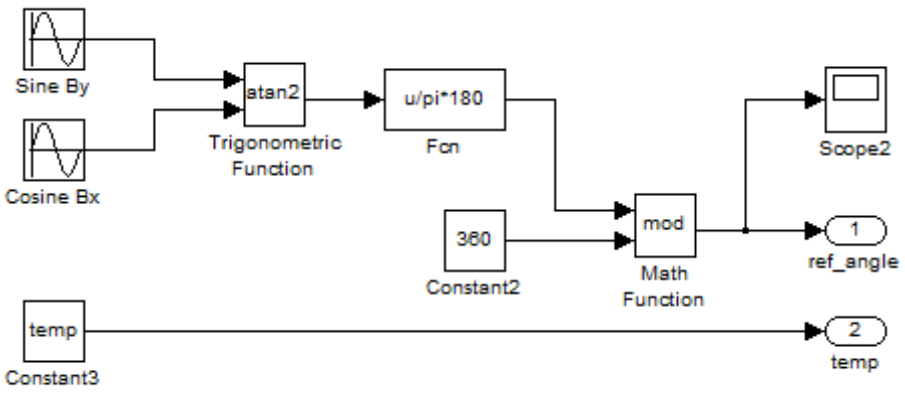

Figure 3 - 16: Stimulus generation block

Magnetic response and GMR sensitive area

The B-field components calculated in the FEM simulations are stored in a LUT as shown in Figure 3 - 17. The reference angle of the stimulus generation block serves as index for this LUT. Depending on the reference angle a new angle is calculated from the stored B-field components.

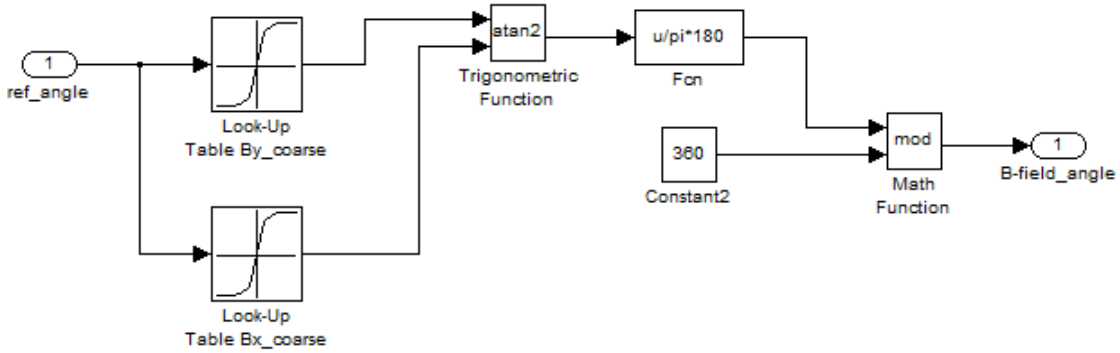

Figure 3 - 17: Calculation of new angle from the B-field components stored in the LUT

This new angle serves as input for the model of the sensitive area. The sensitive area consists of two Wheatstone bridges oriented at 90° to each other. Figure 3 - 18 illustrates the model of the Wheatstone bridges.

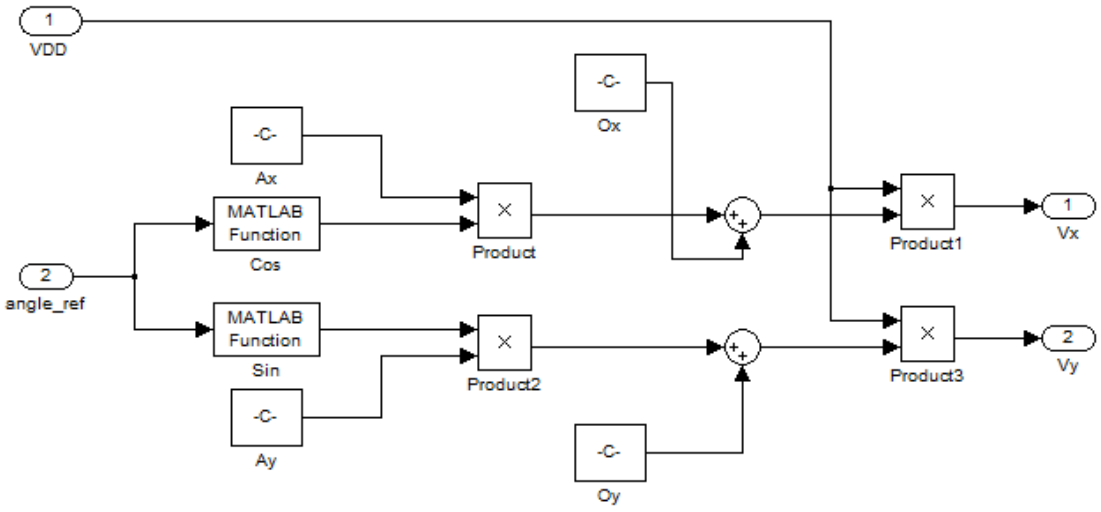

Figure 3 - 18: Simulink model of the Wheatstone bridges

The upper path in this model represents the Wheatstone bridge measuring the x component (cosine) of the magnetic field. The lower path represents the Wheatstone bridge measuring the y component (sine). Naturally the output voltages depend on the bridge supply voltage. The maximum output signal strongly varies over temperature and magnetic field drifts.

As already shown in Chapter 3.2 the peak amplitude is 81.6mV. The minimum amplitude is 15.4 mV. The frequency of the signal depends on the motor speed and on the structure of the pole wheel. In case of the pole wheel setup used in this system the maximum frequency is 5 kHz at a motor speed of 15000 rpm.

Delta-Sigma ADC

The ADC is modeled as a second order Delta-Sigma modulator. This is a good compromise between achievable resolution and required silicon area. In addition higher order modulators are considered potentially unstable owing to the accumulation of high input signal values in the integrators [16].

The Simulink model is depicted in Figure 3 - 19. The input signal is sampled at very high frequency of 125 MHz. The Delta-Sigma modulator shapes the noise and pushes it to higher frequencies. The reference voltage of the ADC is selected according the overload property of the Delta-Sigma modulator:

It is necessary to leave some headroom to avoid overload of the modulator. By increasing the input voltage also the SNR increases linearly until its peak SNR is reached. Beyond the peak SNR the SNR drastically decreases due to instability of the modulator. If the input amplitude applied to the converter is larger than a certain value, the feedback loop of the modulator gets unstable and the noise shaping disappears. This overload level is 3 dB below the peak SNR. Therefore to be on the safe side, some headroom is left and the reference voltage of the Delta-Sigma converter is set to +/- 120 mV. The maximum output of the sensor bridges is +/- 81.6 mV, which is roughly 70% of the full scale reference voltage of the ADC [15].

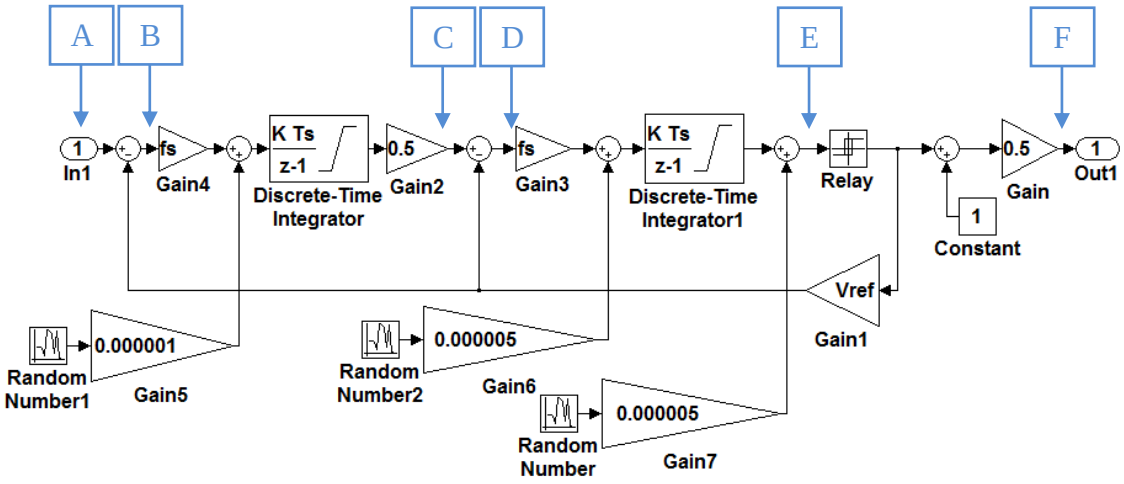

Figure 3 - 19: Simulink model of the 2nd order Delta-Sigma modulator

The integrators are modeled as discrete time integrators with sampling time $1/f_s$ and gain factor f_s. The supply voltage is assumed to be +/-1.25 V. Hence the saturation voltage is set to +/- 1.2 V. The block 'Gain2' in Figure 3 - 19 represents a loop coefficient. According to [15] loop coefficients are necessary to stabilize the Delta-Sigma modulator. The higher the coefficients are, the better the noise shaping ability is, but with higher risk of instability. Figure 3 - 20 illustrates a signal flow chart for a DC input signal with 85 mV. The plots show the signals at the indicated positions in Figure 3 - 19. It is quite difficult to analyze the behavior of the second order modulator in the time domain. Figure 3 - 20A shows the DC input signal with 85 mV, which is near to the positive full scale of 120 mV. Therefore as shown in Figure 3 - 20F there are more 'ones' than 'zeros' in the bitstream at the comparator output. Assuming a 0 V input signal the number of 'zeros' and 'ones' would be equal.

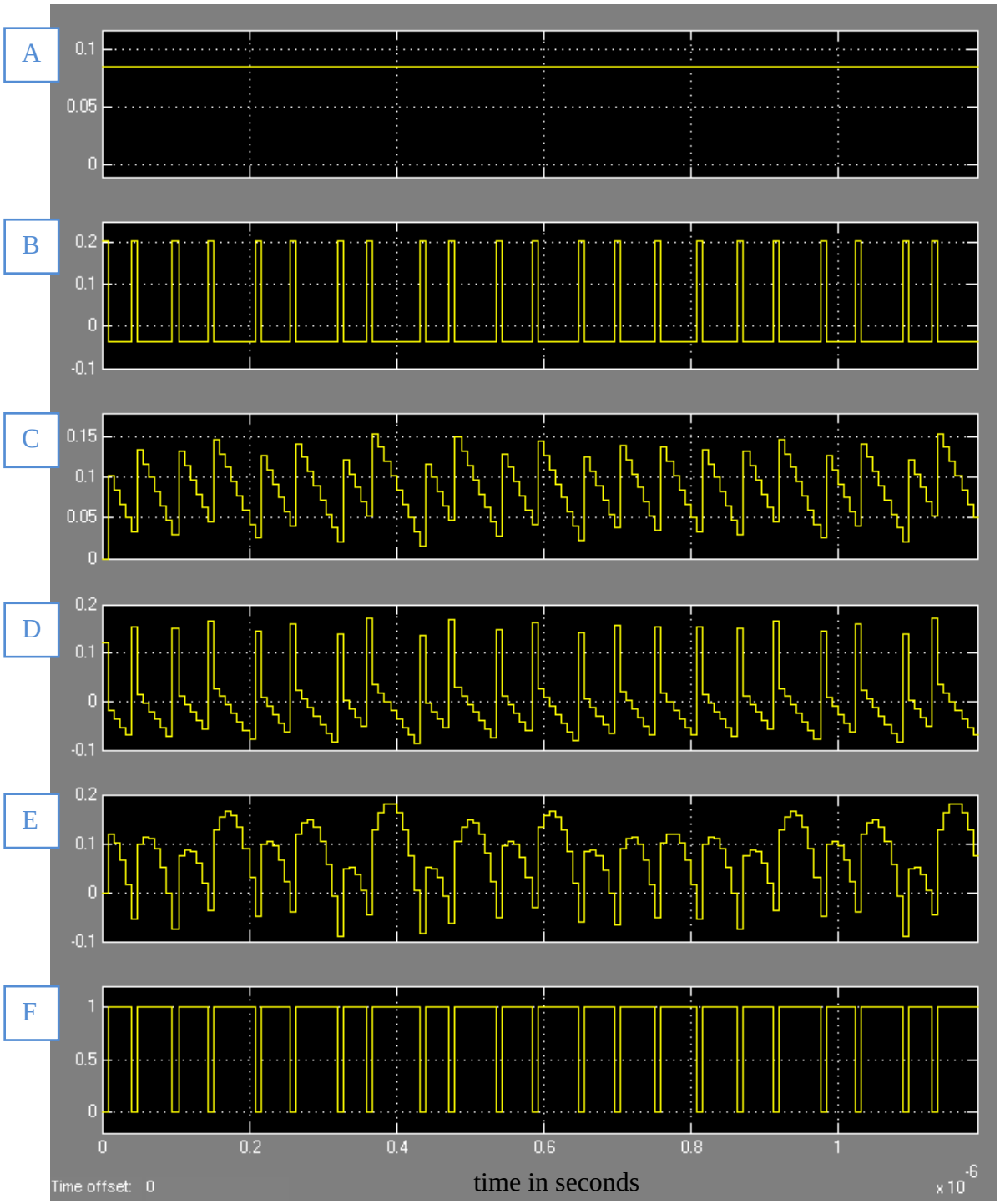

Figure 3 - 20: Signal flow chart for a DC input signal with 85 mV
The plots show the signals at the indicated positions in Figure 3 - 19. For increasing input amplitudes the number of ones in the output bitstream decreases.

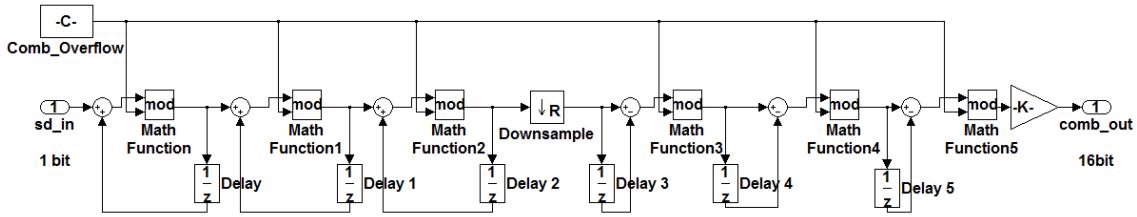

Figure 3 - 21: Simulink model of the 3rd order CIC decimation filter

The comparator output of the Delta-Sigma modulator is directly fed into the CIC decimation filter, which is shown in Figure 3 - 21. Here the serial bitstream is converted to a 16 bit code word by reducing the sample rate. The integrators of the CIC decimation filter are running at the same frequency as the Delta-Sigma modulator. The downsample block reduces the sampling frequency by a factor R = 128. Thus the frequency at the output of the comb section is 977 kHz. The differential delay M is set to 1. The maximum register length is modeled according the bit growth formula of the previous chapter. In this case the number of bits is 22. Register overflow is modeled using modulo blocks. The frequency of the CIC filter is additionally decreased in the moving average filter by a factor of 4. Therefore the output data rate of the Delta-Sigma converter is 244 kHz. The parameters of the Delta-Sigma ADC are summarized in Table 3 - 3.

Parameter	Value	Unit	Comment
f_S	125	MHz	Delta Sigma modulator frequency
V_{REF}	+/- 120	mV	Reference voltage
V_{SAT}	+/- 1.2	V	Integrator saturation voltage
R_{CIC}	128	-	CIC decimation factor
R_{MA}	4	-	Moving average decimation factor
f_{OUT}	244	kHz	ADC output frequency

Table 3 - 3: Parameters of the Delta Sigma ADC

3.6 Performance metrics for the Delta-Sigma ADC

In this section typical performance metrics which characterize the Delta-Sigma ADC are presented. The definitions were taken from [15] , [22] and [23]. The performance metrics of the second order Delta-Sigma ADC used in the Simulink model are determined using the MATLAB script from [24] and a test setup as outlined in [22].

- The signal-to-noise ratio (SNR) is defined as the ratio of the input signal power (RMS value) to the noise power of the converter (RMS value), excluding the DC and harmonic components. The maximum achievable SNR of a converter is called peak signal to noise ratio. The noise includes the quantization noise and circuit noise. For an input sine signal having an amplitude of 109 mV and a frequency of 5 kHz the peak SNR of 96.1453 dB is reached. Figure 3 - 22 illustrates the SNR for different input amplitudes.

- The signal-to-noise and distortion ratio (SINAD) is defined in a similar way. It is the same as SNR except that the SINAD also includes the harmonic components in the noise power calculations. At low input amplitudes the distortion components go down in the noise floor of the converter. Therefore the SINAD is equal to the SNR. At high input amplitudes the harmonic components get more dominant leading to a deteriorated SINAD compared to the SNR. From the SINAD the ENOB can be calculated. Using the same input sine signal as for the SNR calculation the SINAD is 96.1276 dB.

- The overload level (OL) refers to the input signal amplitude where the SNR decreases by 3 dB below the peak SNR. For higher input amplitudes than the OL the Delta-Sigma modulator gets unstable and the noise shaping disappears. This results in a drastic SNR degradation. The OL of the ADC in the Simulink model is reached at about 117 mV. Here the SNR is 92.7834 dB which is approximately 3 dB below the peak SNR

- The dynamic range (DR) is the ratio between the maximum input signal power which can be applied to the ADC without significant degradation of the SNR (SNRp – 3dB) and the minimum detectable input signal power (SNR = 0dB). The DR represents the range of input signal amplitudes which a converter can resolve. The DR of the ADC of the Simulink model is given by

$$DR = 20 * \log\left(\frac{OL}{V_{LSB}}\right) = 20 * \log\left(\frac{117\ mV}{3.36\ \mu V}\right) = 90.84\ dB$$

- The effective number of bits (ENOB) can be calculated from the SINAD using the following formula [25].

$$ENOB = \frac{SINAD - 1.76}{6.02}$$

The ENOB decreases with increasing input frequencies, as the increasing distortion components deteriorate the SINAD. For the ADC of the Simulink model with a SINAD of 93.9964 dB at an input amplitude of 81.6mV the ENOB is 15.32.

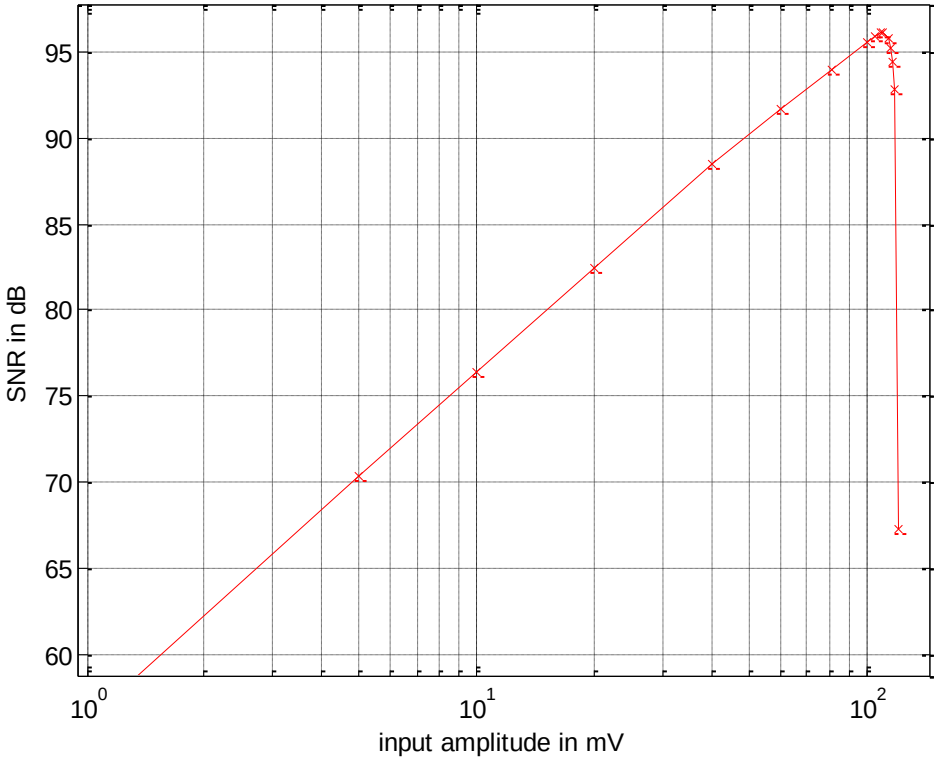

Figure 3 - 22: SNR over different input amplitudes
The peak SNR is 96.1453 reached at an amplitude of 109 mV. At 117 mV the SNR has dropped by 3 dB (Overload Level).

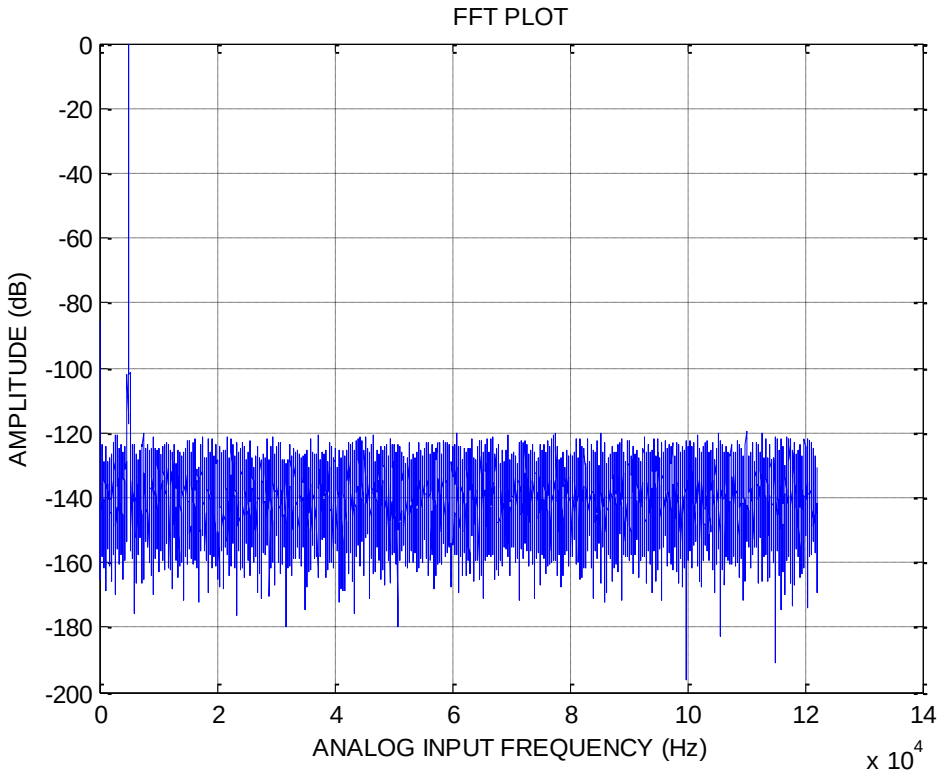

Figure 3 - 23: FFT output of 2nd order Delta-Sigma ADC

3.7 Digital Representation

In this chapter the results of the analog-to-digital conversion as well as a runtime estimation for the angle calculation are presented.

The upper plot of Figure 3 - 24 shows the maximum and minimum possible output signals of the Wheatstone bridges. The lower plot shows the corresponding results of the analog to digital conversion. As visible there is also an offset voltage superimposed to the signals.

Here the simulation time is set to 1ms. The motor speed is 15000 rpm. The blue signal is the voltage representing the x component of the magnetic field caused by the coarse pole wheel at an ambient temperature of -40°C. The red signal is the voltage representing the y component at an ambient temperature of +150°C. As visible the amplitude drastically depends on the ambient temperature. It increases with falling temperatures. In the lower plot the digitized versions are depicted. The results are summarized in Table 3 - 1.

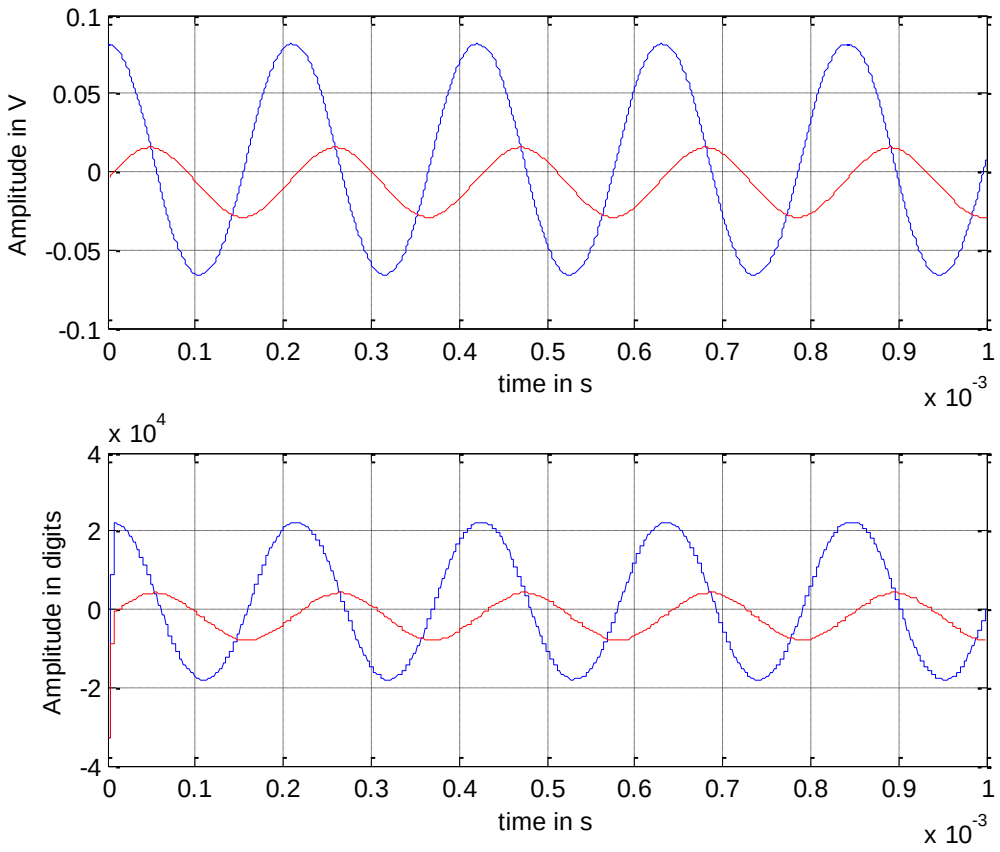

Figure 3 - 24: Maximum and minimum occuring output amplitudes

Parameter	Value	Unit	Comment
V_{MAX} Amplitude	22275	Digits	@ -40°C
V_{MIN} Amplitude	4208	Digits	@ 150°C

Table 3 - 4: Maximum and minimum amplitudes after analog-to-digital conversion

To analyze the error introduced by the sensors and the analog-to-digital conversion a comparison between the angle calculations using the digitized and the analog signals is shown. This time the simulation time was set to 4 ms. At an engine speed of 15000rpm this corresponds to one revolution of the motor shaft. The ‘analog’ angle is calculated from the raw B-field components, while the ‘digital’ angle is calculated from the output of the Delta-Sigma ADCs. The upper plot in Figure 3 - 25 shows the resulting angles over one revolution of the shaft. There is a constant offset superimposed to the angle calculated from the digitized signal amplitudes, which is related to the delay time of the analog-to-digital conversion. By subtracting this offset the error introduced by the sensors and the conversion becomes visible. The maximum error is about +/- 0.0216°. This error is denoted as the angle noise. The peak-to peak angle noise is 0.0432, which is within the desired bounds of 0.05°.

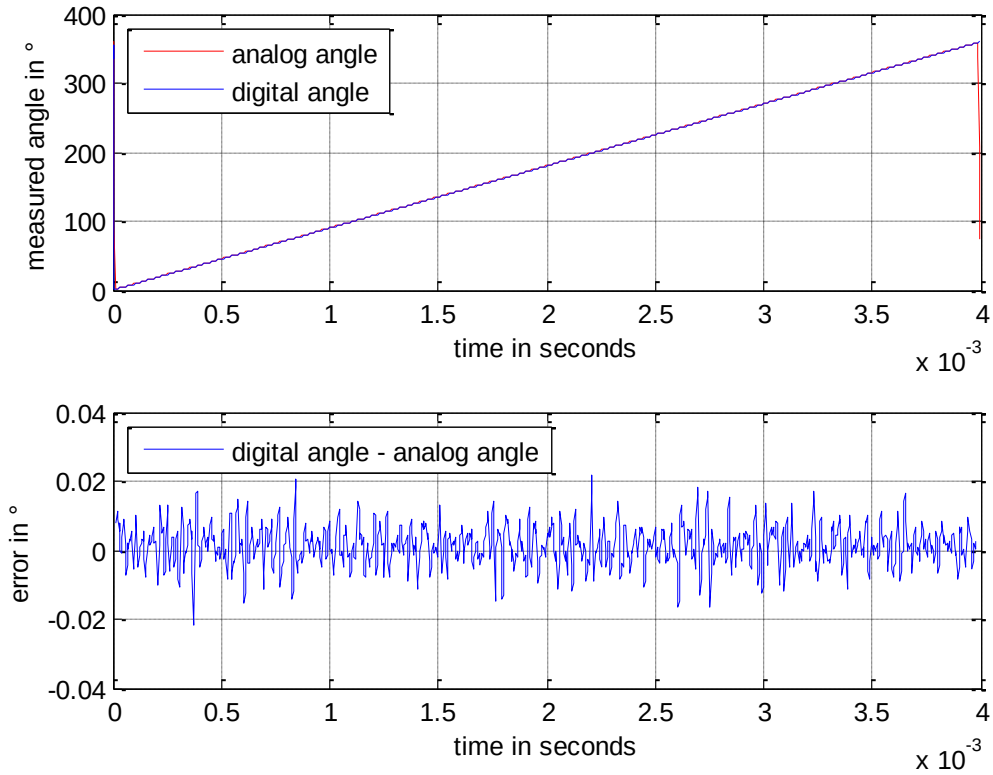

Figure 3 - 25: The maximum error of the analog-to-digital conversion is +/- 0.0216°

Runtime Estimation

The runtime of the angle calculation algorithm additionally delays the results, which leads to an additional angle error. To estimate the runtime the occurring instructions are counted and listed in Table 3 - 5. For each operation the required number of clock cycles in order to execute the instruction is estimated:

- Additions can be implemented for instance as a ripple-carry-adder, which consists of N-1 full adders and one half adder. Here N is the number of bits of the operands. Ripple-carry-adders offer a simple design and fast implementation. The disadvantage is that in worst case the carry bit has to propagate through all gates, and therefore the result is available only after N times the propagation delay through one adder. Nevertheless ripple-carry-adders can be implemented in a way delivering a new summation result within one clock cycle. In a similar way subtractions can be realized within one clock cycle.

- A multiplication of two N bit values can be split up into N properly shifted additions. This is shown using the example from [26] where two eight bit values are multiplied:

```
   0b00100011         * 0b10001001
   --------------------------------
     00100011          <--+|||||||
+     00000000          <---+||||||
     ---------              ||||||
     001000110              ||||||
+      00000000         <----+|||||
     ----------              |||||
     0010001100              |||||
+       00000000       <-----+||||
     -----------             ||||
     00100011000             ||||
+        00100011      <------+|||
     ------------            |||
     001001010011            |||
+         00000000     <-------+||
     -------------           ||
     0010010100110           ||
+          00000000    <---------+|
     --------------             |
     00100101001100             |
+           00100011   <----------+
     ---------------
     001001010111011
```

  Indeed there is no real multiplication required. Depending on a zero or a one in the multiplier one has only to decide whether the multiplicand has to be added properly shifted to the intermediate result or not. Therefore a multiplication of two 16 bit values can be realized using 16 additions within 16 clock cycles. Divisions and modulo instructions also require 16 cycles. Moreover multiplications or divisions by a number with base 2 are simply shift operations which can be performed in one cycle.

- The trigonometric arc tangent function is implemented using a CORDIC (Coordinate Rotation Digital Computer) algorithm. Instead of performing real rotations the CORDIC algorithm performs pseudorotations by a precomputed set of angle values, which are stored in a LUT. The mathematical background won't be discussed here. The interested reader is referred to [27] for detailed informa-

tion. The algorithm is an iterative process and requires 16 clock cycles for a 16 bit resolution to converge.

Instruction Type	Instruction Count	Required Clock Cycles
Addition	9	1
Subtraction	10	1
Multiplication	8	16
Division	6	16
Modulo	4	16
CORDIC	4	16

Table 3 - 5: Total number of instructions and required clock cycles for execution

Therefore in total 371 clock cycles are required to execute the algorithm. To budget for some reserves roughly 2 * 371 clock cycles for the execution are assumed. The output data rate of the Delta-Sigma converter is 244 kHz, or in other words the ADC produces a new digital value every 4.096 µs. Within this time a new angle value has to be calculated. Therefore the minimum clock frequency is given by

$$f > \frac{742\ clock\ cycles}{4.096\ \mu s} = 182\ MHz$$

Therefore to get a new result within one cycle a clock frequency of about 200 MHz would be required. Assuming this clock frequency the runtime of the algorithm is calculated by

$$\text{Runtime} = \frac{742\ clock\ cycles}{200\ MHz} = 3.71\ \mu s$$

Due to the algorithm the angle is delayed by an additional clock cycle or 4.096 µs, which additionally affects the error. This error depends on the motor speed. For a maximum engine speed of 15000 rpm the additional error would be

$$e_{delay} = \frac{15000\ rpm}{60} * 360° * 4.096\ \mu s = 0.3686°$$

Hence the delay time of the algorithm additionally increases the angle error at higher motor speeds. At lower speeds the error is smaller.

Error including angle delay time

Figure 3 - 26 shows results of the measurement system for different ambient temperatures. In the left column the mechanical reference angle of the rotating shaft as well as the measured angle for three different temperatures is depicted. The corresponding angle errors are shown in the right column. The engine speed is set to 15000 rpm and the simulation time is 4 ms. Therefore the simulation results represent one revolution of the shaft. The Wheatstone bridges are parameterized using the values in the MATLAB script in the Appendix B. Due to the calibration of the Wheatstone signals in the angle calculation algorithm the sensor mismatch doesn't affect the angle calculation. Temperature influences are compensated as well. The resulting angle error is listed in Table 3 - 6. As visible from the table and the plots the error is constant over the whole operating range. The high error is mainly related to the delay of the analog to digital conversion and the runtime of the angle calculation algorithm.

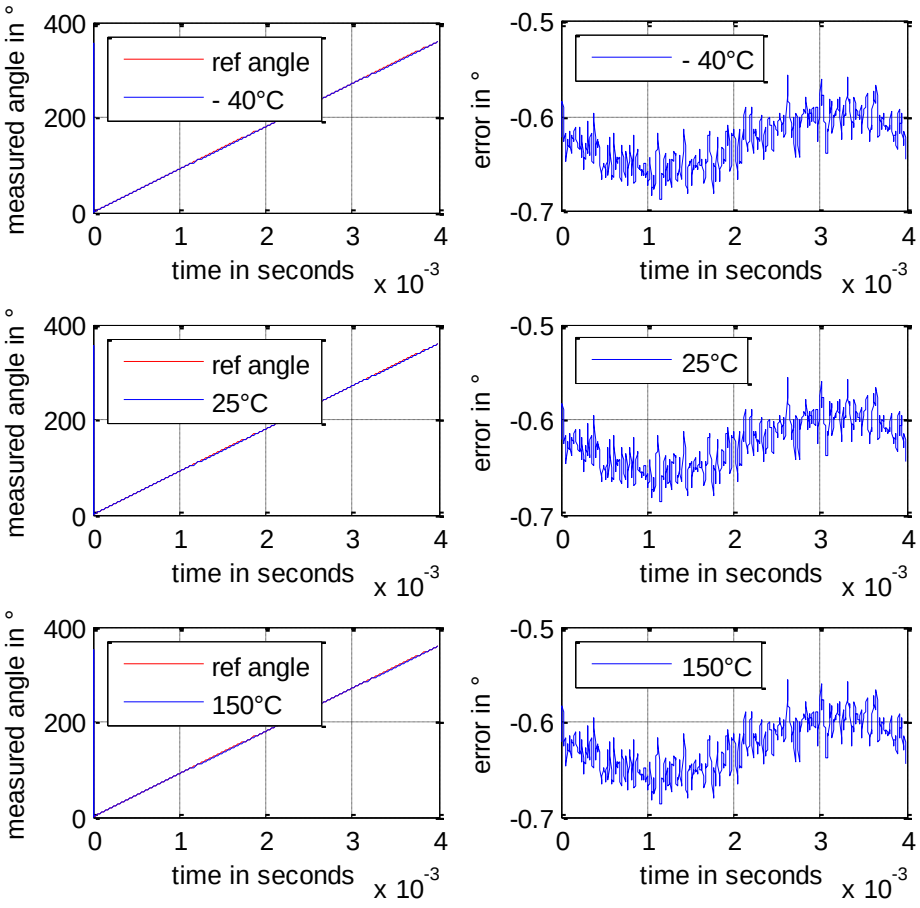

Figure 3 - 26: Measured angles and corresponding errors for three different ambient temperatures. The high error results from the delay time of the ADC and the runtime of the algorithm

Angle error		Unit	Comment
min	max		
-0.6869	-0.5567	°	@ - 40°C
-0.6864	-0.5567	°	@ 25°C
-0.6870	-05567	°	@ 150°C

Table 3 - 6: Resulting angle error over the whole operating range including angle delay time

The offset in the right column of Figure 3 - 26 is about -0.6445°. As the motor speed is constant this angular offset corresponds to the angle delay time. The angle delay time reflects the delay time of the whole signal path. It consists of the GMR bridges, the Delta-Sigma ADC including the digital filter and the angle calculation. The angle delay time is 7.161 µs. The angle calculation takes one clock cycle or 4.096 µs. Therefore the latency of the analog-to-digital conversion is about 3.064 µs.

The error due to angle delay time can be decreased by a linear prediction model of the shaft angle [10]. This model assumes a constant motor speed. The prediction is done by the following equation

$$\alpha(t+1) = 2 * \alpha(t) - \alpha(t-1)$$

Using this prediction model the angle delay time is decreased. The resulting error drops to -0.1673° / -0.324° as depicted in Figure 3 - 27.

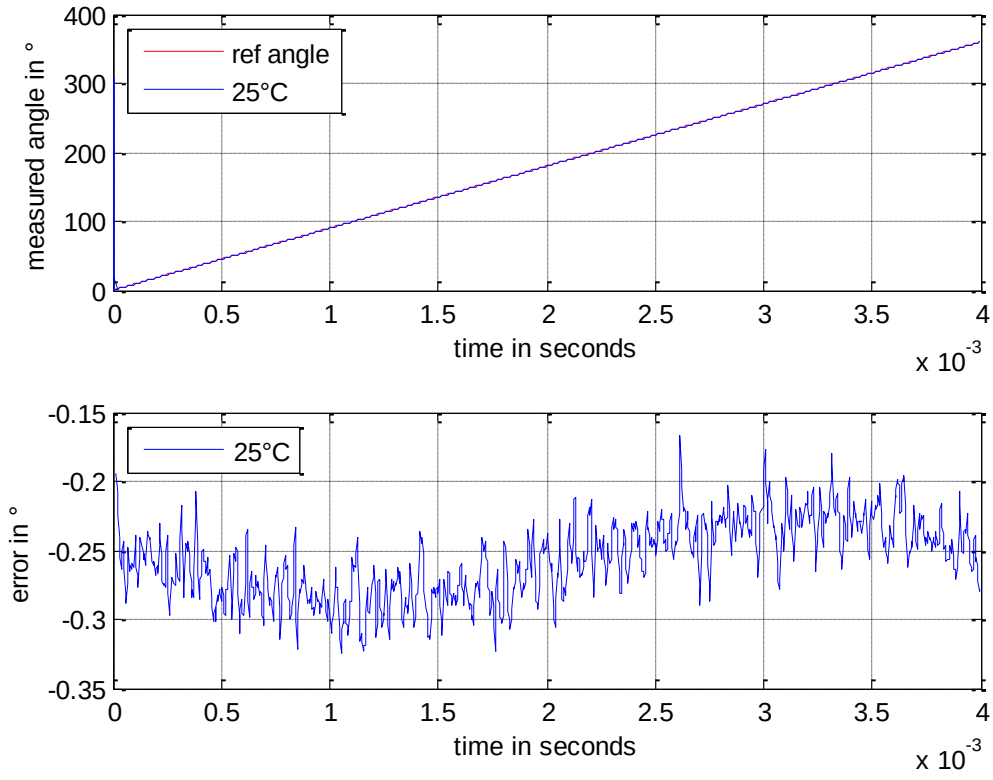

Figure 3 - 27: The linear prediction reduces the error due to the angle delay time

Parameter	Value	Unit	Comment
Update Rate	244	kHz	
Angle delay time without prediction	7.16	µs	
Angle delay time with prediction	2.98	µs	
Angle noise peak-peak	0.0388	°	3σ

Table 3 - 7: Signal processing results

The results show that the errors introduced by the sensor electronics and the signal processing are negligible compared to the errors introduced by the magnetic circuit and the mounting tolerances.

4 Conclusion and Outlook

The aim of this work was to develop a concept for a magnetic out of axis angle measurement system and to analyze the errors arising from the single building blocks.

Within this work a new algorithm based on the well-known Vernier principle leading to much higher accuracy was introduced. In combination with a new hardware measurement setup, the system delivers highly accurate results. Assuming an ideal magnetization the maximum error is about -0.07° / 0.06°. A MATLAB Simulink model of the overall out of axis angle measurement system is another contribution of this work. The signal processing path consists of the GMR bridges, Delta-Sigma modulators, digital filtering and the final angle calculation. In this model non-idealities of the sensors like offsets, phase shifts and different amplitudes of the Wheatstone signals are taken into account. Here the maximum resulting error of the measurement system is about -0.042° / 0.088°. Due to the compensation algorithm the error introduced by the sensor mismatch and the analog-to digital conversion is only +/- 0.02°. Table 4 - 1 summarizes the most important simulation results.

Parameter	Values		Unit	Comment
	min	max		
Error Vernier	-3.50	4.23	°	
Error Algorithm	-0.14	0.11	°	Calculated from raw field components, Ansys Mechanical
Error Algorithm + Two Probe Setup	-0.07	0.06	°	
Error Non-ideal magnetization	-0.16	0.14	°	
Error Algorithm + Two Probe Setup	-0.044	0.094	°	Raw field components, Ansoft Maxwell
Error Algorithm + Two Probe Setup and ADC	-0.042	0.088	°	
Error including angle delay time	-0.6864	-0.5567	°	@ 15000rpm, 25°C
Error with linear prediction	-0.324	-0.1673	°	@ 15000rpm, 25°C

Table 4 - 1: Results of the angle measurement system

The error arising from the signal processing is very small and therefore negligible compared to the other building blocks of the sensor system. The dominant contributors to the overall angle error are the magnetic circuit design and the mounting tolerances. The pole wheels have to be mounted precisely aligned on the shaft. The accurate placement of the sensors around the magnets circumference is another challenging task.

Beside these problems the proposed system is capable of measuring the absolute shaft angle with very high precision and without the need of an extensive calibration procedure. The true power on capability, which means that the angle is available right after startup, is another advantage of this system.

Appendix

Appendix A – Results of FEM simulation

The tables summarize the results of the FEM simulations. For different sensor locations the maximum and minimum electrical angle error is listed. The mechanical angle error is calculated by dividing the electrical angle error by the pole pair number. Additionally the magnetic field strength at the sensor location is listed. Typical GMR sensors require a minimum magnetic field strength of about 10 mT to operate properly. Therefore smaller magnetic fields are marked red in the tables. In all simulations the geometric dimensions of the pole wheels are constant. The inner wheel radius measures 20 mm, the outer radius is 30 mm and the height is 10 mm. As material hard ferrite with a coercivity H_C = 140 kA/m and a remanence B_R = 0.22 T is used. Each table lists the results for a defined number of poles. The sensor is placed either in "Top Read" or "Side Read" configuration. Additionally the results of the "Two Probe" configuration described in Chapter 2.6 are shown.

Ringmagnet 10 Poles Normal

R = 30 r = 20 h = 10

	Distance	E_max el.	E_min el.	E_max mech.	E_min mech.	B_max	B_min
	mm	°	°	°	°	mT	mT
Top Read	31.00	30.38	-30.39	6.08	-6.08	105.00	74.00
	32.00	26.10	-26.34	5.22	-5.27	67.00	58.00
	33.00	23.11	-22.62	4.62	-4.52	47.00	43.00
	34.00	19.85	-20.18	3.97	-4.04	37.00	31.00
	35.00	17.94	-17.98	3.59	-3.60	29.00	24.00
	36.00	15.70	-15.84	3.14	-3.17	23.00	18.00
	37.00	14.33	-14.55	2.87	-2.91	18.00	14.00
	38.00	12.76	-12.82	2.55	-2.56	14.00	11.00
	39.00	11.54	-11.66	2.31	-2.33	11.00	8.00
Two Probe	36.00	1.17	-1.32	0.23	-0.26	23.00	18.00
Side Read	6.00	9.72	-9.43	1.94	-1.89	14.00	12.00
	7.00	6.17	-6.45	1.23	-1.29	11.00	10.00
	8.00	2.97	-2.78	0.59	-0.56	8.00	8.00

Table A - 1: Simulation results for a pole wheel with 10 poles

Ringmagnet 20 Poles Normal

R = 30 r = 20 h = 10

	Distance	E_max el.	E_min el.	E_max mech.	E_min mech.	B_max	B_min
	mm	°	°	°	°	mT	mT
Top Read	31.00	17.76	-18.35	1.78	-1.84	95.00	71.00
	32.00	13.33	-13.06	1.33	-1.31	54.00	49.00
	33.00	10.33	-10.23	1.03	-1.02	36.00	31.00
	34.00	8.68	-9.59	0.87	-0.96	24.00	21.00
	35.00	8.24	-8.76	0.82	-0.88	17.00	14.00
	36.00	7.54	-7.20	0.75	-0.72	12.00	9.00
	37.00	6.38	-7.11	0.64	-0.71	8.00	7.00
Two Probe	33.00	1.23	-1.44	0.12	-0.14	36.00	31.00
Side Read	6.00	2.66	-2.65	0.27	-0.27	13.00	12.00
	7.00	6.00	-5.31	0.60	-0.53	10.00	8.00

Table A - 2: Simulation results for a pole wheel with 20 poles

Ringmagnet 30 Poles Normal

R = 30 r = 20 h = 10

	Distance	E_max el.	E_min el.	E_max mech.	E_min mech.	B_max	B_min
	mm	°	°	°	°	mT	mT
Top Read	31.00	10.74	-11.07	0.72	-0.74	87.00	65.00
	32.00	7.47	-7.55	0.50	-0.50	46.00	40.00
	33.00	5.05	-6.92	0.34	-0.46	27.00	24.00
	34.00	5.79	-4.92	0.39	-0.33	16.00	14.00
	35.00	3.71	-3.76	0.25	-0.25	10.00	9.00
	36.00	3.53	-3.59	0.24	-0.24	7.00	6.00

Table A - 3: Simulation results for a pole wheel with 30 poles

Ringmagnet 38 Poles Normal

R = 30 r = 20 h = 10

	Distance	E_max el.	E_min el.	E_max mech.	E_min mech.	B_max	B_min
	mm	°	°	°	°	mT	mT
Top Read	31.00	7.90	-7.47	0.42	-0.39	75.00	59.00
	32.00	3.42	-3.74	0.18	-0.20	35.00	33.00
	33.00	2.73	-2.41	0.14	-0.13	18.00	18.00
	34.00	5.89	-5.62	0.31	-0.30	10.00	8.00
Two Probe	32.00	0.85	-1.32	0.04	-0.07	35.00	33.00
	33.00	0.85	-1.00	0.04	-0.05	18.00	18.00

Table A - 4: Simulation results for a pole wheel with 38 poles

Ringmagnet 40 Poles Normal

R = 30 r = 20 h = 10

	Distance	E_max el.	E_min el.	E_max mech.	E_min mech.	B_max	B_min
	mm	°	°	°	°	mT	mT
Top Read	31.00	7.14	-8.20	0.36	-0.41	73.00	58.00
	32.00	3.06	-3.24	0.15	-0.16	34.00	31.00
	33.00	2.40	-2.69	0.12	-0.13	17.00	16.00
	34.00	2.59	-3.08	0.13	-0.15	10.00	9.00
Two Probe	32.00	0.77	-1.24	0.04	-0.06	34.00	31.00
	33.00	0.95	-1.31	0.05	-0.07	17.00	16.00

Table A - 5: Simulation results for a pole wheel with 40 poles

Ringmagnet 60 Poles Normal

R = 30 r = 20 h = 10

	Distance	E_max el.	E_min el.	E_max mech.	E_min mech.	B_max	B_min
	mm	°	°	°	°	mT	mT
Top Read	31.00	4.80	-5.72	0.16	-0.19	53.00	43.00
	31.50	3.66	-3.72	0.12	-0.12	31.00	27.00
	32.00	5.19	-6.19	0.17	-0.21	22.00	18.00
Two Probe	31.50	1.76	-2.69	0.06	-0.09	31.00	27.00

Table A - 6: Simulation results for a pole wheel with 60 poles

Appendix B – MATLAB Scripts

init.m

```
1 close all
2 clear all
3 clc
4
5 engine_speed = 15000; % rpm
6 temp = 25; % temp in °C
7 PREDICT_BYP = 1;
8 bfield = 23.9;
9 top_read = 1;
10
11 [angle, Bx_coarse, By_coarse, Bx_fine, By_fine, Bx_fine2, By_fine2]
= importLUT('./LUTs/polewheels38_40v2.txt');
12
13 Vdd = 2.5;
14
15 % Sensor 1 Parameters
16 Amp_x1 = 24e-3; % V/1VDD
17 Amp_y1 = 16e-3; % V/1VDD
18 TC_Amp_x1 = -0.35; % %/K
19 TC_Amp_y1 = -0.33; % %/K
20 FC_Amp_x1 = -0.05; % %/(kA/m)
21 FC_Amp_y1 = -0.05; % %/(kA/m)
22
23 Offset_x1 = 3e-3; % V/1VDD
24 Offset_y1 = -3e-3; % V/1VDD
25 TC_Offset_x1 = -2e-6; % V/1VDD/K
26 TC_Offset_y1 = 2e-6; % V/1VDD/K
27 FC_Offset_x1 = -0.3e-6; % V/1VDD/(kA/m)
28 FC_Offset_y1 = -0.3e-6; % V/1VDD/(kA/m)
29
30 Ortho1 = 5.00; % °
31 TC_Ortho1 = 0.0005; % °/K
32 FC_Ortho1 = -0.004; % °/(kA/m)
33
34
35 % Sensor 2 Parameters
```

```
36 Amp_x2 = 18e-3; % V/1VDD
37 Amp_y2 = 20e-3; % V/1VDD
38 TC_Amp_x2 = -0.34; % %/K
39 TC_Amp_y2 = -0.35; % %/K
40 FC_Amp_x2 = -0.05; % %/(kA/m)
41 FC_Amp_y2 = -0.05; % %/(kA/m)
42
43 Offset_x2 = -2e-3; % V/1VDD
44 Offset_y2 = 3e-3; % V/1VDD
45 TC_Offset_x2 = -2e-6; % V/1VDD/K
46 TC_Offset_y2 = 2e-6; % V/1VDD/K
47 FC_Offset_x2 = -0.3e-6; % V/1VDD/(kA/m)
48 FC_Offset_y2 = -0.3e-6; % V/1VDD/(kA/m)
49
50 Ortho2 = 2.00; % °
51 TC_Ortho2 = 0.0005; % °/K
52 FC_Ortho2 = -0.004; % °/(kA/m)
53
54
55 % Sensor 3 Parameters
56 Amp_x3 = 20e-3; % V/1VDD
57 Amp_y3 = 22e-3; % V/1VDD
58 TC_Amp_x3 = -0.34; % %/K
59 TC_Amp_y3 = -0.33; % %/K
60 FC_Amp_x3 = -0.05; % %/(kA/m)
61 FC_Amp_y3 = -0.05; % %/(kA/m)
62
63 Offset_x3 = 3e-3; % V/1VDD
64 Offset_y3 = -2e-3; % V/1VDD
65 TC_Offset_x3 = 2e-6; % V/1VDD/K
66 TC_Offset_y3 = -1e-6; % V/1VDD/K
67 FC_Offset_x3 = -0.3e-6; % V/1VDD/(kA/m)
68 FC_Offset_y3 = -0.3e-6; % V/1VDD/(kA/m)
69
70 Ortho3 = 7.00; % °
71 TC_Ortho3 = 0.0005; % °/K
72 FC_Ortho3 = -0.004; % °/(kA/m)
73
74 % Sigma Delta ADC and Cascaded Integrator Comb filter parameters
75
76 Vref = 0.120; % +Vref of 1 Bit-DAC. input Amplitude is 50mV at
bridge supply Vdd
```

```
= 2.5V
77 fs = 125e6; % sampling frequency in Hz
78 Ts = 1/fs; % sample time in s
79 R = 128; % rate change factor
80
81 FIR_BYP = 0; % 0 = filter active, 1 = inactive
82
83 if FIR_BYP == 1
84 fir_dec_factor = 1;
85 else
86 fir_dec_factor = 4;
87 end
88
89 if top_read
90 By_coarse = -1 * By_coarse;
91 By_fine = -1 * By_fine;
92 By_fine2 = -1 * By_fine2;
93 end
94
95 deltaT = temp - 25;
96 deltaB = bfield - 23.9;
97
98 save('fuses.mat', 'Vdd', 'deltaT', 'deltaB', 'Amp_x1', 'Amp_y1',
...
99 'TC_Amp_x1', 'TC_Amp_y1', 'FC_Amp_x1', 'FC_Amp_y1', 'Offset_x1',
...
100 'Offset_y1', 'TC_Offset_x1', 'TC_Offset_y1', 'FC_Offset_x1', ...
101 'FC_Offset_y1', 'Ortho1', 'TC_Ortho1', 'FC_Ortho1','Amp_x2', ...
102 'Amp_y2', 'TC_Amp_x2', 'TC_Amp_y2', 'FC_Amp_x2', 'FC_Amp_y2', ...
103 'Offset_x2', 'Offset_y2', 'TC_Offset_x2', 'TC_Offset_y2', ...
104 'FC_Offset_x2', 'FC_Offset_y2', 'Ortho2', 'TC_Ortho2', ...
105 'FC_Ortho2', 'Amp_x3', 'Amp_y3', 'TC_Amp_x3', 'TC_Amp_y3', ...
106 'FC_Amp_x3', 'FC_Amp_y3', 'Offset_x3', 'Offset_y3',
'TC_Offset_x3', ...
107 'TC_Offset_y3', 'FC_Offset_x3', 'FC_Offset_y3', 'Ortho3', ...
108 'TC_Ortho3', 'FC_Ortho3' );
```

calcVernierError.m

```
% This script calculates the maximum Vernier error from the raw B-Field
% components. Thus influences of electronics are neglected. The resulting
% error is used as threshold for the error peak compensation
% in the "angle calculation" block of the simulink model

close all
%clear all
clc

[angle, Bx_coarse, By_coarse, Bx_fine, By_fine, Bx_fine2, By_fine2] = importLUT('./LUTs/polewheels38_40v2.txt');

top_read = 1;
if top_read
By_coarse = -1 * By_coarse;
By_fine = -1 * By_fine;
By_fine2 = -1 * By_fine2;
end

two_probe = 1;

pole_pairs = 20;


angle_coarse = mod(180/pi * atan2(By_coarse, Bx_coarse),360);


if ~two_probe
angle_fine = mod(180/pi * atan2(By_fine, Bx_fine),360);
else
angle_fine = mod(180/pi * atan2(By_fine, Bx_fine),360);
angle_fine2 = mod(180/pi * atan2(By_fine2, Bx_fine2),360);


```

```
38 for i = 1:length(angle_fine)
39 if (angle_fine(i) - angle_fine2(i))>140
40 angle_combined(i,1) = (angle_fine(i) + angle_fine2(i)) / 2 - 180;
41 elseif (angle_fine(i) - angle_fine2(i))<-140
42 angle_combined(i,1) = (angle_fine(i) + angle_fine2(i)) / 2 + 180;
43 else
44 angle_combined(i,1) = (angle_fine(i) + angle_fine2(i)) / 2;
45 end
46 end
47
48 angle_fine = angle_combined;
49 end
50
51
52
53
54
55
56 % Vernier angle
57 diff_angle = mod(angle_fine-angle_coarse,360);
58
59 % calculate angles
60 angle_thresh = 360 / pole_pairs;
61
62 angle_fine_new = zeros(size(diff_angle));
63 for i = 1 : length(diff_angle)
64
65 angle_fine_new(i) = (360 * floor(diff_angle(i) / angle_thresh) +
angle_fine
(i)) / pole_pairs;
66
67 end
68
69
70
71 % OPTIONAL -> REDUZIERT DIE SPRÜNGE IM AUSGANGSWINKEL
72 Vernier_error = diff_angle - angle;
73
74
75 Vernier_error(Vernier_error > 180) = Vernier_error(Vernier_error >
180) - 360;
```

```
76 Vernier_error(Vernier_error < -180) = Vernier_error(Vernier_error <
-180) + 360;
77 plot(angle, Vernier_error)
78
79 delta = max(abs(Vernier_error));
80 disp(['Maximum Vernier error is ' num2str(delta) '°'])
81
82
83 for i = 1 : length(angle_fine_new)
84 err = angle_fine_new(i) - diff_angle(i);
85 if err > delta
86 angle_fine_new(i) = angle_fine_new(i) - angle_thresh;
87 end
88 if err < -delta
89 angle_fine_new(i) = angle_fine_new(i) + angle_thresh;
90 end
91 end
92
93
94
95
96 error = angle_fine_new - angle;
97 error(error > 180) = error(error > 180) - 360;
98 error(error < -180) = error(error < -180) + 360;
99
100 % offset = ( max(error) + min(error) ) / 2
101 % angle_fine_new = angle_fine_new - offset;
102 % error = error - offset;
103
104 figure
105 subplot(2,1,1)
106 plot(angle, angle_fine,'g')
107 hold on
108 plot(angle, angle_coarse,'b')
109 plot(angle, diff_angle, 'k')
110 plot(angle, angle_fine_new,'r')
111 legend('40 poles', '38 poles', 'Vernier angle', 'output angle' )
112 xlabel('reference angle °')
113 ylabel('measured angle °')
114 grid on
115
116 subplot(2,1,2)
```

```
117 plot(angle, error, 'r')
118 hold on
119 %plot(angle, Vernier_error, 'k')
120 xlabel('reference angle °')
121 ylabel('angle error °')
122 %legend('angle error', 'Vernier error')
123 legend('angle error')
124 grid on
125
126 disp(['Min Angle Error is ' num2str(min(error)) '°'])
127 disp(['Max Angle Error is ' num2str(max(error)) '°'])
```

angleCalculationAlgo.m

```
1 function measured_angle = angleCalculationAlgo(Vx_coarse, Vy_coarse,
Vx_fine, Vy_fine, Vx_fine2, Vy_fine2)
2
3 ADC_Gain = (2^15)/0.120;
4 Target_Gain = 2^14;
5 load fuses.mat
6
7
8 % Correct signals of sensor 1
9 TCO_X_S1 = deltaT * TC_Offset_x1 * Vdd * ADC_Gain;
10 OFFSET_X_S1 = Offset_x1 * Vdd * ADC_Gain; % without ACAL
11 OFFSET_X_T_S1 = OFFSET_X_S1 + TCO_X_S1;
12 X1_S1 = Vx_coarse - OFFSET_X_T_S1;
13
14 TCO_Y_S1 = deltaT * TC_Offset_y1 * Vdd * ADC_Gain;
15 OFFSET_Y_S1 = Offset_y1 * Vdd * ADC_Gain; % without ACAL
16 OFFSET_Y_T_S1 = OFFSET_Y_S1 + TCO_Y_S1;
17 Y1_S1 = Vy_coarse - OFFSET_Y_T_S1;
18
19 GAINQ_X_S1 = (ADC_Gain * Vdd * Amp_x1) / Target_Gain; % without AC-
AL;
20 GAINQ_X_T_S1 = GAINQ_X_S1 * (1 + TC_Amp_x1 * deltaT/100);
21 X2_S1 = X1_S1/GAINQ_X_T_S1;
22 X3_S1 = X2_S1;
23
24 GAINQ_Y_S1 = (ADC_Gain * Vdd * Amp_y1) / Target_Gain; % without AC-
AL;
25 GAINQ_Y_T_S1 = GAINQ_Y_S1 * (1 + TC_Amp_y1 * deltaT/100);
26 Y2_S1 = Y1_S1/GAINQ_Y_T_S1;
27
28 Ortho_S1 = Ortho1 + deltaT * TC_Ortho1;
29 Y3_S1 = (Y2_S1 - X2_S1 * sin(Ortho_S1 * pi/180) ) / cos(Ortho_S1 *
pi/180);
30
31
32 % Correct signals of sensor 2
33 TCO_X_S2 = deltaT * TC_Offset_x2 * Vdd * ADC_Gain;
34 OFFSET_X_S2 = Offset_x2 * Vdd * ADC_Gain; % without ACAL
35 OFFSET_X_T_S2 = OFFSET_X_S2 + TCO_X_S2;
36 X1_S2 = Vx_fine - OFFSET_X_T_S2;
```

```
37
38 TCO_Y_S2 = deltaT * TC_Offset_y2 * Vdd * ADC_Gain;
39 OFFSET_Y_S2 = Offset_y2 * Vdd * ADC_Gain; % without ACAL
40 OFFSET_Y_T_S2 = OFFSET_Y_S2 + TCO_Y_S2;
41 Y1_S2 = Vy_fine - OFFSET_Y_T_S2;
42
43 GAINQ_X_S2 = (ADC_Gain * Vdd * Amp_x2) / Target_Gain; % without AC-
AL;
44 GAINQ_X_T_S2 = GAINQ_X_S2 * (1 + TC_Amp_x2 * deltaT/100);
45 X2_S2 = X1_S2/GAINQ_X_T_S2;
46 X3_S2 = X2_S2;
47
48 GAINQ_Y_S2 = (ADC_Gain * Vdd * Amp_y2) / Target_Gain; % without AC-
AL;
49 GAINQ_Y_T_S2 = GAINQ_Y_S2 * (1 + TC_Amp_y2 * deltaT/100);
50 Y2_S2 = Y1_S2/GAINQ_Y_T_S2;
51
52 Ortho_S2 = Ortho2 + deltaT * TC_Ortho2;
53 Y3_S2 = (Y2_S2 - X2_S2 * sin(Ortho_S2 * pi/180) ) / cos(Ortho_S2 *
pi/180);
54
55
56 % Correct signals of sensor 3
57 TCO_X_S3 = deltaT * TC_Offset_x3 * Vdd * ADC_Gain;
58 OFFSET_X_S3 = Offset_x3 * Vdd * ADC_Gain; % without ACAL
59 OFFSET_X_T_S3 = OFFSET_X_S3 + TCO_X_S3;
60 X1_S3 = Vx_fine2 - OFFSET_X_T_S3;
61
62 TCO_Y_S3 = deltaT * TC_Offset_y3 * Vdd * ADC_Gain;
63 OFFSET_Y_S3 = Offset_y3 * Vdd * ADC_Gain; % without ACAL
64 OFFSET_Y_T_S3 = OFFSET_Y_S3 + TCO_Y_S3;
65 Y1_S3 = Vy_fine2 - OFFSET_Y_T_S3;
66
67 GAINQ_X_S3 = (ADC_Gain * Vdd * Amp_x3) / Target_Gain; % without AC-
AL;
68 GAINQ_X_T_S3 = GAINQ_X_S3 * (1 + TC_Amp_x3 * deltaT/100);
69 X2_S3 = X1_S3/GAINQ_X_T_S3;
70 X3_S3 = X2_S3;
71
72 GAINQ_Y_S3 = (ADC_Gain * Vdd * Amp_y3) / Target_Gain; % without AC-
AL;
73 GAINQ_Y_T_S3 = GAINQ_Y_S3 * (1 + TC_Amp_y3 * deltaT/100);
```

```
74 Y2_S3 = Y1_S3/GAINQ_Y_T_S3;
75
76 Ortho_S3 = Ortho3 + deltaT * TC_Ortho3;
77 Y3_S3 = (Y2_S3 - X2_S3 * sin(Ortho_S3 * pi/180) ) / cos(Ortho_S3 *
pi/180);
78
79
80 Vx_coarse = X3_S1;
81 Vy_coarse = Y3_S1;
82 Vx_fine = X3_S2;
83 Vy_fine = Y3_S2;
84 Vx_fine2 = X3_S3;
85 Vy_fine2 = Y3_S3;
86
87
88 two_probe = 1;
89 pole_pairs = 20;
90
91 angle_coarse = mod(180/pi * atan2(Vy_coarse, Vx_coarse),360);
92
93 if ~two_probe
94 angle_fine = mod(180/pi * atan2(Vy_fine, Vx_fine),360);
95 else
96 angle_fine = mod(180/pi * atan2(Vy_fine, Vx_fine),360);
97 angle_fine2 = mod(180/pi * atan2(Vy_fine2, Vx_fine2),360);
98 if ( angle_fine - angle_fine2 ) > 140
99 angle_fine = ( angle_fine + angle_fine2 ) / 2 - 180;
100 elseif ( angle_fine - angle_fine2 )<-140
101 angle_fine = ( angle_fine + angle_fine2 ) / 2 + 180;
102 else
103 angle_fine = ( angle_fine + angle_fine2 ) / 2;
104 end
105 end
106
107 % Vernier angle
108 diff_angle = mod(angle_fine-angle_coarse,360);
109
110
111 angle_thresh = 360 / pole_pairs;
112
113
```

```
114 angle_fine_new = (360 * floor(diff_angle / angle_thresh) + an-
gle_fine) /
pole_pairs;
115
116
117 error = angle_fine_new - diff_angle;
118 if error > 4.55%5.9766; % max(abs(Vernier_error));
119 angle_fine_new = angle_fine_new - angle_thresh;
120 end
121 if error < -4.55%-5.9766;
122 angle_fine_new = angle_fine_new + angle_thresh;
123 end
124
125
126 measured_angle = angle_fine_new;
```

calcErrors.m

```
% This script calculates the angle error of the overall system, including
% errors introduced by the ADC, sensor mismatch and the compensation
% algorithm

calcVernierError;
yi = interp1(((0:360)./360).*4e-3,angle_fine_new, angle_out.time);
ref_angle = (angle_out.time/4e-3)* 360;

error_ref = yi(5:end-5) - ref_angle(5:end-5);


figure
plot(angle_out.time(5:end-5), error_ref)
hold on


% deviation from mechanical reference angle with delay time
error_adc = angle_out.signals(1).values(5:end-5) - angle_out.signals(2).values(5:end-5);
disp(['Maximum angle error including signal processing path and angle delay time is ', num2str(max(error_adc)) ])
disp(['Minimum angle error including signal processing path and angle delay time is ', num2str(min(error_adc)) ])

% deviation from mechanical reference angle without delay time
offset_delay = ((max(error_adc) + min(error_adc))/2) - ((max(error_ref) + min
(error_ref))/2)
error_adc = error_adc - offset_delay;
delay_time = offset_delay / (engine_speed/60 * 360)
plot(angle_out.time(5:end-5), error_adc,'r')
legend('Raw B-field components', 'Simulink model')
ylabel('Error in °')
title('deviation from reference angle')
grid on

disp(['Maximum angle error including signal processing path, but excluding delay is ', num2str(max(error_adc)) ])
```

```
33 disp(['Minimum angle error including signal processing path, but
excluding delay is ', num2str(min(error_adc)) ])
34
35
36 % Quantization error including errors of compensation algorithm
37
38 quantization_error = error_adc - error_ref;
39 quantization_error = quantization_error - ((max(quantization_error)
+ min(quantization_error))/2);
40
41 figure
42 plot(angle_out.time(5:end-5), quantization_error)
43 grid on
44 title('Error introduced by quantization and sensor mismatch compen-
sation')
45 ylabel('Error in °')
46 xlabel('time in s')
47
48 disp(['Maximum angle noise is ', num2str(max(quantization_error))
])
49 disp(['Minimum angle noise is ', num2str(min(quantization_error))
])
50
51
52 % discard three sigma outliers
53 num = floor(length(quantization_error) * 0.997);
54 values = sort(abs(quantization_error));
55 values = values(1:num);
56
57 disp(['Maximum 3-sigma angle noise is ', num2str(max(values)) ])
58
```

References

[1] **Meyer, G und Valldorf, J.** *Advanced Microsystems for Automotive Applications 2011.* Springer, 2011.

[2] **Binder, G.** *Konzeptuntersuchung Modellierung eines Permanentmagneten in MATLAB.* TU Graz, Institut für Elektronik, 2011.

[3] **Infineon Technologies AG.** *Position Feedback for Motor Control Using Magnetic Sensors.* Infineon Technologies AG, 2010.

[4] **Kadar, Z.** *Integrated Resonant Magnetic Field Sensor.* 1997. ISBN: 90-407-1411-8.

[5] **Marti, O und Plettl, A.** *Vorlesungsskript Physikalische Elektronik und Messtechnik.* Universität Ulm, 2007.

[6] **Sensitec GmbH.** *Application Note: AMR Free Pitch Sensoren für Winkel und Längenmessung. AA700 Familie.* 2009.

[7] **Granig, W, et al.** *Performance and Technology Comparison of GMR versus commonly used Angle Sensor Principles for Automotive Applications.* SAE Paper Nr. 2007-01-0397, 2007.

[8] **Granig, W, et al.** *Integrated Gigant Magnetic Resistance based Angle Sensor.* 5th IEEE confernce on sensors, 2006.

[9] **Hammerschmidt, D, et al.** *Giant magneto resistors – sensor technology & automotive applications.* SAE Paper Nr. 2005-01-0462, 2005.

[10] **Infineon Technologies AG.** *TLE5012B GMR-Based Angular Sensor - Datasheet.* Infineon Technologies AG, 2010.

[11] **Frachon, D, et al.** *Absolute magnetic sensors for large diameter through-shaft applications.* Moving Magnet Technologies SA, 2010.

[12] **Granig, W, Hammerschmidt, D und Leteinturier, P.** *Offenlefungsschrift.* Deutsches Patent- und Markenamt, 2009. Patent Nr.: DE102009038256A1.

[13] **Infineon Technologies AG.** *TLE5009 GMR-Based Angular Sensor - Application Note TLE5009 Calibration.* Infineon Technologies AG, 2010.

[14] **Infineon Technologies AG.** *TLE5009 GMR-Based Angular Sensor - Datasheet.* Infineon Technologies AG, 2011.

[15] **Yao, L, Steyaert, M und Sansen, W.** *Low-Power Low-Voltage Sigma-Delta Modulators in Nanometer CMOS.* Springer, 2006. ISBN: 1-4020-4139-X.

[16] **Kester, W.** *ADC Architectures III: Sigma-Delta ADC Basics.* Analog Devices, Inc, 2009.

[17] **Maxim Integrated Products.** *APPLICATION NOTE 1870: Demystifying Delta-Sigma ADCs.* 2003.

[18] **Maxim Integrated Products.** *APPLICATION NOTE 1080: Understanding SAR ADCs: Their Architecture and Comparison with Other ADCs.* 2001.

[19] **Hogenauer, E.** *An Economical Class of Digital Filters for Decimation and Interpolation.* IEEE, 1981.

[20] **Donadio, M.** *CIC Filter Introduction.* http://www.amrad.org/projects/dsp/cic1.pdf [last known version: 02.02.2012], 2000.

[21] **Lyons, R.** *Understanding cascaded integrator-comb filters.* http://eetimes.com/design/embedded/4006446/Understanding-cascaded-integrator-comb-filters [last known version: 02.02.2012], 2005.

[22] **Kester, W.** *Understand SINAD, ENOB, SNR, THD, THD + N, and SFDR so You Don't Get Lost in the Noise Floor.* Analog Devices, Inc, 2009.

[23] **Maxim Integrated Products.** *APPLICATION NOTE 641: ADC and DAC Glossary.* 2000.

[24] **Maxim Integrated Products.** *Application Note 729: Dynamic Testing of High-Speed ADCs.* http://pdfserv.maxim-ic.com/en/an/AN729.pdf [last known version: 13.02.2012], 2002.

[25] **Kester, W.** *Taking the Mystery out of the Infamous Formula, "SNR = 6.02N + 1.76dB," and Why You Should Care.* Analog Devices, Inc, 2009.

[26] **www.mikrocontroller.net.** *AVR-Tutorial.* http://www.mikrocontroller.net/articles/AVR-Tutorial:_Arithmetik8 [last known version: 19.03.2012].

[27] **Parhami, B.** *Computer Arithmetic: Algorithms and Hardware Designs.* Oxford University Press, 2010. ISBN: 978-0-19-532848-6.

[28] **Kester, W.** *ANALOG-DIGITAL CONVERSION.* Analog Devices, Inc, 2004. ISBN: 0-916550-27-3.